Winter 2022

Implementing a reference backscatter calibration technique on a multi-sector multibeam echosounder

Rui Miguel Aleixo Miguel Cândido
University of New Hampshire, Durham

IMPLEMENTING A REFERENCE BACKSCATTER CALIBRATION TECHNIQUE ON A MULTI-SECTOR MULTIBEAM ECHOSOUNDER

By

Rui Miguel Aleixo Miguel Cândido

M.S. in Naval Military Sciences, Escola Naval, Portugal, 2011

THESIS

Submitted to the University of New Hampshire

in Partial Fulfillment

of the Requirements for the Degree of

Master of Science

In

Earth Sciences: Ocean Mapping

December 2022

This thesis was examined and approved in partial fulfillment of the requirements for the degree of Master of Science in Earth Sciences: Ocean Mapping by:

Thesis Director, John Hughes Clarke, Professor, Earth Sciences and Ocean Engineering, Center for Ocean Coastal Mapping, University of New Hampshire

Brian Calder, Research Professor, Earth Sciences and Ocean Engineering, Center for Ocean Coastal Mapping, University of New Hampshire

Thomas Weber, Affiliate Research Professor, Center for Ocean Coastal Mapping, University of New Hampshire

On September 16th, 2022

Approval signatures are on file with the University of New Hampshire Graduate School.

ACKNOWLEDGEMENTS

My incredible two-year experience at the University of New Hampshire would not have been possible without the contribution of several remarkable personalities and organizations.

I would like to express my deepest appreciation to my thesis committee, Professors John Hughes Clarke, Brian Calder and Tom Weber, who had such an inspirational role throughout my learning journey, as their joy and dedication in teaching is truly fascinating, especially considering the struggles and challenges the pandemic brought upon us all. I would like to sincerely thank Professor Larry Mayer that, despite not officially integrating the committee, provided meaningful insight and contributed to a better dissertation.

My success would not have been possible without the invaluable insight and relentless support of Professor John Hughes Clarke, my advisor. The innumerous learning opportunities he promoted, his contagious enthusiasm about Ocean Mapping and welcoming personality, continuously encouraged me to improve and deepen my knowledge. Having worked with him daily for the past two years is one of the defining milestones of my hydrographic career.

I am deeply indebted to the Portuguese Navy for providing and fully funding this invaluable learning opportunity, which I am sure it will be put to good use in future deployments.

Special thanks to Kjell Nilsen, who provided valuable advice on how to interpret and process .KMALL datagrams.

I am grateful for the support and friendship of my fellow students, especially Brandon Maingot, Daniel Leite and Juliane Affonso. Your camaraderie brought joy to my student life and the academic discussions we had helped me become a better ocean mapper.

I would like to acknowledge the faculty and staff of the Center for Coastal and Ocean Mapping, to whom I had great pleasure of working with.

Finally, I would like to express my deepest gratitude and love to my family. My loving wife, Diana, was able to move abroad, pursue her PhD remotely and build a home from scratch, all while supporting my academic efforts, being an excellent Mother and taking care of our cat, Banzé. My daughter Lara, who constantly provided me with playful and relaxing moments, helped me release the stress associated to exams and deadlines. It was wonderful watching her grow. To my Parents, my Parents-in-law, and my Sister, thank you for enduring this separation and maintaining the foundations of our Family in Portugal, for supporting me whenever I needed your assistance and for encouraging me to follow my dreams.

TABLE OF CONTENTS

ABSTRACT

Increasingly, national hydrographic agencies are committing to routine acquisition of seabed backscatter strength estimates from multibeam echosounders (MBES) as part of national programs for seabed characterization. As part of their bathymetric survey mandate, these agencies have a long history of sounding quality control utilizing absolute and relative calibration (reference surfaces and crossover comparisons). Equivalent quality control is, however, not yet in place for managing seabed backscatter strength measurements, as the majority of the collected data is not absolutely referenced.

Herein, a new technique for cross-calibrating a MBES with a reference calibrated split-beam echosounder (SBES) was implemented. Broadband reference bottom backscatter strength (45-450 kHz) from areas with different seafloor types, derived from data obtained with Simrad EK80 SBES, is used to adjust the received acoustic intensities acquired from the same areas with several multi-sector MBES (Kongsberg Maritime EM2040P, EM710 and EM712), thereby enabling the routine collection of absolutely referenced bottom backscatter strength measurements. Previous efforts to implement a similar cross-calibration only considered a simplified vertically referenced ensonification geometry, ignoring the dynamic variations due to vessel rotations and active stabilization. As a result, neither the rotation of the beam pattern with respect to the vertical reference nor the compensation due to active beam stabilization were accounted for. Furthermore, this method properly accounts for modern MBES which have multiple transmit sectors over multiple swaths with the associated changes in frequency and signal modulation.

The main output of this research is a set of two-dimensional arrays of correctors, derived for each transmit sector - the correction heatmap - providing estimates of the necessary calibration, as a function of across- and along-track sonar referenced angles. To test the repeatability of the proposed technique, correction heatmaps derived for the same system (using the same settings), but with data from different reference areas, were compared, resulting in differences generally within ± ~2 dB.

Finally, a pre-calibrated MBES was used to survey a different location and establish a reference area, enabling the subsequent calibration of sonars that use the same frequencies.

1. INTRODUCTION

1.1. The need for seafloor characterization

Characterizing the physical properties of the seabed has long been recognized as a fundamental pre-requisite for a wide range of marine science and engineering applications. Most recently, that need has been explicitly embedded into both international and national initiatives. For example, the United Nations Decade of Ocean Science for Sustainable Development 2021-2030 initiative objectively sets the goal of creating a digital representation of the Ocean (UNESCO/IOC, n.d.), for which seafloor mapping and characterization are required. An example at a national scale is the Presidential Memorandum of November 19, 2019, regarding the *Ocean Mapping of the United States Exclusive Economical Zone* (EEZ) *and Shoreline and Nearshore of Alaska*, which acknowledged that only ~40% of the United States EEZ had been mapped and considerably less had its resources and ocean systems characterized. Subsequently, it was deemed necessary to implement a strategy for mapping, exploring and (most relevantly for this thesis) characterizing the seafloor.

What exactly, however, constitutes characterization of a seafloor depends on the user group. Traditionally, physical descriptions such as mud, sand or gravel have sufficed (Wentworth, 1922). For the offshore geotechnical engineering community, shear strength and bulk modulus are desired (Thompson & Beasley, 2012). For the naval warfare community, acoustic parameters such as impedance, attenuation and roughness are of interest (Inman & Jenkins, 2002; Mulhearn, 2000; Wilkens & Richardson, 2007). For the benthic biological community, more nebulous parameters such as habitat suitability for specific species are desired (J. T. Anderson et al., 2008; T. J. Anderson et al., 2007; Brown et al., 2011; Foveau et al., 2017).

1.2. The approach: acoustic remote sensing

While unambiguous direct characterization has long been achieved at point locations using *in situ* physical sampling (e.g., grabs, cores, cone penetrometers), such an approach is impractical to deliver mapping at the scales now demanded. Thus, remote sensing techniques are desired and, given the widespread use of single beam, sidescan and multibeam sonars, acoustic-based characterization has been attempted (J. T. Anderson et al., 2008).

Many of the desired seafloor properties listed above cannot, however, be directly derived from acoustic remote sensing. As an alternate indirect approach, these can be estimated by feeding theoretical and empirical models (e.g., Jackson et al., 1986) that relate seafloor physical properties with measurements of seabed slope and acoustic bottom backscatter strength (S_b) (e.g., Angular Range Analysis from Fonseca & Mayer, 2007). To do so effectively, however, requires both the model being appropriate and the S_b measurements being bias free. This thesis focuses on the second issue, the fidelity of S_b measurements.

S_b is an inherent property of a given type of seabed, being only dependent of the grazing angle – the angle between the seafloor and the ensonification axis (Figure 1.1) – and the frequency of the acoustic signal (Urick, 1954) as illustrated in Figure 1.2 and Figure 1.3, potentially thereby making it a powerful seafloor classifier.

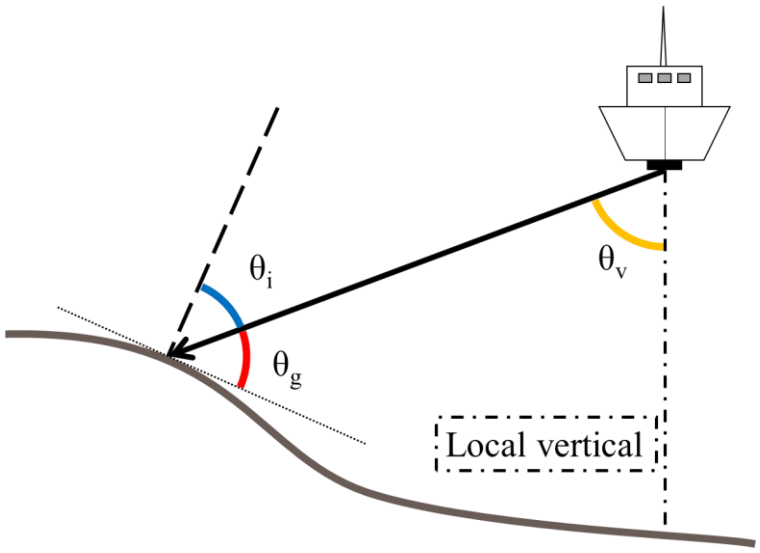

Figure 1.1: Representation of the grazing angle (θ_g), incidence angle (θ_i) and vertical referenced angle (θ_v). The dashed line represents a vector orthogonal to the seafloor, the dotted line represents a vector tangent to the seafloor, the dash-dotted line represents the local vertical direction and the arrow represents the ensonification axis.

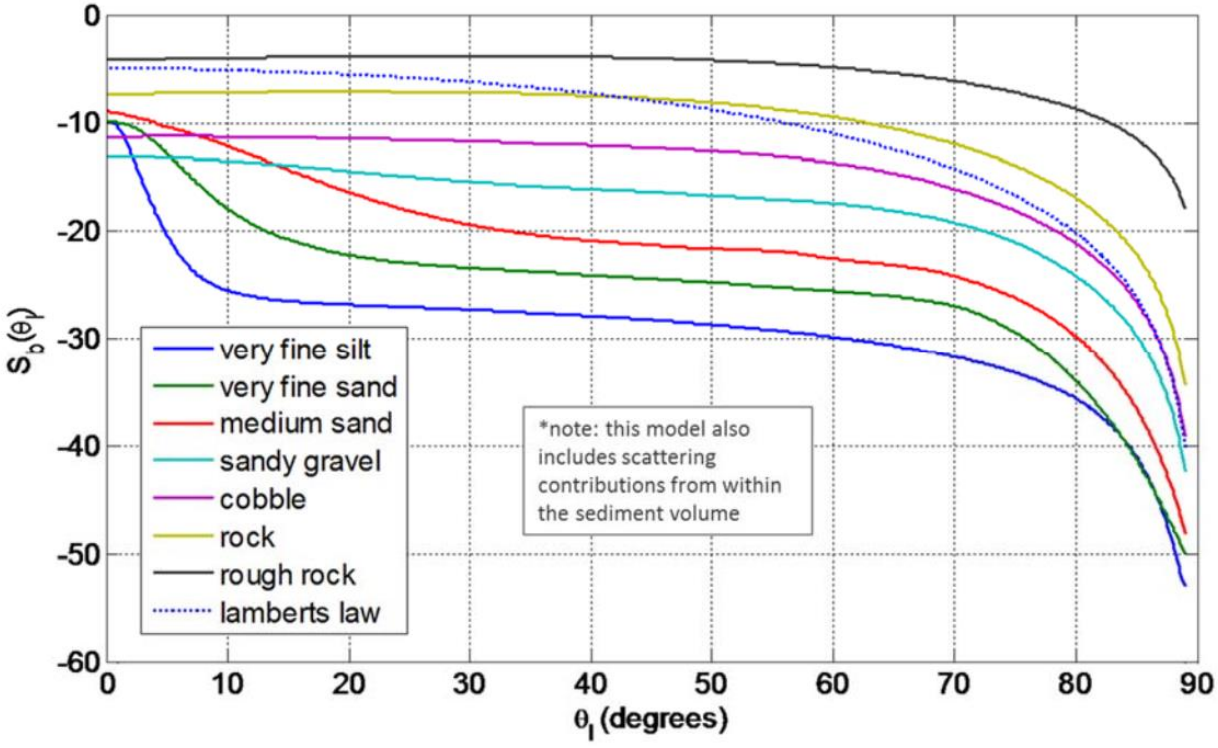

Figure 1.2: Example of incidence angle dependent S_b for different substrate types at 100 kHz, based on model results using the Applied Physics Laboratory – University of Washington (APL-UW) model (APL-UW, 2014). From Weber & Lurton (2015).

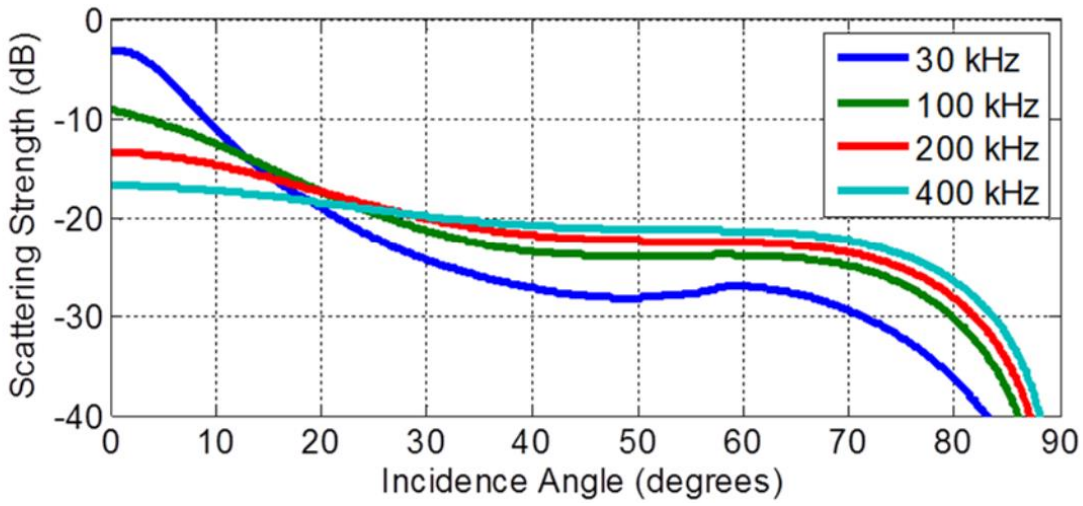

Figure 1.3: Example of incidence angle dependent S_b for medium sand at medium frequencies, based on model results using the APL-UW (2014) model. From Weber & Lurton (2015).

Given the advantage in propagation of acoustic methods over optical methods in water, acoustics are, arguably, the most valuable approach to remotely sense the ocean floor. Furthermore, increasingly, the most commonly used acoustic mapping technology is the multibeam echosounder system (MBES), which is the *de facto* modern hydrographic surveying tool. Although high resolution bathymetry maps are its most recognizable product, MBES additionally are capable of co-locating depth measurements and acoustic received intensities, from which the S_b can be estimated. For several decades now, MBES have been deemed capable of providing such a means of characterizing the nature of the seafloor (de Moustier, 1986). Ideally, if properly reduced, the S_b is independent of the characteristics of the sonar. That reduction, however, is fraught with complications (Hughes Clarke et al., 2008; Lamarche & Lurton, 2018; Malik et al., 2018; Schimel et al., 2018) and in practice most measurements are not bias-free. This thesis is an attempt toward improving that state of affairs.

1.3. The complication: imperfect measurements

With inadequate reduction, as depicted in Figure 1.4, different sonars will provide significantly different S_b estimates for the same area, making the comparison of S_b products acquired with distinct MBES a very difficult task (Hughes Clarke et al., 2008; Lamarche & Lurton, 2018).

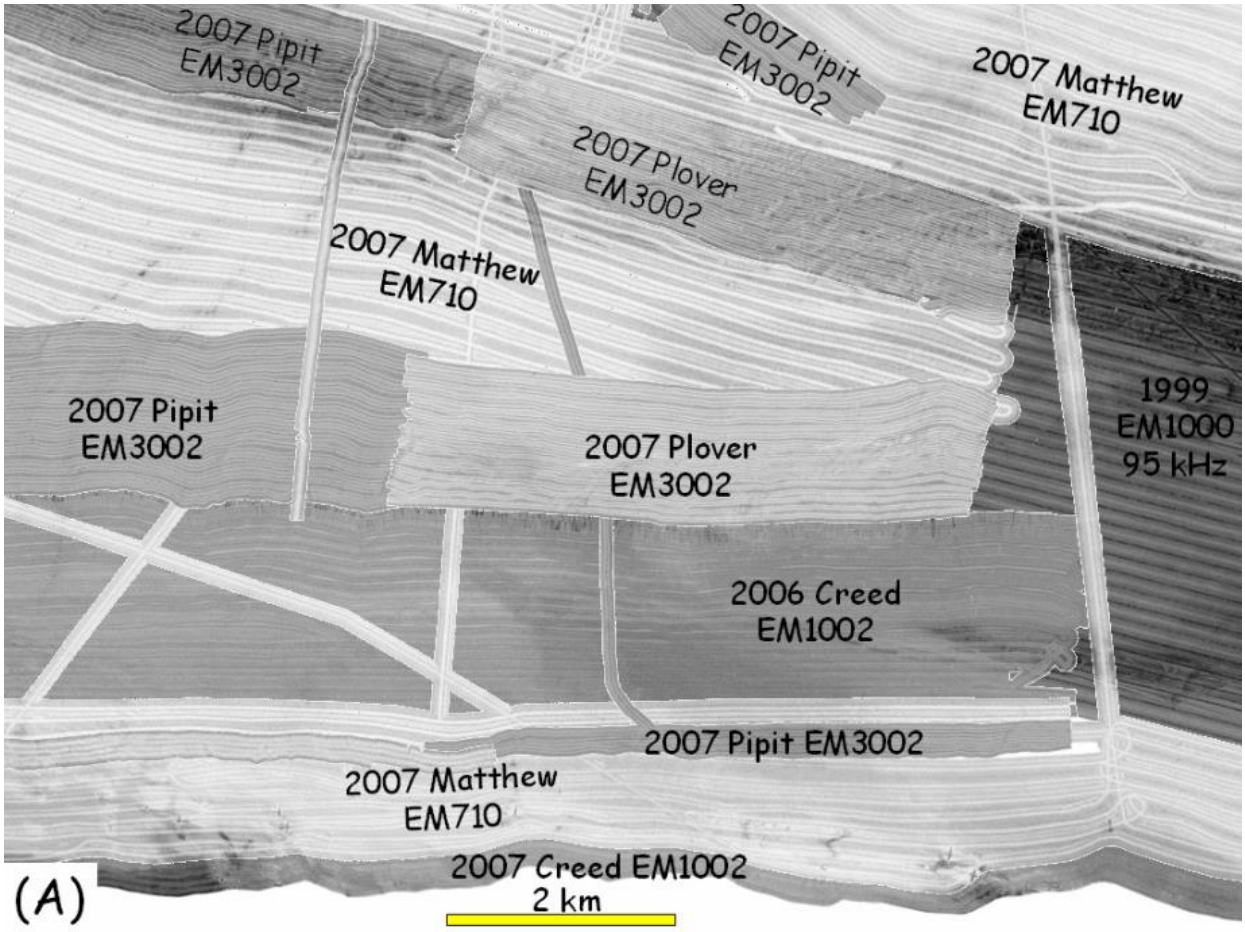

Figure 1.4: Mosaic of backscatter data from different MBES, as acquired. From Hughes Clarke et al. (2008).

While most published studies of acoustic seabed remote sensing have shown promise for the case of a single sonar deployment, the reality of most national mapping programs is that

regional scale mapping is conducted over multiple years with multiple systems. The net result is that at the present time, regrettably, if obtained with different MBES, S_b estimates for the same area will often not be repeatable.

While there are several components to proper data reduction (see Chapter 2), in many instances the problem resides primarily in the radiometric characteristics of the sonar – its acoustic source level (SL in dB re 1µPa at 1m) and receiver sensitivity (M in dB re 1V/1µPa) – being unknown, including its dependence on the array-relative ensonification direction – the beam pattern. While some sonar manufacturers provide estimates for SL and M, these are usually not accurate enough to derive identical S_b estimates from different systems. An example of manufacturer-provided SL and M angular dependence is illustrated in Figure 1.5.

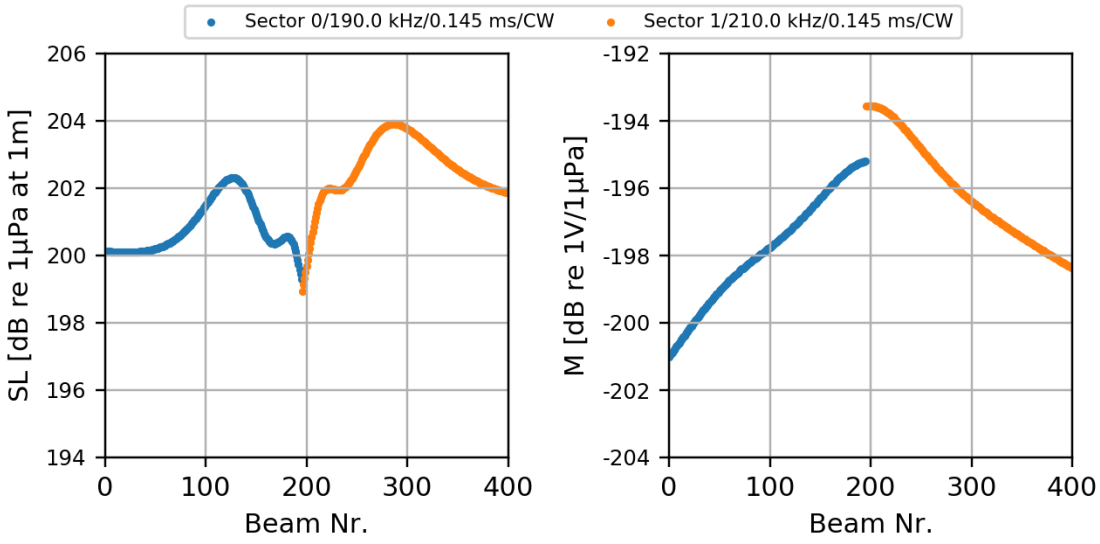

Figure 1.5: Manufacturer-provided SL and M estimates, sorted by beam number, for a particular swath of a Kongsberg Maritime EM2040P MBES, operating at 200 kHz in Shallow depth mode and dual swath (two transmit sectors per swath).

While both SL and M impact the measurement, ultimately it is their product that is embedded in the S_b measurements. Thus, for the purpose of S_b data reduction, if just their product is known, that can suffice.

1.4. Current solutions and the need for improvement

To derive S_b estimates independent of the used sonar, several techniques have been attempted. One of the most notable was proposed by Eleftherakis et al. (2018), in which S_b values from the same location are derived both with a calibrated sonar (i.e., a sonar outputting absolutely referenced S_b) and an uncalibrated MBES, each operating at similar frequencies (Figure 1.6). In principle, the difference between the two datasets should permit the establishment of the MBES response bias and to determine the necessary combined SL and M compensations to obtain absolutely referenced S_b estimates from it.

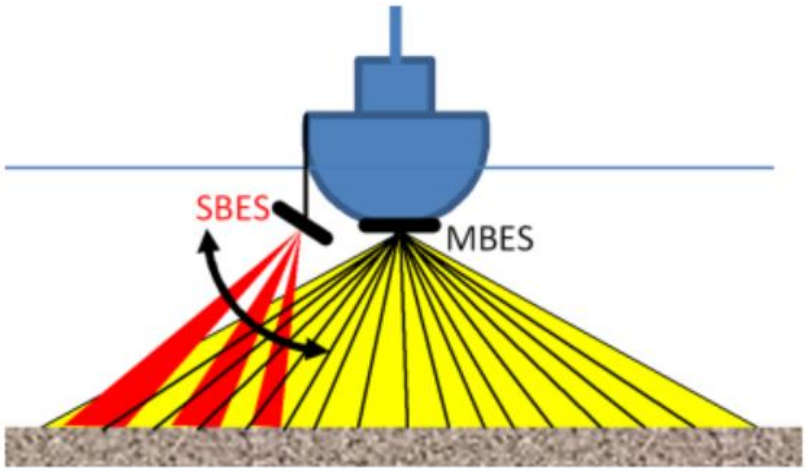

Figure 1.6: Cross calibration between a MBES and a calibrated split-beam echosounder (SBES). From Eleftherakis et al. (2018).

Estimating the combined SL and M angular dependence for a particular MBES (i.e., calibrating the sonar) is not a trivial task. The architecture of modern MBES encompasses the use of several transmit sectors, each with its individual steering, allowing it to compensate for the vessel's motion and to provide a uniform seafloor ensonification. Furthermore, multiple swaths can be used in a single transmission-reception cycle, increasing the along-track seafloor ensonification density. Subsequently, each transmit sector (of each swath) will have its own characteristic combined transmit/receive angular dependence and acoustic frequency, which must be considered in the calibration process. To date, this has not been adequately addressed by current methods.

1.5. Dealing with reference frames

The proper quantification of the SL and M angular dependence must be related to angles measured in a sonar referenced frame, whose relationship with a vertically referenced frame – where the z axis follows the gravity vector – depends on the vessel attitude and on the installation orientation of the sonar on the vessel. For this dissertation, several coordinate systems will be relevant. Firstly, a vertically referenced georeferenced coordinate system (GCS) must be defined, centered somewhere in the sea surface, with its x and y-axis pointing North and East respectively. With respect to it, a vessel coordinate system (VCS) can be established, with its origin being a reference point (RP) physically located on the platform, typically its metacenter or center of gravity. Its x and y-axis point in the forward and starboard directions respectively. The VCS is no longer a vertically referenced frame, since its orientation will depend on the attitude of the vessel (roll, pitch, heading), which will change between the time of transmission and reception. In addition to the GCS, it is also useful to establish a vertically referenced frame – denominated the

surface coordinate system (SCS) – centered on the vessel's RP and with its x-axis pointing along the horizontal projection of the VCS x-axis. Finally, array coordinate systems (ACS) centered on the receive and/or transmit transducers can be established. The orientation of the ACS with respect to the GCS will depend both on the vessel's attitude and on the array mounting angles, measured in the VCS. An example of the establishment of these coordinate systems is presented in Figure 1.7.

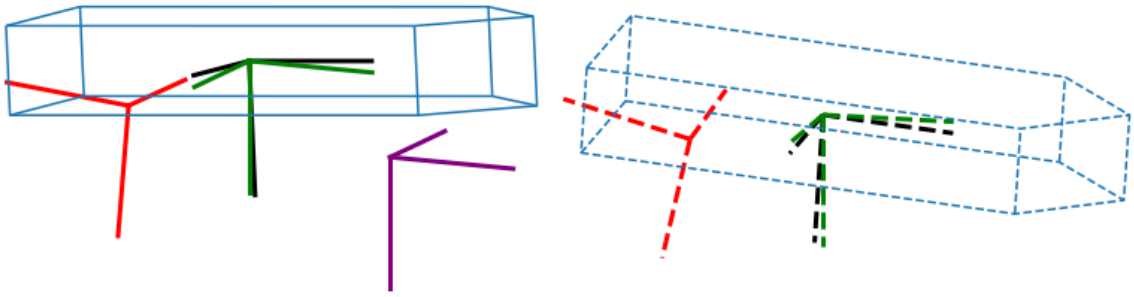

Figure 1.7: Relevant coordinate systems: GCS (purple), SCS (green), VCS (black), and ACS (red). The different line styles represent different time instants (transmission and reception).

1.6. What this thesis intends to address

The calibration approach described by Eleftherakis et al. (2018) was developed for a MBES with a single transmit sector and swath, and does not account for the beam pattern variations due to active steering, characterizing the MBES response bias only in a vertically referenced frame. Therefore, when applied to a sonar performing motion compensation, especially yaw stabilization, and/or using multiple swaths, it would contribute to less-than-optimal S_b estimates. Additionally, as multiple sectors are often separated in frequency, the calibrated sonar would have to provide multispectral reference S_b values to enable the comparison between the calibrated and uncalibrated datasets.

Considering the described framework, this research takes inspiration from Eleftherakis et al. (2018) contributions and aims to expand them by enabling their use in multisector MBES and accounting for all the vessel's rotations, active beam steering and usage of different frequencies. To describe how the transmit/receive beam pattern varies in the sonar reference frame, the geometry developed by Hiroji (2016) proved valuable and was incorporated into this study. Moreover, this research uses the results presented by Guimarães (2020), consisting of S_b absolutely referenced estimates from several sites, over a wide range of grazing angles, at frequencies commonly used by shelf-depth sonars (40-400 kHz). Conveniently, Guimarães (2020) also collected uncalibrated MBES data at the same locations, facilitating the development of the present study.

The main goal of this research is to develop a processing pipeline for the calibration of MBES S_b data by comparing it against reference datasets fully accounting for all the reference frame offsets, thereby allowing the determination of adequate correctors that properly consider the sonar's operational settings: frequency, steering, number of swaths and number of sectors. The subsequent usage of absolutely referenced S_b estimates will promote the compatibility of datasets obtained from different sonars, enabling the generation of comparable S_b based products and ultimately contribute to more accurate seafloor characterization processes.

The layout of this thesis is as follows:

- Chapter 2 depicts the theory behind reducing bottom backscatter strength estimates from received acoustic intensities, addressing the terms of the active sonar equation and describing the S_b physical controls.

- Chapter 3 addresses how beamforming and motion compensation processes influence the transmit and receive beam patterns, highlighting the particularities of single and multi-sector MBES.
- Chapter 4 provides an overview of existing methods used to obtain calibrated S_b estimates.
- Chapter 5 describes the technique developed under the scope of this thesis to obtain absolutely referenced Sb estimates from multi-sector, multi-swath MBES.
- Chapter 6 shows and discusses the results of applying the developed technique on specific datasets.
- Chapter 7 concludes this research.

2. FROM RECEIVED ACOUSTIC INTENSITIES TO S_b

Bathymetry is often known as the primary product of echosounders. The time elapsed between transmission and reception can be converted to depth if the sound speed throughout the water column and the initial direction of the acoustic ray can be estimated. However, the received echo also has the potential to provide further information about the bottom. Indeed, if the combined effects of the sonar architecture and the acoustic propagation throughout the water column are considered, it should be possible to characterize how the acoustic pulse interacts with the seafloor.

A simple way of describing the relationship between the received echo, the sonar architecture and the acoustic interaction with the medium – the water column – and the seafloor is through the active monostatic sonar equation, which can be presented as

$$S_b = EL_V - SL - M - A + 2TL \qquad 2.1$$

where all terms are in decibel units: the bottom backscatter strength (S_b in dB), the voltage associated to the received acoustic intensity (EL_V in dB re 1V), the sonar transmit source level (SL in dB re 1μPa at 1m) and receiver sensitivity (M in dB re 1V/1μPa), the ensonified area (A in dB re $1m^2$) and the two-way transmission loss (2TL in dB) (adapted from Augustin & Lurton, 2005). The following sections detail the mentioned terms.

2.1. Bottom Backscatter Strength

Urick (1954) was one of the earliest to identify that the backscattered (i.e., scattered towards the source) to incident acoustic intensity ratio, normalized for the ensonified area, could provide information about the roughness and composition of the seafloor. In principle, this ratio is

an inherent property of the seafloor and is addressed as the interface backscattering cross-section per unit area (σ), defined as

$$\sigma(\theta_i) = \frac{R^2 \ < I_s(R, \theta_i) >}{I_i(\theta_i)A} \qquad 2.2$$

where $< I_s (R, \theta_i) >$ is the idealized average over an infinite ensemble of scattered intensities I_s measured at the range R from the seafloor at an incidence angle θ_i, I_i is the incident intensity and A is the ensonified area (adapted from Jackson & Richardson, 2007). In its logarithmic form

$$S_b(\theta_i) = \ 10 \log_{10} \sigma(\theta_i) \qquad 2.3$$

it is usually referred to as bottom backscattering strength (S_b) (Jackson & Richardson, 2007; Lurton, 2002; Urick, 1954).

Although a single I_s might seem to imply a fixed returned EL_V, in reality, considering a specific patch of the seafloor, observed from the same direction with a particular sonar, randomly fluctuating EL_V values would be acquired. This stochastic nature results from the summation of the backscattered contributions from activated scatterers with statistically independent random phases (Stanic & Kennedy, 1992; Weber & Lurton, 2015), resulting in the backscattered amplitudes ($a_b = \sqrt{\frac{R^2 \ I_s(R,\theta_i)}{I_i(\theta_i)A}}$) following a Rayleigh like distribution, or more generally, a Weibull distribution (Fonseca et al., 2021). Therefore, rather than considering individual I_s values to characterize the bottom, an ensembled average must be considered to obtain meaningful S_b estimates.

2.2. Ensonified Area

Considering the classical Mill's cross array design, where the transmit and receive arrays are typically aligned with the alongship and athwartship directions respectively, the ensonified

area is bounded along-track by the transmit beamwidth and, across-track, either by the receive beamwidth (beamwidth limited or long-pulse regime) or by the projection of the transmit pulse on the seafloor (pulse length limited or short-pulse regime) (Hellequin et al., 2003; Lurton, 2002).

In the beamwidth limited / long-pulse regime, commonly observed at normal or near normal incidence, the beam footprint is completely ensonified by the pulse projection on the seafloor. However, in the pulse length limited / short-pulse regime, occurring mostly at oblique incidences, the ensonified area is a sector of an annulus, decreasing with the increasing incidence angle and proportional to range (Weber & Lurton, 2015). The ensonified area in the beamwidth limited and pulse length limited regimes can be approximated by equations 2.4 and 2.5 respectively:

$$A_{bl} = \frac{\Omega_{eq}^{rx} R}{\cos \theta_i^{ac}} \frac{\Omega_{eq}^{tx} R}{\cos \theta_i^{al}} \qquad 2.4$$

$$A_{pl} = \frac{c\, \tau_{eff}}{2 \sin \theta_i^{ac}} \frac{\Omega_{eq}^{tx} R}{\cos \theta_i^{al}} \qquad 2.5$$

where A_{bl} and A_{pl} are the beamwidth limited and pulse length limited ensonified areas, Ω_{eq}^{tx} and Ω_{eq}^{rx} are the along-track transmit and across-track receive equivalent beamwidths, τ_{eff} is the effective transmit pulse length, θ_i^{al} and θ_i^{ac} are the acoustic incidence angles along and across-track, c is the sound speed and R is the slant range.

Some transmissions use a non-rectangular tapered pulse (e.g., Kongsberg Maritime, Reson, R2Sonic) to suppress the frequency sidelobes, better delimiting the bandwidth of the signal. In that case, the length of a rectangular pulse with the same energy as the tapered one should be used instead of the total pulse length (τ_t). This rectangular energy equivalent pulse length is commonly known as the effective pulse length (τ_{eff}).

The equivalent beamwidth (defined as equivalent aperture of a beam in Lurton, 2002) is the aperture of an ideal beam with a single lobe and constant beam pattern (0 dB), containing all the energy of the beam, as represented in Figure 2.1, where b(θ) is the beam pattern and θ is the angular offset between the considered direction and the maximum response axis. The -3 dB beamwidth (Ω_{3dB}) also illustrated in Figure 2.1, is a commonly used approximation for the equivalent beamwidth, which in uniformly weighted line arrays, might lead to a ~1 dB bias in the ensonified area estimation (Weber & Lurton, 2015).

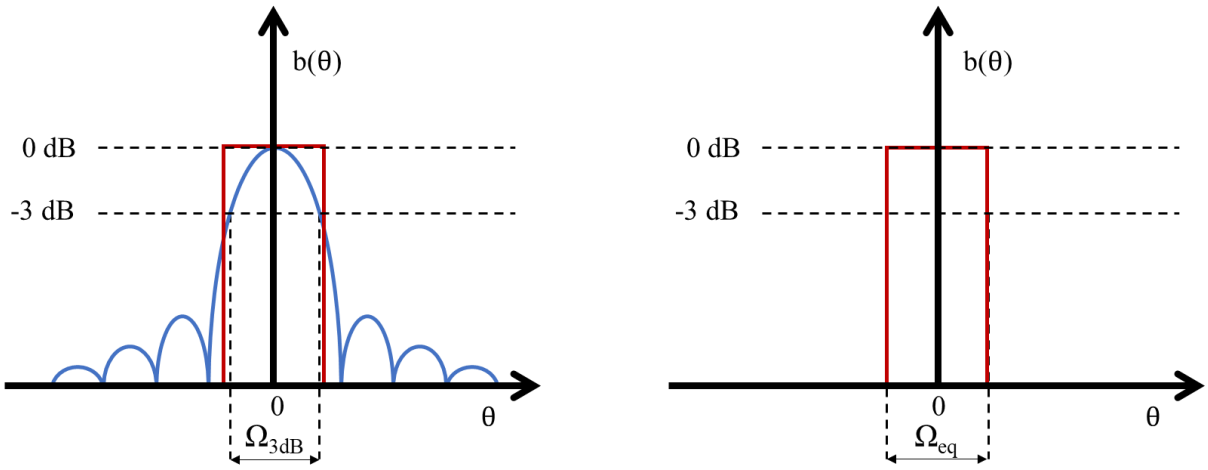

Figure 2.1: Relation between the equivalent beamwidth and the -3 dB beamwidth. The real beam is represented in blue while the ideal beam is represented in red. Adapted from Lurton (2002).

The incidence angle is defined as the angle between the acoustic ray and the normal to the seafloor at the intersection point. To derive the three-dimensional vector orthogonal to the seafloor implies that both the across- and along-track slopes must be considered when estimating the ensonified area.

By inspecting the geometry associated with the ensonified area illustrated in Figure 2.2, it is apparent that its complicated shape is simplified so it can be approximated by a rectangle when

using equations 2.4 and 2.5. Nonetheless, this model (or slight variations of it) has been applied in several research papers/theses (Amiri-Simkooei et al., 2009; Eleftherakis et al., 2018; Guimarães, 2020; Hammerstad, 2000; Hellequin et al., 2003; Hiroji, 2016; Lurton, 2002; Weber et al., 2018). Malik et al. (2018), compares the ensonified area obtained by applying this simplified model with the estimates obtained by employing the point-scatterer model developed by Ladroit et al. (2012). Both solutions matched quite well, except for the narrow angular range near the transition between the beamwidth limited and pulse length limited regimes, where more significant differences were observed, as shown in Figure 2.3. Even so, the usage of this simplified model is likely to have a negligible to small contribution (0.01 to 1 dB) in the magnitude of the uncertainty of the ensonified area estimate (Malik et al., 2018).

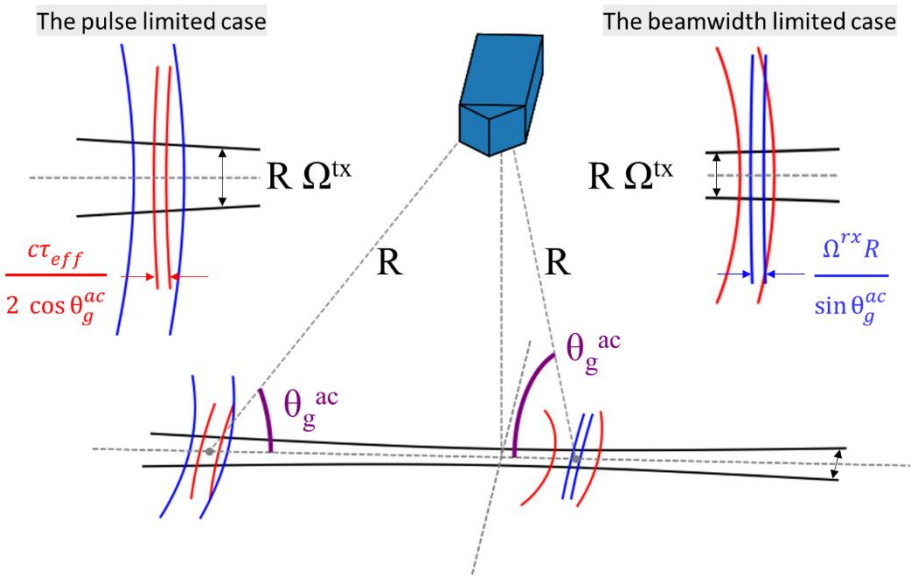

Figure 2.2: Ensonified area geometry over a flat seafloor for pulse length limited and beamwidth limited regimes, representing the transmit pulse projection (red), the transmit beamwidth footprint (black), the receive beamwidth projection (blue) and the across-track grazing angle θ_g^{ac} (purple). Along-track grazing angle is assumed to be 90°.

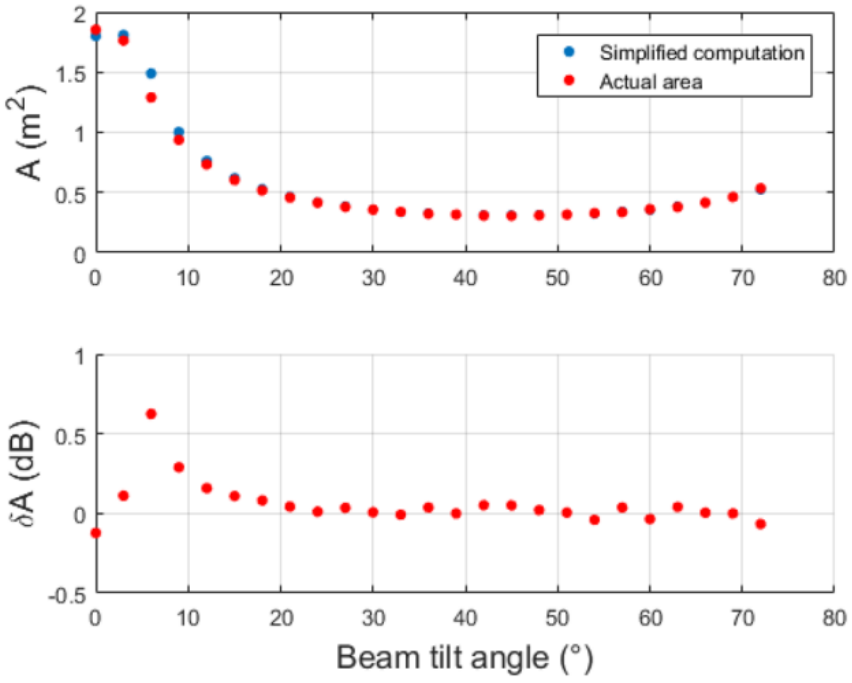

Figure 2.3: Comparing ensonified area estimates: simplified computation (equations 2.4 and 2.5) and Ladroit (2012) numerical simulation. Depth 50 m; pulse length 0.15 ms, beamwidth 1.5°. From Malik et al. (2018).

2.3. Transmission Loss

While it propagates throughout the water column, the intensity of a spherical acoustic wave weakens as a function of the traveled distance and the characteristics of the medium in what is usually referred to as transmission loss (TL) and defined as

$$TL = 20 \log_{10} \frac{R}{R_{ref}} + \alpha R \qquad 2.6$$

The first term is usually designated as the spherical spreading, where R_{ref} is typically 1 m, and the second as the attenuation, where α is the attenuation coefficient in dB/m (assuming the slant range R is in m).

The spherical spreading term is purely geometric, since it assumes a point source radiating omnidirectionally and that the energy, although conserved, is spread over spheres of larger and larger radii (Lurton, 2002).

Regarding the attenuation term, it is acknowledged that water is a dissipative medium i.e., it absorbs part of the acoustic energy through viscosity or chemical reactions (Lurton, 2002). The attenuation coefficient that controls this loss mechanism is dependent on the acoustic frequency, salinity, temperature, pressure and pH (Francois & Garrison, 1982a, 1982b). It is noteworthy that throughout the water column, α will change according to the characteristics of the medium. To address this added complication, Carvalho (2012) proposed a cumulative α, integrating the computed attenuation coefficients between the source and the depth of interest.

In the case of a monostatic sonar, since the acoustic wave has an outgoing and return path, the two-way transmission loss (2TL) is usually presented in the sonar equation:

$$2TL = 40\log_{10} R + 2\alpha R \qquad 2.7$$

For the specific case addressed herein, any imperfections in the estimated attenuation due to incorrect temperature (T) and salinity (S) observations will introduce a range-dependent bias in the S_b estimates. For a given T and S error the impact of this is notably more significant at higher frequencies due to the greater attenuation coefficients. Considering a sonar operating at 300 kHz, in a depth of 50 m with a ±75° wide coverage, an α = 74.5 dB/km (T=14°C, S=30 PSU) with 10% uncertainty, would result in a maximum 3 dB uncertainty for 2TL. In contrast, a 100 kHz system, at the same location, would present a maximum 1.3 dB uncertainty (α = 31.7 dB/km). In addition to T and S errors, the model used to estimate the previous attenuation coefficients (Francois & Garrison, 1982a), is estimated to be accurate within 5% for frequencies between 10 and 500 kHz

and the following oceanographic conditions: -2 < T < 22°C, 30 < S < 35 PSU and 0 < depth < 3.5 km.

2.4. Source Level and Receiver Sensitivity

The acoustic intensity emitted by a projector is a function of the provided power and of its own electro-acoustic efficiency and directivity gain (Lurton, 2002). Its source level (SL) is defined by the ratio between the source intensity at 1 m (I_o) and the reference intensity (I_{ref}) of a propagating plane wave with a root mean square pressure of 1μPa ($6.7x10^{-19}$ W/m² when water with density of 1000 kg/m^3 and a sound speed of 1500 m/s is considered), as defined in equation 2.8 (Weber & Lurton, 2015). SL is in dB re 1μPa at 1m.

$$SL = 10 \log_{10} \frac{I_o}{I_{ref}} \quad 2.8$$

The receiver sensitivity (M) of a hydrophone quantifies the efficiency of the electro-acoustic conversion, being defined as

$$M = 20 \log_{10} \frac{V_{1\mu Pa}}{V_{ref}} \quad 2.9$$

where $V_{1\mu Pa}$ is the resulting voltage for an incident acoustic pressure of 1 μPa and V_{ref} is the reference voltage of 1 V (Lurton, 2002). M is in dB re 1V/1μPa.

Both SL and M will be respectively modulated by the transmission and reception beam patterns adding an extra degree of complexity to these sonar equation terms which will be further discussed in Chapter 3.

2.5. Physical controls on bottom backscatter strength and angular dependence

If properly reduced, S_b is only dependent on the acoustic frequency and incidence angle, and on the physical properties of the bottom, potentially enabling remote seafloor characterization. Three relevant physical controls are the 1: water-bottom interface impedance contrast, 2: roughness of that interface and 3: modulations in impedance within the slightly sub-surface sediment.

The impedance of a medium is defined as the product of its sound speed and bulk density. The higher the difference in impedance of the media at an interface, the higher the ratio of reflected energy. Still, this concept by itself does not explain the occurrence of scattering. In reality, if the seafloor was completely flat, the acoustic energy would be either refracted or specularly reflected - an echo would be observed only if the incidence angle coincided with the reflection angle (i.e., normal incidence). The reality is that the seafloor is rough, in the sense that the water-bottom interface presents an elevation deviation from an average depth (Weber & Lurton, 2015). This interface roughness can be explained through a spectrum describing the power associated with the various spatial components of the relief, where the larger spatial scales determine the seafloor slope and the smaller scales, comparable to the acoustic wavelength, are responsible for the scattering phenomenon (Jackson & Richardson, 2007). In addition, since seafloor roughness is not necessarily isotropic, the roughness spectrum should be evaluated over two orthogonal dimensions, i.e., a two-dimensional roughness spectrum is considered (Jackson & Briggs, 1992; Briggs et al., 2005). A net result of this can be an apparent azimuth dependence (Lurton et al., 2018). It is important to acknowledge the frequency dependency of this phenomenon since the same roughness spectrum will output different degrees of scattering for distinct acoustic wavelengths.

Since the water-bottom interface impedance contrast is not infinite, energy will refract into the seafloor and potentially scatter from sub bottom interfaces or buried heterogeneities such as gas bubbles, shells and pebbles (Jackson & Richardson, 2007). This constitutes another physical control on S_b commonly called as volume scattering (Jackson et al., 1986). Volume scattering models require spectra describing the spatial fluctuations of the sediment properties and statistical descriptions of the discrete scatterers (Jackson & Richardson, 2007). Volume scattering is frequency dependent for two potential reasons: firstly, as with the surface scattering, different acoustic wavelengths will respond to different length scales of volume heterogeneity and secondly, perhaps more significantly, since it also depends on how deep the energy can penetrate into the sediment, it in turn is controlled by the sediment attenuation which increases with the acoustic frequency (Hamilton, 1972). Additionally, according to Snell's Law, if the incidence angle is greater than the critical angle (dependent on the sound speeds of the media that compose the interface), acoustic penetration into the seabed and the subsequent volume scattering are significantly reduced, only occurring due to mechanisms such as the evanescent wave (Jensen & Schmidt, 1987; Williams et al., 1989) and the scattering from the water-sediment interface surface roughness (Thorsos et al., 2000).

The aforementioned effects will have different contributions to S_b when distinct acoustic incidence angles are considered, as illustrated in Figure 2.4 (from Augustin et al., 1996). Near normal incidence, the backscatter will be dominated by the specular reflection contribution. Moreover, low interface roughness will contribute to a more pronounced and narrower specular peak, while high interface roughness will have the opposite effect (smaller and more smeared specular component). At oblique incidence, a combination of the volume scattering and interface roughness will be the most important contributors to the backscatter. If the water-bottom interface

presents a low impedance contrast, volume scattering gains importance, especially in the presence of a low interface roughness. After the critical angle, the volume scattering will no longer play a role and the backscatter will be solely controlled by the interface roughness. The described angular dependence of the S_b is commonly addressed as the angular response curve (ARC), for a specific seafloor type and acoustic frequency (e.g., Hiroji, 2016; Hughes Clarke, 1994, 2012).

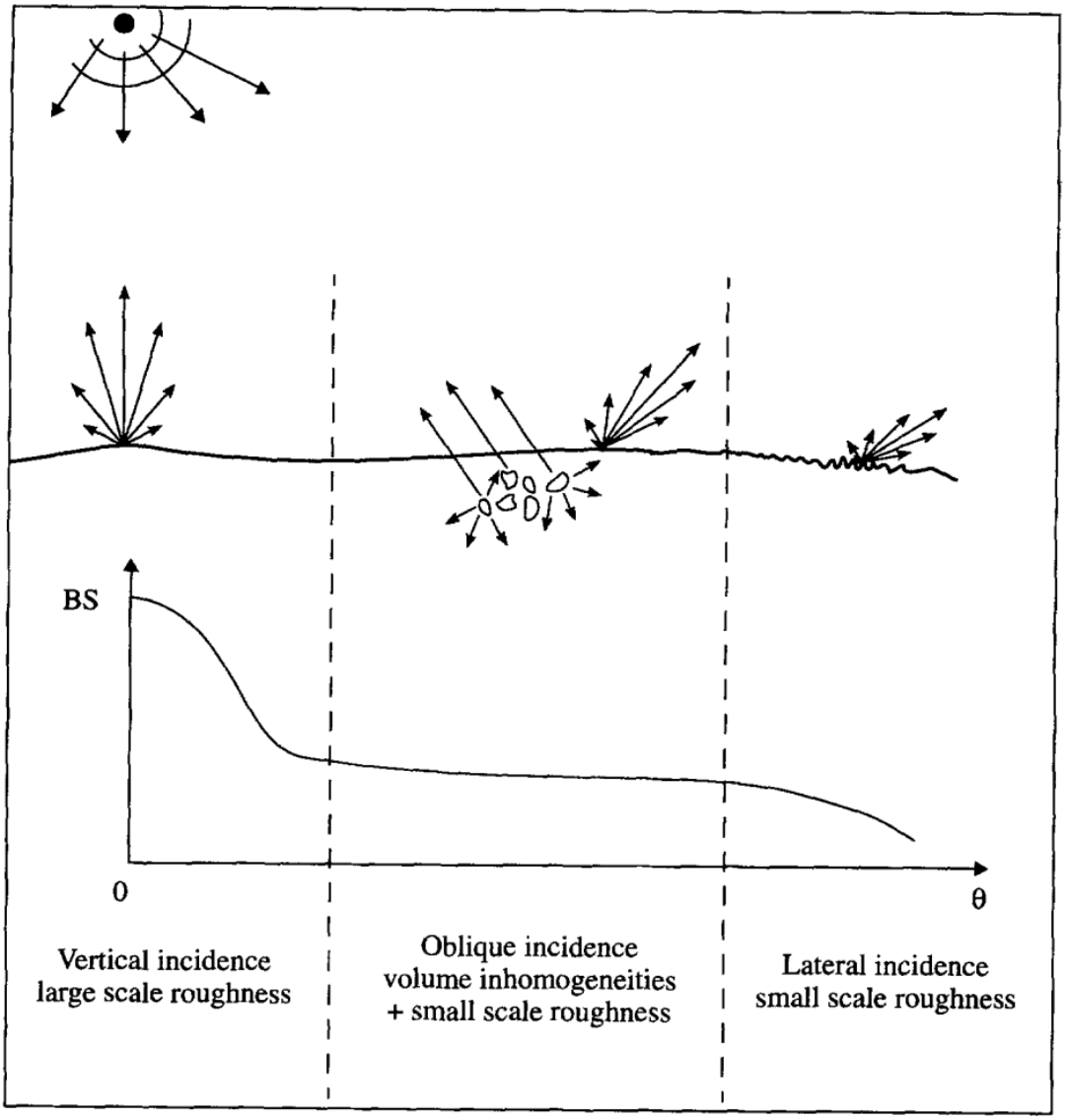

Figure 2.4: S_b physical controls and angular dependence. From Augustin et al. (1996).

3. BEAM PATTERN EFFECTS IN MULTIBEAM BACKSCATTER STRENGTH DATA

From the Chapter 2 discussion about the sonar equation, it is evident that to properly estimate S_b, it is essential to know SL and M for every ensonification direction, i.e., the transmit and receive beam patterns. This chapter will examine how the beam patterns are influenced by beamforming and beam steering, relating these processes with typical features of multibeam echosounder systems such as motion compensation and the usage of multiple transmit sectors.

3.1. Beamforming

Beamforming is the process of combining the individual contributions of the elements of an array to achieve a desired spatial directivity, either on transmission or reception. For multibeam echosounders with the classic Mill's cross design, on transmission the result is a main lobe, narrow in the along-track direction and wide athwartships. Conversely, on reception, the main lobe is narrow athwartships and wide along-track. In both cases, the shape of the main lobe will depend on the directivity of each of its elements and the spacing between them, and on the acoustic wavelength with respect to the physical dimensions of the array (Lurton, 2002). The larger the length / width of the transmit array (L_{tx}, W_{tx}), the narrower the transmit main lobe will be in the fore-aft / across-track direction. For the receive array, a similar relation can be established. However, its length (L_{rx}) is aligned with the port-starboard direction and its width (W_{rx}) with the fore-aft direction. Consequently, a larger L_{rx} / W_{rx} results in a narrower receive main lobe in the across-track / along-track direction. An illustration of the main dimensions of a MBES with a Mill's cross design is provided by Figure 3.1.

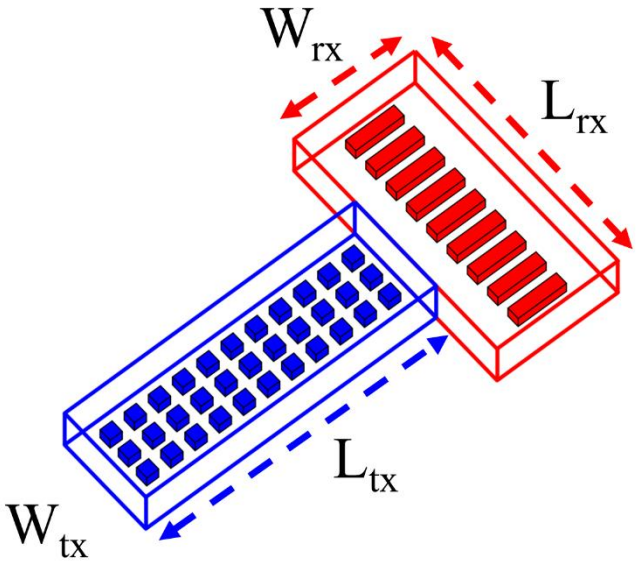

Figure 3.1: Transmit and receive arrays of a MBES with a Mill's cross design, their relevant dimensions. The two-dimensional disposition of the elements of the transmit array allows it to be steered both along and across-track.

The main lobe can be steered by an angle θ_s to a desired direction (by using time delays or phase shifts on each element), which will make it wider by a factor of $1/\cos \theta_s$ and reduce its peak SL / M, while preserving the basic shape of the beam pattern (Lurton, 2002), as portrayed in Figure 3.2.

The directivity of the transducer results from the mathematical product of the beam pattern of the elementary transducer and the beam pattern of a line array of point omnidirectional transducers (Lurton, 2002). Since the transducer elements commonly present a smaller directivity to the sides, any amount of steering applied to the array will result in a beam with a smaller peak SL or M. As the across-track steering angle range used for receiver arrays is typically within ± 65°, this effect results in an evident peak M roll-off for the heavily steered beams. Identically, when the transmit array is steered, the same process applies. Although the along-track steering applied to the transmitter array is smaller (±3° for pitch compensation or ±10° for yaw

stabilization), it will still cause a peak SL roll-off. Also, when the transmitter array is capable of performing across-track steering (e.g., multi-sector transmission), as higher steering angles are commonly used, the SL roll-off becomes more evident.

Additionally, to perform sidelobe suppression, it is common to unevenly weigh the contribution of each element of the array (known as amplitude shading), which will further influence the SL and M beam pattern shapes (Harris, 1978).

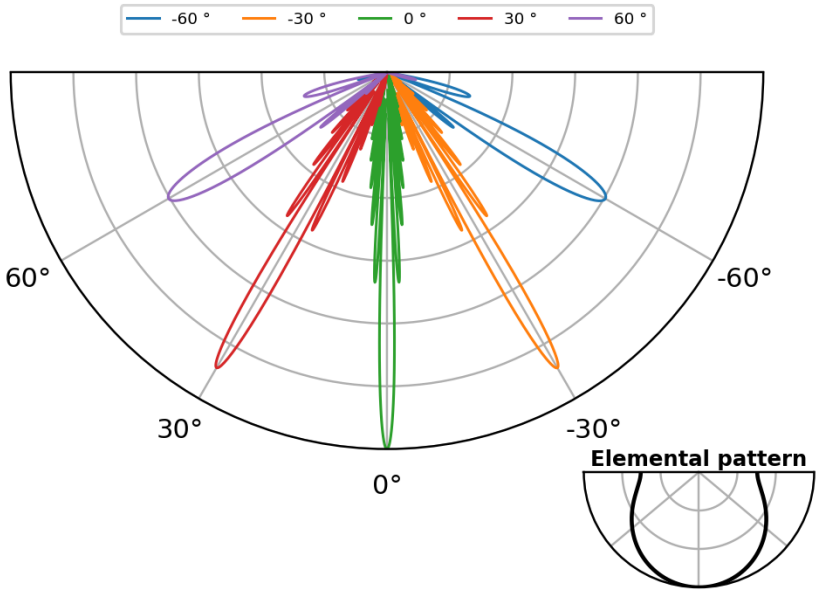

Figure 3.2: Beam pattern dependence on steering, based on an unshaded discrete line array of piston transducers. Note that the beam gets wider and the directivity smaller as steering increases (exaggerated effect for better visualization). The elemental pattern is represented in the inset.

The SL and M beam patterns will be heavily dependent on the beamforming process and are typically described in a sonar referenced frame, as opposed to vertically referenced, since few MBES are designed to totally compensate for the vessel's motion.

Considering the transmit beam pattern, as Hiroji (2016) points out, the SL across-track will usually peak near the across-track steering direction (0° in the ACS for a single sector, but up to 60° for some multi-sector systems) and diminish to either side, rolling off inboard and outboard depending on the across-track beam width (typically ± 70° for single sectors, but only ±20° or less for multi-sector systems). While there is also a much more rapid intensity variation along-track, as the transmit pulse annulus extends fully fore-aft along the entire width of the beam, it ends up being integrated and described within the equivalent beamwidth (Figure 3.3).

Conversely, the along-track receive beam pattern presents a peak sensitivity at the minimum sonar relative along-track angle but noticeably drops both forward and aft (Figure 3.4). That drop off reflects the fore-aft dimension of the receiver and is by design (to reduce sensitivity to echoes outside the likely transmission footprint). Again, it of course also varies more strongly athwartships, but that is not relevant when the beam directivity is further constrained by the transmit pulse length, impacting only near nadir beams where it is then managed in the equivalent beamwidth estimation.

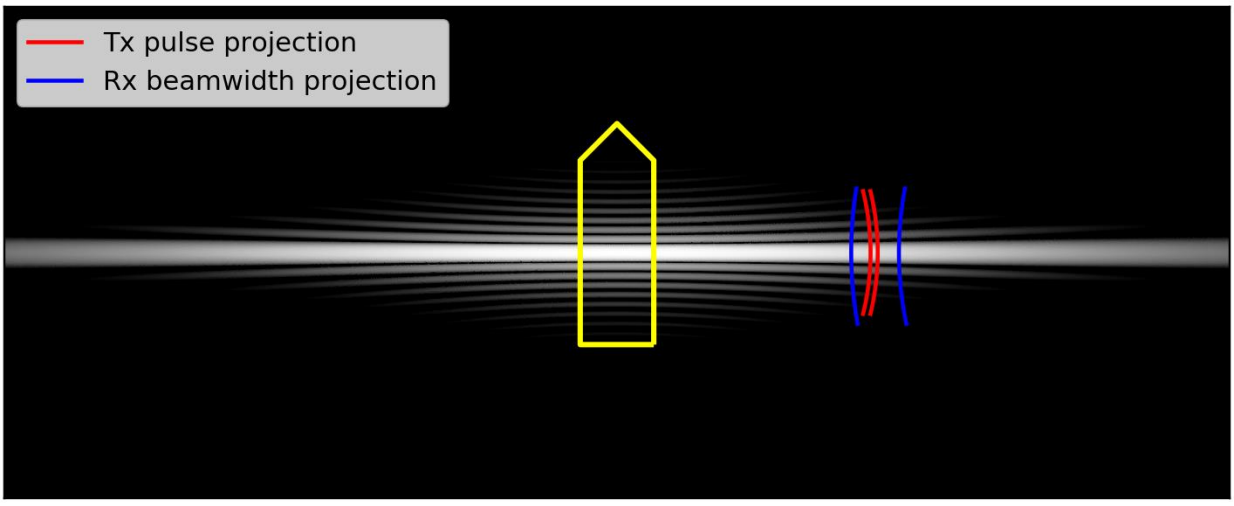

Figure 3.3: Projection on a planar seafloor of an unsteered transmit beam, overlapped with the limits of the transmit pulse (red) and receive beamwidth (blue) projections.

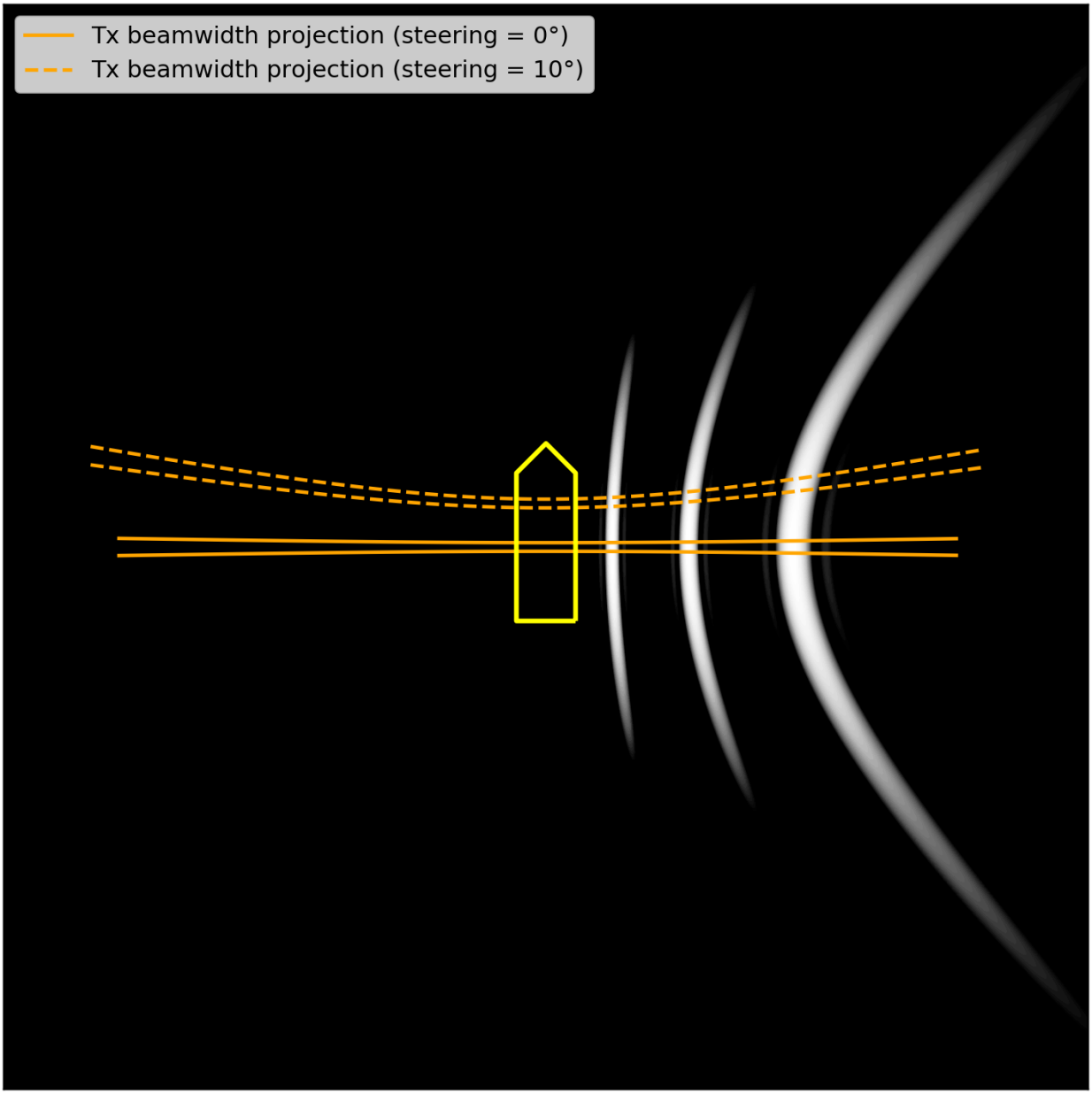

Figure 3.4: Projection on a planar seafloor of the receive beam pattern (grayscale), with different across-track steering (15°, 30° and 45°), overlapped with the limits of an along-track steered (yellow dashed line) and unsteered (yellow solid line) transmit beamwidth footprint.

All the above-described beam pattern dimensions depend on array sizes relative to the acoustic wavelength. Thus, as with the attenuation term, a changing T and S will impact this. Typical scales of sound speed variability within a single survey area are generally less than 1%

(~15 m/s) which changes the beam patterns by no more than ~0.05 dB. Even taking a sonar calibrated in an acoustically fast water mass (e.g., equatorial tropical saltwater: ~1520 m/s), to a slow water mass (e.g., cold freshwater lake: 1460 m/s) still only changes the wavelength by 4% with a corresponding impact on the beampattern of less than 0.2 dB.

3.2. Motion compensation and dual swath

The goal of motion compensation is to provide a uniform sounding density, regardless of the vessel's attitude, ultimately preventing coverage gaps and promoting compliance with bathymetric surveying standards (e.g., International Hydrographic Organization, 2020; Land Information New Zealand, 2020). When no motion compensation is used whatsoever, every beam vector is fixed in a sonar referenced frame (ACS), which itself rotates with respect to a vertically referenced frame (SCS) as a function of the vessel's roll, pitch and yaw. Achieving full motion compensation means that each beam can be stabilized in a vertically referenced frame, thus allowing a more stable swath width and a more even sounding coverage, both along- and across-track.

For the purpose of this research, the manner of compensation needs to be understood so that the variations in sampling the transmit and receive beam patterns are properly accounted for in the S_b reduction. The data that is handled in this thesis is from three different multi-sector multi-swath MBES - Kongsberg Maritime (KM) EM710, EM712 and EM2040P - all of which attempt roll, pitch and yaw stabilization while using dual swath (as defined in Subsection 3.2.4). Specific differences between them will become apparent as they have different transmitter designs: the EM710 and EM712 both have a single two-dimensional transmitter steerable in 2 axes while the EM2040P uses 3 separate one-dimensional line transmitters that can only be steered along-track.

3.2.1. Roll compensation

Roll compensation is usually implemented by dynamically steering the receive beams with respect to the receive transducer, ensuring that the beam maintains a stable orientation with respect to the local vertically referenced frame (Figure 3.5 A). While this is an initial adequate solution for dealing with across-track sounding density, it also means that, from swath to swath, the same roll-stabilized receive beam will be sampling a different part of the receiver sensitivity pattern (M) as well as intersecting the transmit beam pattern at different sonar referenced across-track angles with different source levels. This will impact the proper reduction of the bottom backscatter strength data, implemented in Chapter 5. To mitigate the transmission aspect of this effect, the transmit beam would also have to be roll-stabilized. Even then, the transmit sector pattern would not be exactly the same, as a different across-track beam steering would be involved.

3.2.2. Pitch compensation

Pitch compensation is employed to promote a consistent along-track sounding density, as opposed to the scenario displayed in Figure 3.5 B. It is performed by steering the transmit beam, stabilizing its orientation with respect to a local horizontal plane. However, any steered beam assumes the form of a conical surface and its intersection with a planar seafloor is no longer a straight line. Hence, adjacent pitch-stabilized swaths would not necessarily be parallel, resulting in a residual uneven along-track sounding density for some beams. Nevertheless, pitch compensation is still used to stabilize swath spacing. Typically, an across-track angle off nadir is chosen for optimal compensation – the inner portion of the swath is undercompensated while the outer swath is overcompensated (reference angle in Figure 3.5 C). Similarly, as happens in roll compensation, steering the transmit beam implies that its intersection with the receive beams will

occur at different sonar referenced along-track angles, with different receiver sensitivities (Figure 3.4). Again, this will impact the proper reduction of the bottom backscatter strength data, implemented in Chapter 5. If the receive beams were pitch-stabilized (a feature only possible in a two-dimensional receive array such as the Simrad ME70), this extra complication would be significantly reduced - once more, the beam steering process would (slightly) affect the along-track receive beam pattern.

3.2.3. Yaw compensation

As the vessel changes heading, sounding density will be uneven in the outer regions of the swath: gaps on one side and clusters on the other (Figure 3.5 C). This problem is more evident in deeper waters since, between swaths, greater changes in yaw might occur. Yaw compensation aims to address this complication. However, when a transmit beam is steered along-track, both sides of the swath move in the same direction, while the desired effect would be to rotate the swath's azimuth or, at least, move one side aft and the other side forward (or vice-versa). Unfortunately, there is no mechanism to electronically perform yaw compensation with a single transmission. To deal with this issue, the solution adopted by some multibeam echosounders (e.g., KM and more recently Atlas and Wärtsilä) is to split the transmission into multiple transmit sectors. Each sector's transmit beam can then be individually steered along-track, allowing to place its sub-swath along an ideal swath line, usually orthogonal to an average heading (Figure 3.6 A), thus achieving yaw compensation (Figure 3.6 B). Each sub-swath steering will be typically optimized for its center beam. Hence, the larger the number of transmit sectors, the better the overall yaw stabilization will be, since each sector's soundings will be closer to the ideal swath orientation (Figure 3.6 C1-C4). Analogously, pitch compensation will also benefit from multiple transmit sectors.

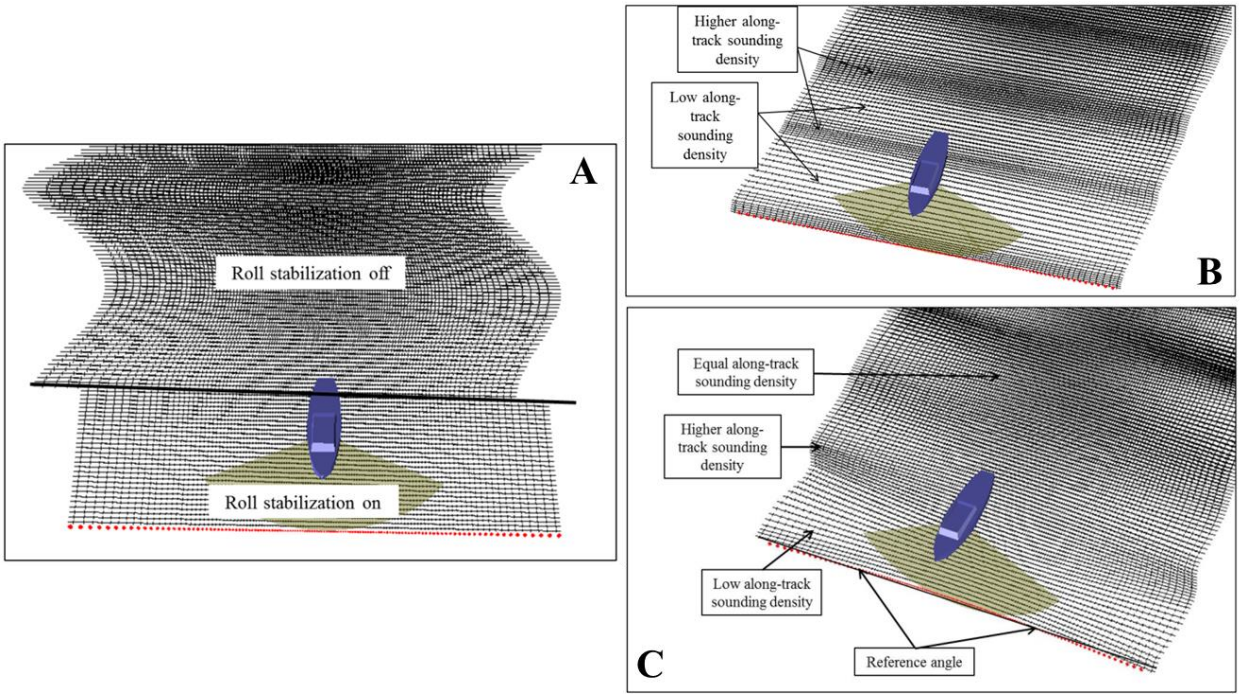

Figure 3.5: A: Roll compensation; B: Along-track sounding density variations due to absence of pitch compensation; C: Single sector sounding density with roll and pitch stabilization without yaw stabilization. From Hiroji (2016).

Similarly, as described for pitch compensation, the along-track steering of each sector's transmit beam will result in intersections with the receive beams at different sonar referenced along-track angles, resulting in irregular sampling of the SL and M patterns. Notably, the amount of along-track steering utilized in yaw stabilization (up to ± 10°) is typically much larger than that used in pitch stabilization (usually ± 3°). The added complication is that each sector will have its own SL beam pattern and, since each sector needs to operate with a different acoustic frequency to avoid interference, the M beam pattern will also be sector dependent, as illustrated by Figure 3.7 showing the M and SL values per beam estimated by KM for a multi-sector MBES. Note that the M is only calculated for across-track, not along-track. Once again, these complications must be properly accounted for in the reduction of the S_b data.

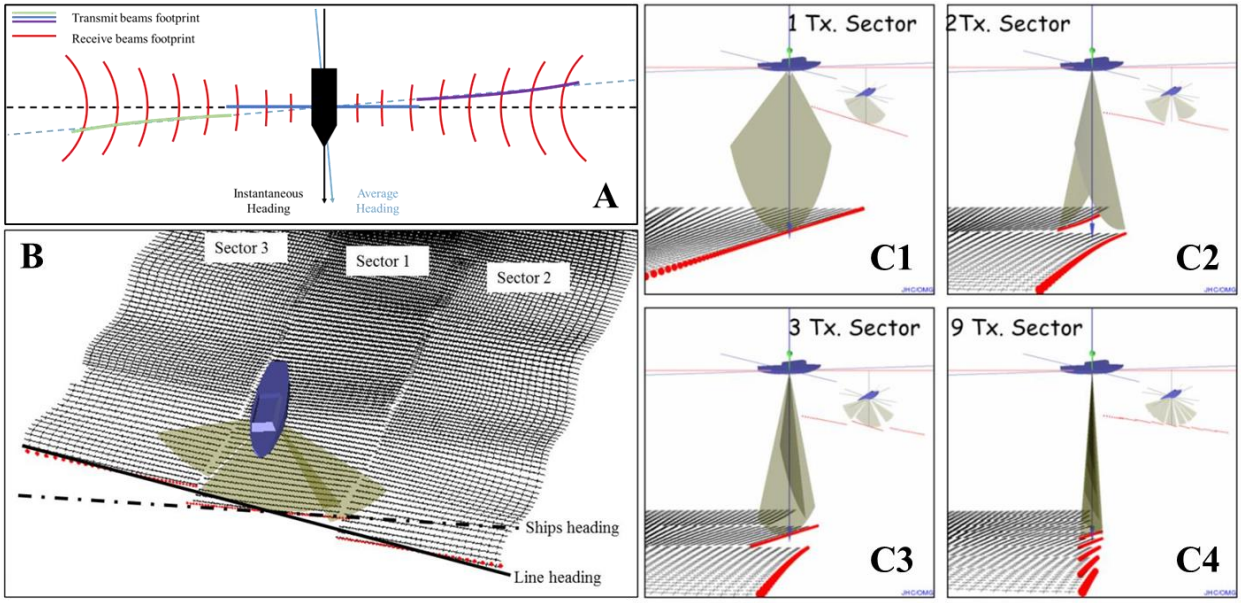

Figure 3.6: A: Addressing yaw compensation by individually steering each transmit sector to obtain an ideal swath, orthogonal to an average heading; B: Multi-sector sounding density with roll, pitch and yaw stabilization – from Hiroji (2016); C1-C4: The larger the number of transmit sectors the better the overall yaw stabilization as each sector's soundings will be closer to the ideal swath orientation – from Hughes Clarke (2020).

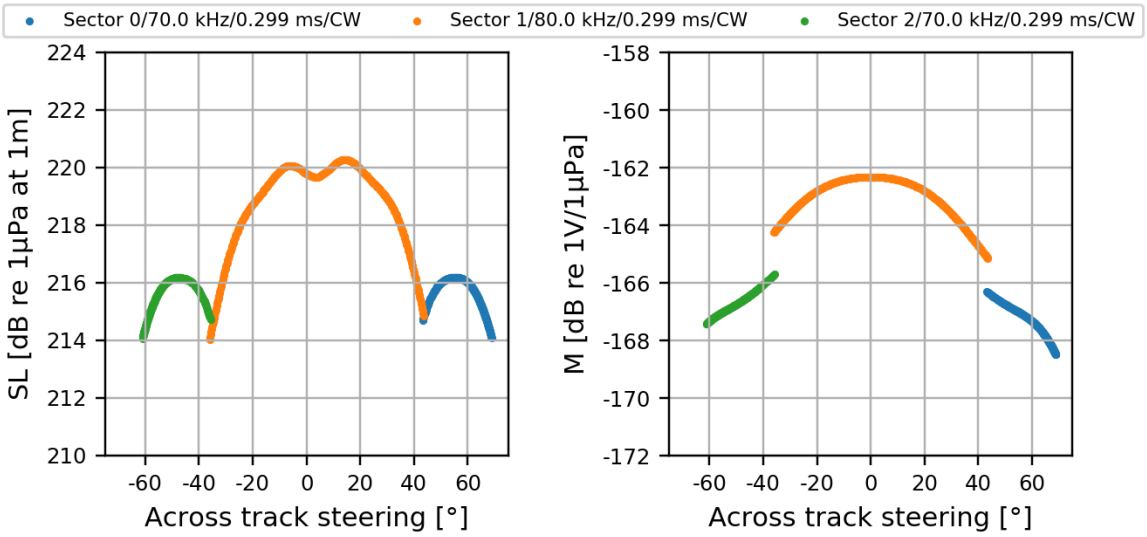

Figure 3.7: Manufacturer-provided SL and M estimates (extracted from .KMALL files), sorted by across-track steering angle, for a particular swath of an EM712, operating in Very Shallow mode (70-100 kHz) and dual swath (three sectors per swath).

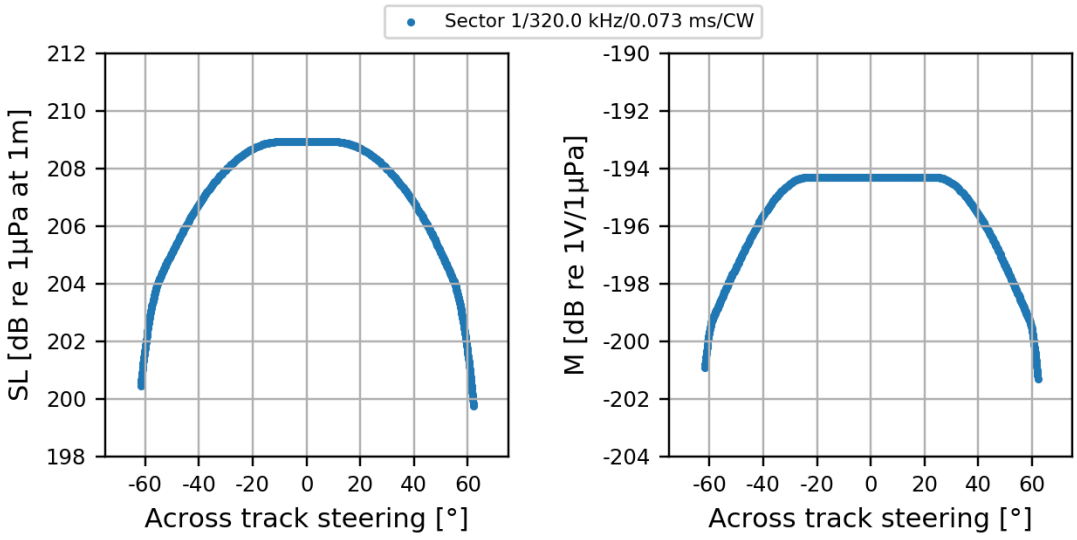

Figure 3.8: Manufacturer-provided SL and M estimates (extracted from .KMALL files), sorted by across-track steering angle, for a particular swath of an EM2040C (Mk I receiver), operating in Shallow mode (300 kHz) and dual swath (single sector per swath).

Figure 3.7 and Figure 3.8 allow one to compare the manufacturer-provided SL values per beam, for a particular swath, for MBES operating with a multi- and single-sector transmission. For the multi-sector case, the roll-off from the steering direction outwards occurs rapidly (~6 dB in ~40° for the center sector), while for the single-sector system the decrease in SL is considerably less steep (~9 dB in ~60°). The narrower SL roll-off is compatible with the multi-sector MBES having a larger W_{tx}. Furthermore, the capability to perform both along and across-track steering requires the transmitter to have a two-dimensional matrix of elements (as is the case for the illustrated EM712).

The greater along-track transmit steering used for yaw compensation makes the intersection of the transmit and receive beam patterns occur at higher sonar referenced along-track angles. Therefore, the receiver beam pattern will be sampled at a region with a smaller M, as can be understood from Figure 3.4. The extracted manufacturer-provided M estimates applied to an

EM2040P, binned by along-track angle (Figure 3.9), supports this hypothesis, as a M roll-off is clearly identified. In contrast, the same analysis for an EM712 (Figure 3.10) does not show this, suggesting that along-track M roll-off is not compensated for.

3.2.4. Dual swath

Even with full motion compensation, higher survey speeds and/or wider swaths might result in a reduced along-track sounding density due to larger two-way travel times and thus wider along-track spacing between swaths. To deal with that, some sonars implemented the capability of using multiple swaths per transmit cycle, typically two, commonly known as dual swath. Even though it still utilizes the same geometry of interaction between the transmit and receive beams, using dual swath requires considering more transmit sectors with their unique associated SL and M beam patterns, adding yet another layer of complexity to S_b estimation. Figure 3.11 illustrates manufacturer's estimates for the SL and M for two subsequent profiles, showing how different the beam patterns can be between swaths.

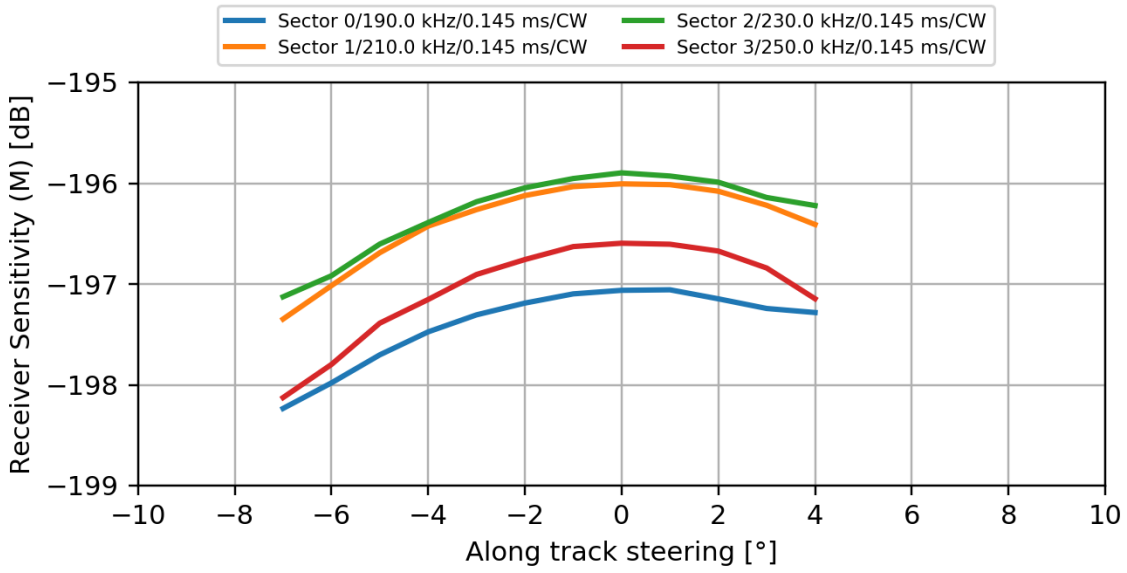

Figure 3.9: Average manufacturer-provided M, sorted by along-track steering angle, applied on an EM2040P (extracted from .KMALL files), operating in Shallow mode (200 kHz) and dual swath (two sectors per swath).

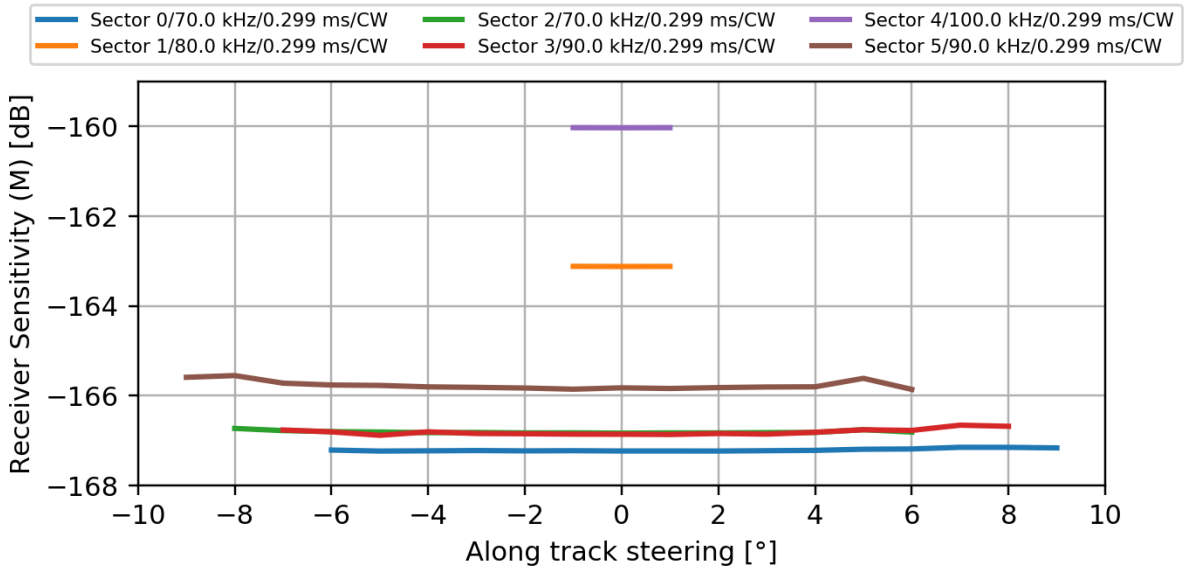

Figure 3.10: Average manufacturer-provided M, sorted by along-track steering angle, applied on an EM712 (extracted from .KMALL files), operating in Very Shallow mode (70 kHz) and dual swath (two sectors per swath).

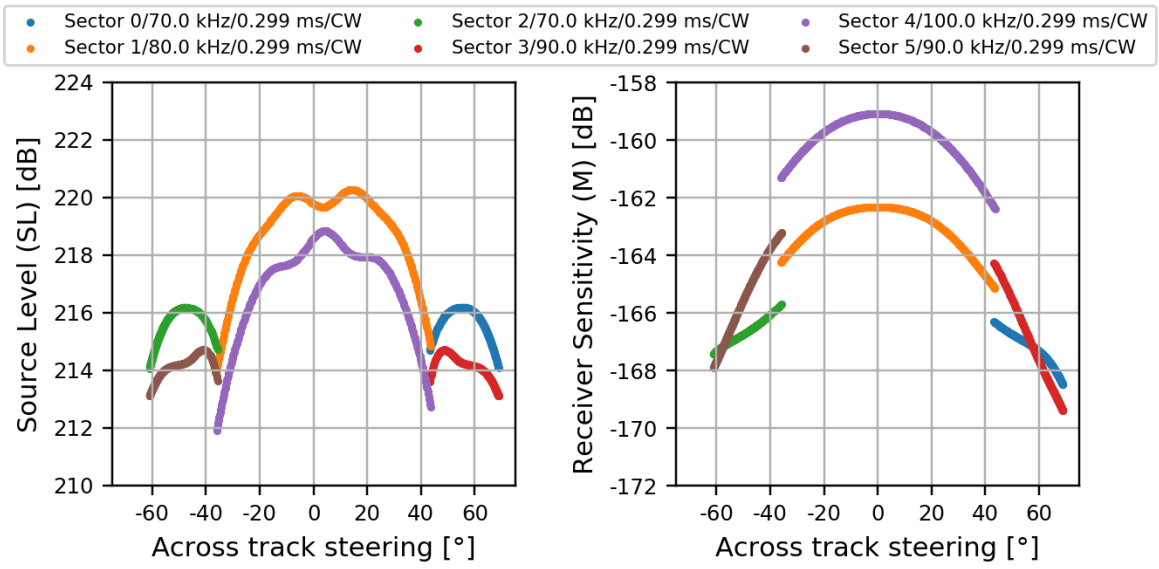

Figure 3.11: Manufacturer-provided SL and M estimates, sorted by across-track steering angle, for two subsequent swaths of an EM712 (extracted from .KMALL files), operating in Very Shallow (70-100 kHz) mode and dual swath (three sectors per swath).

4. BOTTOM BACKSCATTER STRENGTH CALIBRATION

To extract bottom backscatter strength estimates from received acoustic intensities, assumptions regarding environmental and sonar operational parameters, such as the attenuation coefficient throughout the water column, source level, receive sensitivity and pulse length, are required. Since any one or all of these could have an associated bias, the resulting S_b estimates will ultimately become a relative measure with respect to an arbitrary and unknown reference. The net result is that S_b estimates derived from different sonars, even if from the same manufacturer/model, will be different. As an example, Hughes Clarke et al. (2008) provides, for the same location and over a course of three years, the mean S_b obtained with five KM EM3002 MBES, mounted in different platforms and operating at 300 kHz. The departure of those estimates from a reference value varied between -3 and -9 dB, emphasizing the poor repeatability of the bottom backscatter strength reduction process when data from different sonars is compared.

In notable contrast to the existing standards for bathymetry establishing the maximum acceptable uncertainty for a survey (e.g., International Hydrographic Organization, 2020; Land Information New Zealand, 2020), the required accuracy of S_b estimates is not currently defined by specific guidelines. Requirements should reflect the users' needs, which for seabed backscatter have never been formally defined. In practice, the marine geologist or ocean engineer would want to be able to distinguish typical variations in seafloor sediment that impact their analysis. As a guide, the range of S_b values for common seafloor sediments should be examined. A benchmark study is the Applied Physics Laboratory - University of Washington (APL-UW) model (APL-UW, 2014), which relies on the model described in Jackson et al. (1986). For frequencies below 100 kHz, the APL-UW model predicts that, while the average difference between the mean S_b for the

full range of typical sediments (gravels to clays) can be up to 40 dB, sediments that are most common on the continental shelf (medium sands to silts – Swift, 1974) exhibit a far reduced range of S_b. At 100 kHz, the average difference between their ARCs, for the entire grazing angle range, can be as little as ~ 2dB.

Lucieer et al. (2018), in a paper discussing users' expectations for MBES S_b data, suggests that 1 dB of accuracy in S_b estimates should be adequate to discriminate between sediment classes.

While 1 dB may be a desired level of accuracy, as pointed out by Malik et al. (2018), even though some manufacturers predict the response of their sonars and provide estimates of S_b, the incomplete knowledge of sonar parameters - source level and receiver sensitivity - has a detrimental and unpredictable effect in the bottom backscatter strength determination and can result in prohibitive biases (> 6 dB), well in excess of the Lucieer et al. (2018) proposal. To address this issue, some form of practically achievable calibration is required.

4.1. Early efforts to obtain calibrated bottom backscatter strength

Over the last ~70 years, several pioneering studies have used calibrated sonars to estimate S_b. Each of these studies has emphasized the need to relate their results to a well-known reference.

Urick (1954) estimated S_b of several sediment types at a harbor bottom with a piston transducer, over wide range of grazing angles and using frequencies between 10 and 60 kHz. The need to compare the results with a reference target – in his case a three-foot spherical mine case - was strongly emphasized.

Boehme et al. (1985) estimated S_b at grazing angles ranging from 2 to 10° over frequencies of 30-95 kHz in San Diego, California. Prior to the data collection, at a calibration facility, the

relationship between the projector maximum response axis SL and the transmit electrical current was established and the projector and hydrophone directivity functions were measured.

Stanic et al. (1988) in Panama City, Florida and Stanic et al. (1989) in Jacksonville, Florida, used a pair of broadband parametric sources and a 12 hydrophone two-dimensional spatial array, composed of omnidirectional elements, to derive S_b. The observations were performed at between 20 and 180kHz at grazing angles spanning from 5 to 30°. Both the projectors and hydrophones were previously calibrated.

Gensane (1989), collected S_b on sand, gravel and clay bottoms, using frequencies between 8 and 40 kHz at grazing angles from 4 to 90°. For that purpose, a device called *Reverberometer* was created. It included a parametric array as the source and the reception was handled by a hydrophone. Both were previously calibrated.

Notably, all of these studies have utilized a system best calibrated at its boresight, after which they then chose to mechanically rotate the source/receiver to achieve a wide range of grazing angles (and in some case azimuths). For the case of a MBES, however, the wide range of angles is achieved without rotation, but one then has to more confidently deal with calibration over a wide range of boresight relative angles - the beam pattern, rather than just the boresight SL.

All these historic measurements emphasized that there is a need to be confident in the calibration. To that end, various approaches to achieving that calibration have been proposed. There are three main end member solutions:

- using an object with a known target strength as a reference, thereby estimating the calibration of the combined MBES source level and receiver sensitivity (Section 4.2).

- separately measuring the MBES source level and receiver sensitivity, using respectively calibrated hydrophones and sources, and thereafter combining them (Section 4.3).
- using a natural seabed, that has previously been measured using a different calibrated system, as an extended surface target to be able to calibrate MBES against in the field (Section 4.4).

Each of these approaches has been attempted and has their own advantages and limitations. These will be discussed in the next three sections.

4.2. Using reference targets for echosounder calibration

Reference targets are widely used to calibrate sonars employed in fisheries research (Demer et al., 2015; Foote et al., 1987). The target strength – the proportion of the incident intensity that is backscattered – of a spherical object with a known composition can be very precisely modelled as a function of the acoustic frequency (MacLennan, 1981). Concurrently, if that sphere is small enough to completely fit within the main lobe of an echosounder, an estimate of that target strength can be derived and compared to the modelled value. Assuming all the other terms of the sonar equation have been perfectly reduced, the difference between the estimated and modelled target strengths would be the required correction to combined transmit/receive beam pattern (SL + M) at that vector in a sonar referenced frame (ACS). To be able to know where the target is with respect to the sonar reference frame, a split-beam echosounder (SBES) is popularly used since its transducer is typically divided into four quadrants, enabling the measurement of the phase difference between quadrant pairs, thus providing the ability to resolve the angular position of a

target within a beam, usually in the alongship and athwartship directions. In this manner, SL + M can be calibrated either on or off the acoustic main response axis.

Reference targets have also been used to calibrate MBES. To do so, the MBES must also be split beam on two axes. Most MBES utilize a split aperture across-track (in order to achieve phase detection), but the receiver is not split in the fore-aft direction. In contrast, on specialized fisheries MBES like the Simrad ME70 and the Simrad MS70, the receiver is two dimensional and thus fore-aft as well as across-track target angles can be estimated.

Because of this, both the ME70 and the MS70 can be calibrated at sea, in favorable weather, in ~3 and ~1 hours, respectively (Ona et al., 2009). While possible, the process described in Ona et al. (2009) required using several winches to slowly move a target sphere over each of the MBES beams - 500 beams on the MS70 and 21 beams on the ME70. With the MS70, positioning the sphere in the outer beams (>30° relative to vertical) was difficult, especially in inclement weather. Furthermore, to cover the available center frequencies (70 – 120 kHz), two target spheres were required. It is not desirable two deploy the two spheres simultaneously since interference might occur, further contributing to the logistical complexity of the operation.

Employing the reference target approach to calibrate MBES without fore-aft split-beam capability has also been performed. These attempts normally rely on the use of a controlled environment, such as a sea well or tank, on the positioning of the target sphere relative to the array mostly by geometric considerations, and on accurate rotations of the transducer (Chu et al., 2002, 2003; Cochrane et al., 2003; Foote et al., 2005; Lanzoni & Weber, 2012). The arrays are mounted in such a way that the acoustic axis lies approximately on a horizontal plane and the reference target is within the beam. Then, by rotating the transducer around its vertical axis and/or by varying the depth of the target, the beam pattern can be estimated as a function of the elevation and

azimuthal angles between the target and the acoustic axis. The Foote et al (2005) implementation is depicted in Figure 4.1.

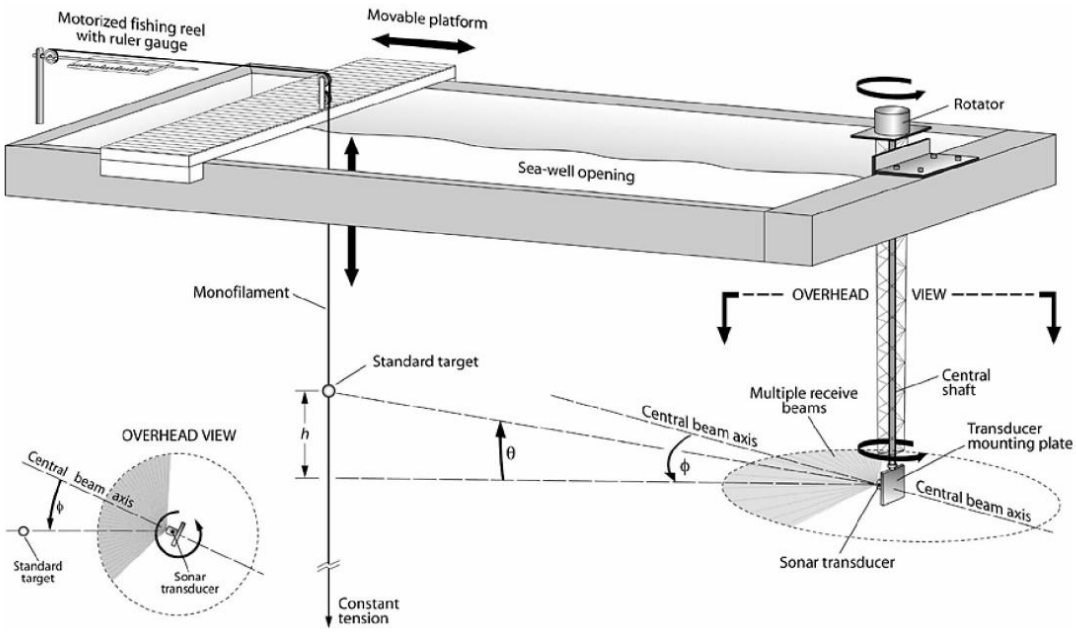

Figure 4.1: Schematic diagram of a sea well configured for calibrating a MBES using a reference target. The azimuthal angle (ϕ) is measured on an approximately horizontal plane containing the multiple beams. The elevation angle (θ) is controlled by changing the depth of the sphere (influencing h) and measured on a plane perpendicular to the horizontal, containing the receive array acoustic center and the reference target. From Foote et al. (2005).

While acoustic calibrations performed in a laboratory environment allow one to accurately determine the beam pattern (Lanzoni & Weber, 2012), having access to such facilities is not normally the case for the usual MBES end user. Furthermore, they require removing the sonar from its platform, potentially neglecting the effects of interference from other systems mounted on the vessel, as well as the potential impact of the hull and mounting frame on back-radiated sound. Moreover, depending on the size of the tank, the reference target might be in the sonar's near field, requiring some compensation to obtain a valid far field calibration (Foote et al., 2005; Wendelboe

et al., 2012). Also, in smaller tanks, reflections from the surface and/or the walls might hinder the calibration process.

Avoiding these complications, Lanzoni & Weber (2011) proposed a field calibration methodology relying on positioning a reference target with a SBES operating in passive mode, as shown in Figure 4.2. The positional offsets between the SBES and the MBES, and the angles/ranges measured by the SBES, allow one to determine the reference target angles in the MBES reference frame. Still, to fully determine the combined transmit/receive beam pattern of the MBES, the target sphere must occupy several along and across-track angles within each beam – and most modern MBES have several hundreds of beams. The ease of executing this operation will also depend on the relative orientations between the beam to calibrate and the SBES maximum response axis.

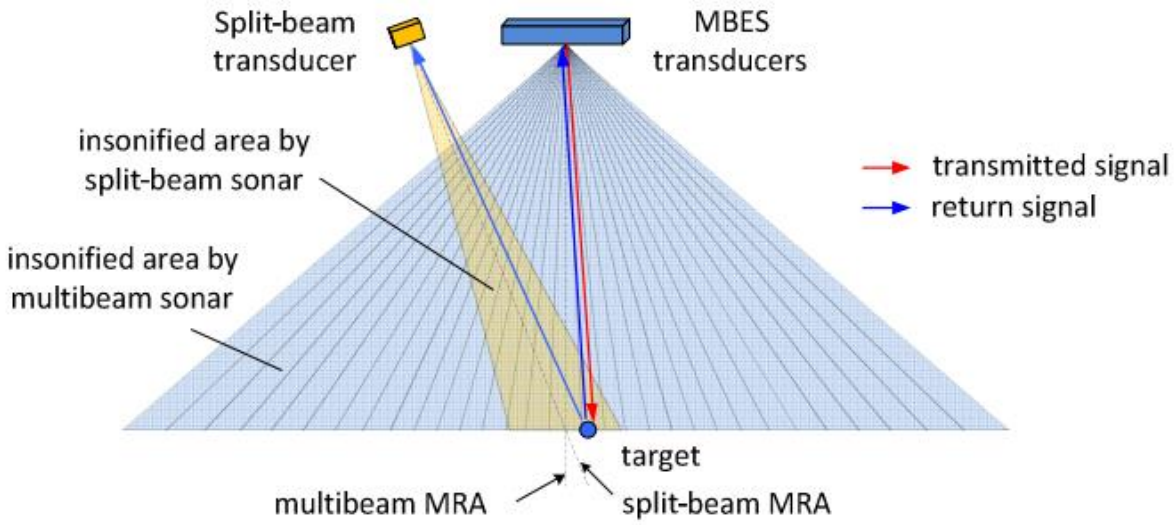

Figure 4.2: Field calibration methodology, using a SBES to position the reference target. From Lanzoni & Weber (2011).

So far, only target spheres have been mentioned as calibration targets. Alternately, MBES calibration can be addressed by using a target with a different form factor, e.g., a curtain composed

of chain links, as depicted in Figure 4.3 (Heaton, 2014; Heaton et al., 2017). In contrast to the target sphere calibration technique, this method provides an extended reference target analogous to the seafloor. Considering that obtaining S_b is the final objective, using a target with a morphology similar to the seafloor could reduce the impact of calibration errors (e.g., ensonified area calculation systematic errors cancelling out). To characterize the chain curtain backscattering properties, a calibrated SBES was used and angular dependence was not detected (Heaton, 2014; Heaton et al., 2017). Unlike the other documented calibration techniques, this technique requires less precision in positioning the target. Still, the inherent logistical requirements make this procedure hard to implement in the field since the curtain needs to be hung vertically and the MBES transducers must be mounted on a rotating mechanism (such that the transmit beam is roughly in a horizontal plane), ensuring that every beam (in turn) hits the target, as illustrated by Figure 4.4. Ultimately, a MBES beam pattern correction as a function of the beam steering angle is generated, allowing it to provide calibrated S_b estimates. The difference between these and the simultaneously acquired S_b from a calibrated SBES (same frequency and grazing angle of 45°) were under 1.5 dB (Heaton et al., 2017).

Figure 4.3: Jack-chain extended reference target: entire target (left); close up (right). From Heaton (2014).

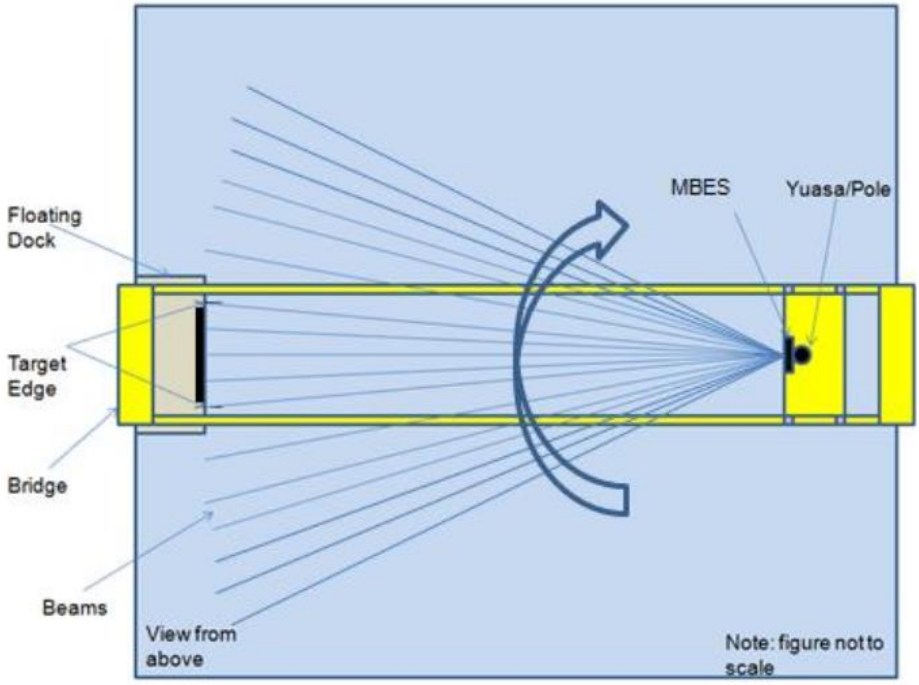

Figure 4.4: MBES calibration sweep concept. Yuasa is the mechanical rotator operating on the pole the MBES is attached to. From Heaton (2014).

4.3. Calibrating a MBES by separately measuring its transmission and reception

A MBES consists of a transmission and a reception array and, through the use of calibrated projectors and hydrophones, the transmit and receive beam patterns can be separated and characterized (Figure 4.5). Additionally, other characteristics of the transmission - pulse length, modulation and shading - can be measured (e.g., Trzcinska et al., 2021; Wendelboe, 2018).

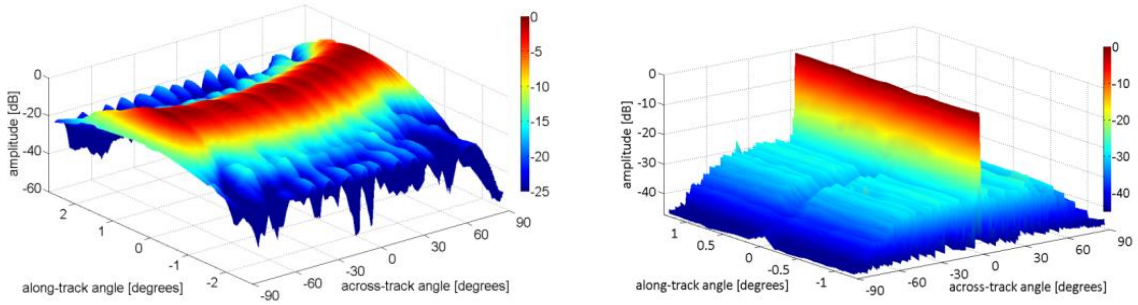

Figure 4.5: Reson 7125 beam patterns (single sector). Left: transmit beam pattern. Right: receive beam pattern for beam 128. From Lanzoni & Weber (2010).

Several studies applying this concept adopted an experimental design similar to the one depicted in Figure 4.1 (Foote et al., 2005), but replacing the reference target with a calibrated hydrophone or projector, to measure the transmit and receive beam patterns respectively (Lanzoni & Weber, 2010; Perrot et al., 2014; Wendelboe, 2018; Wendelboe et al., 2012). As with other laboratory tank methods, this approach is restricted to a controlled environment since it relies on the accurate positioning of the hydrophone/projector and on the usage of rotators to accurately orient the MBES arrays, suffering from the limitations already mentioned in Section 4.2.

4.4. Using a reference area for MBES calibration

An alternative to the previously described calibration techniques consists of comparing uncalibrated MBES S_b estimates from a natural seafloor against an independently acquired

absolutely referenced ARC from the same location. This approach bypasses the need for accessing controlled facilities with specific instrumentation or the inconvenience of moving a reference target over hundreds of beams, at sea.

4.4.1. Obtaining the reference

To get the calibrated seafloor reference, several users have taken advantage of the process described in Section 4.2 utilizing a calibrated SBES using a reference target. That reference sonar is then in turn pointed at the seafloor. Three examples of this approach are now presented.

Weber & Ward (2015) used a calibrated SBES – Simrad ES200-7CD - to obtain absolute estimates of S_b from a single grazing angle (45°). While restricted in grazing angle, this approach was particularly notable because a swept frequency system was used, allowing the collection of S_b between 170 and 250 kHz simultaneously, reflecting the variation in center frequency amongst sectors of modern MBES.

A different method was attempted by Eleftherakis et al. (2018), using two calibrated SBES transducers, Simrad ES200-7CD and ES333-7CD, operating at 200 and 333 kHz continuous wave pulses, respectively. While S_b was only estimated at two single frequencies, a mechanical rotator was used to sweep through a wide range of grazing angles (30-90°). The end goal was to use these data to calibrate a MBES operated at similar frequencies in the same location, an approach that will be further discussed in Section 4.4.

Guimarães (2020), combined the two aforementioned approaches by using four calibrated SBES transducers – Simrad ES70-7CD, ES120-7CD, ES200-7CD and ES333-7CD – all using swept frequency modulated pulses with overlapping frequency ranges and with the ability of being

mechanically rotated. Absolute estimates of S_b were collected between 45 and 400 kHz and at grazing angles spanning from 10 to 90°. This study will be further detailed in Chapter 5.

4.4.2. Establishing a suitable reference area

If such an approach is to be viable, establishing a reference area for this purpose should satisfy several criteria, as described by Roche et al. (2018). Ideally, its ARC should be stable and isotropic (no azimuthal dependence), with a negligible specular component, high mean backscatter strength and a gentle variation with grazing angle. To best meet those criteria, the seafloor should be near planar, with a homogeneous coarse sediment cover. Furthermore, the area must be deep and wide enough to operate the MBES in the far field and to accommodate a reasonable swath coverage. Besides ensuring the optimal acoustic environment, for practical logistical reasons, the area should also be easily accessible, safe to navigate on several headings (considering the size of the vessel where the MBES is mounted) and unperturbed by traffic or other activities that would potentially disturb the bottom, such as trawling or dredging (Eleftherakis et al., 2018). As for any other calibration procedure performed, the water column physical properties need to be measured to determine the attenuation coefficient profile. However, at sea, the ideal case would be for the reference area to be under a homogenous and temporally stable water mass, facilitating the estimation of the acoustical losses throughout the medium. If there is a seasonal variability in the oceanographic properties this might be of concern. To exemplify that complication, considering the interface between water (S = 30 PSU; T = 15°C) and fine sand, a water temperature drop of 5°C would affect the water-sediment impedance contrast, resulting in an S_b variation of about ~1 dB (based on the subsequent normal reflection coefficient change).

Naturally, a calibrated sonar should be used to provide S_b estimates over at least the same range of grazing angles acquired by the MBES to be calibrated and at the frequencies at which it operates. Ideally, if a reference area is to be used to calibrate a wide range of MBES, a broad band of frequencies should be observed (e.g., Guimarães, 2020). Also, if the reference area is to be used repeatedly, its temporal acoustic stability should be verified regularly (Roche et al., 2018), over short-, medium- and long-term time scales, as it can be affected by sediment mobilization, changes in the population of benthic fauna or even the release of gas bubbles from the seabed (J. T. Anderson et al., 2007). To monitor that temporal stability would require the repeated deployment of calibrated sonars.

4.4.3. Comparing the reference to the acquired MBES data

Eleftherakis et al. (2018), applied these principles to calibrate a KM EM2040D at 200 and 300 kHz. To simplify the experiment, the MBES was operated with just a single center sector, without yaw stabilization and in single swath mode. Two calibrated SBES (described in Section 4.2) were used to acquire the absolutely referenced S_b from the same location. The SBES were mounted on a mechanical rotator which allowed to control the tilt of the sonar, held constant during a survey line. To obtain observations at several grazing angles, the tilt varied between 0 and 60° in 3° steps (as the usable beamwidth of the reference system was slightly greater).

In principle, it is a trivial step to derive the calibration curve, for each frequency, by subtracting the ARC obtained with the SBES from the ARC obtained with the MBES (Figure 4.6).

In practice, deriving that ARC from the MBES, however, is fraught with complications. For the case of the Eleftherakis et al. (2018) work, this calibration was obtained using the simplifying assumption that the sonar beam pattern was fixed in a vertically referenced frame and

only varies across-track. Such a simplification, however, does not fully account for the variations that the combined transmit/receive beam pattern might suffer in a sonar reference frame rotating with respect to the vertical, coupled to the active steering process used in stabilization as described in Section 3.2. Furthermore, bearing in mind the heavy yaw stabilization usually used by the EM2040D depth modes, the approach did not address the along-track angular component described in Subsection 3.2.3. This is one of the main aspects particularly focused upon in this thesis.

Given the additional logistical complications of rotating the absolutely referenced S_b estimates, some other studies restricted the comparison to just a single grazing angle against the uncalibrated MBES S_b estimates (Ladroit et al., 2018; Weber et al., 2018). Such an approach assumes that an alternate means would be used to predict the shape of the calibration away from that one reference angle.

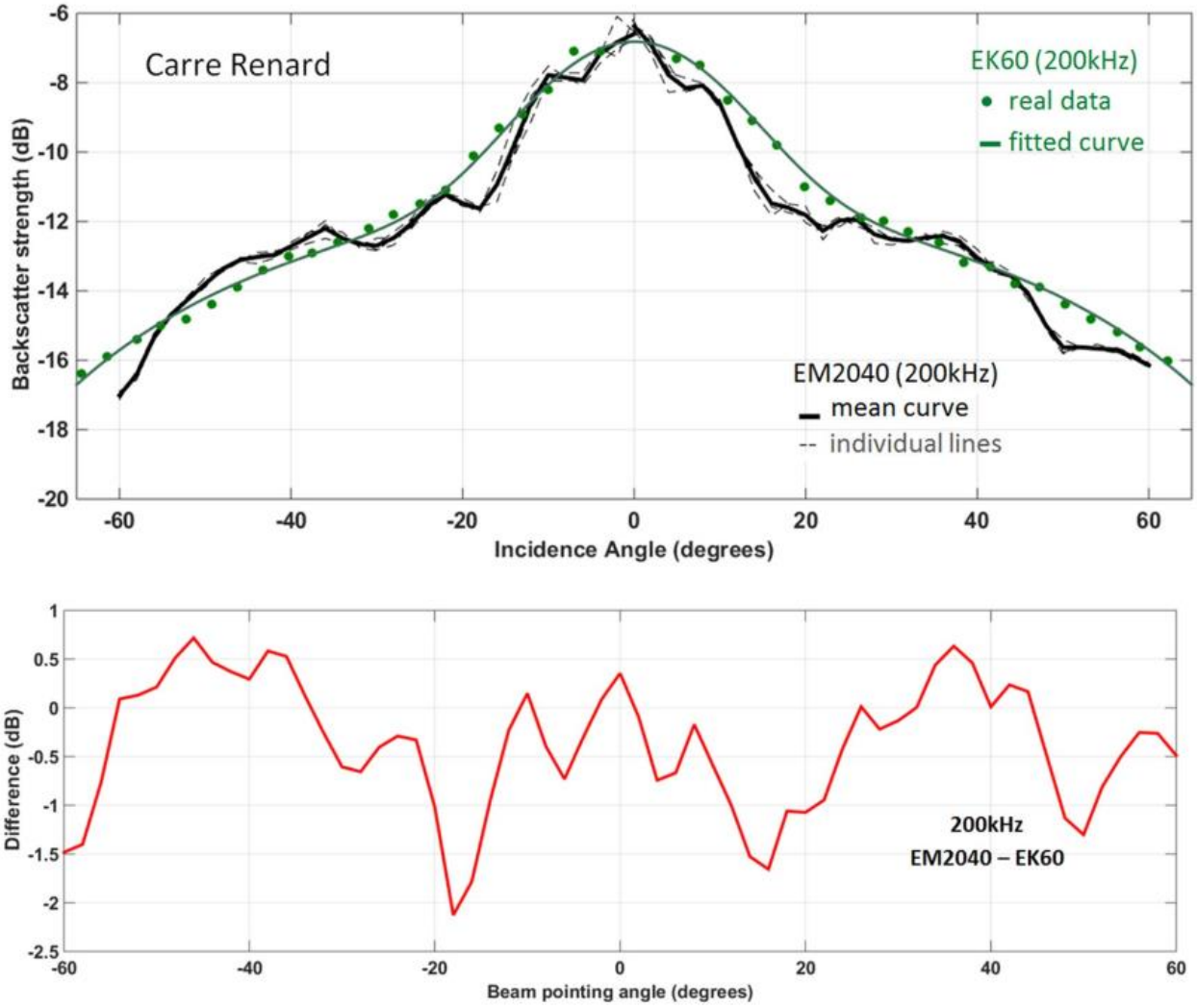

Figure 4.6: Obtaining a calibration curve for a MBES using data from a reference area obtained with a calibrated sonar. Top: Sb estimates from a calibrated SBES (green dots) and respective fit of a model (green solid line); mean ARC obtained with an EM2040D (black solid line) and ARCs obtained from individual lines (grey dashed lines). Bottom: Calibration curve obtained by subtracting the SBES ARC from the MBES ARC. From Eleftherakis et al. (2018).

5. PROPOSED BACKSCATTER STRENGTH CALIBRATION TECHNIQUE

This chapter describes the technique developed to correct the combined transmit/receive beam pattern of a multi-sector MBES, with the goal of enabling the extraction of absolutely referenced S_b estimates from it. The developed technique uses a reference area with an available absolutely referenced ARC. Hence, it can be classified as a cross-calibration technique between the sonar that delivered the absolutely referenced S_b and the uncalibrated MBES. Obviously, this research is, to a certain extent, inspired by the advances in Eleftherakis et al. (2018).

Additionally, the present research aims to further extend its reach by addressing variations of the beam pattern in the sonar referenced frame, the use of multiple transmit sectors, each with its own beam pattern center frequency, and the use of different pulse lengths on the same terrain. For that, the management of the underlying geometries partially implements the work of Hiroji (2016).

Despite the technique having the potential to be applied regardless of the MBES manufacturer/model, it was streamlined to ingest and process KM formats, .ALL and .KMALL.

5.1. Obtaining an absolutely referenced bottom backscatter strength dataset

The cornerstone of the developed technique is the absolutely referenced ARC from the reference area. Since each sector of a multi-sector MBES operates with a different center frequency, ARCs for those must be available, with a range of grazing angles as wide as possible. Considering a swath resulting from an angular coverage of ± 65° and that the seafloor of a

reference area is ideally flat, the ARC domain should at least be defined for grazing angles between 25 and 90°.

5.1.1. The reference S_b

While developing this calibration technique, the broadband ARCs obtained by Guimarães (2020) at several reference areas established in British Columbia, Canada were used since MBES data from the same locations was also collected in October 2019 under the scope of that research as well as subsequent acquisition in April 2022. The S_b values are organized in ARCs with a grazing angle resolution of 1°, at frequencies ranging roughly from 45 to 450 kHz in approximately 4 kHz steps.

Apart from the noise present in the multispectral ARCs, Guimarães (2020) acknowledges a few other limitations in his results, some described in the following subsubsections.

5.1.1.1. Grazing angle determination using the split beam transducers

To calculate the grazing angle of each bottom detection, this research takes advantage of the SBES capability to deliver across-track angles throughout the beam time-series. Applying some elementary trigonometry, a grazing angle can be associated to a specific phase ramp (Figure 5.1). Furthermore, assuming the limiting acoustic rays of the considered phase ramp follow identical paths, with identical refraction distortion, the determined grazing angle ends up accounting for that effect. The downside of this method is that only the across-track grazing angle is being addressed, while the along-track seafloor relief is ignored. This becomes a significant factor at high grazing angles.

Although the phase ramp method works well at oblique incidence, it is impractical to define it at near normal incidence geometries, thus invalidating the usage of this method. To address these situations, Guimarães (2020) assumed a flat seafloor at the minimum slant range and only accounted for the transducer's orientation with respect to a vertically referenced frame to determine the grazing angle, thereby neglecting the seafloor morphology and refraction effects. Nevertheless, considering that the reference areas deliberately chosen are almost flat, the beam path at near normal incidence geometries will most likely almost coincide with the vertical, greatly mitigating the impact of refraction effects. Notably, this allows an estimate of the along-track angle too, thus coping with the fact that the rotation axis of the transducer was often not exactly level.

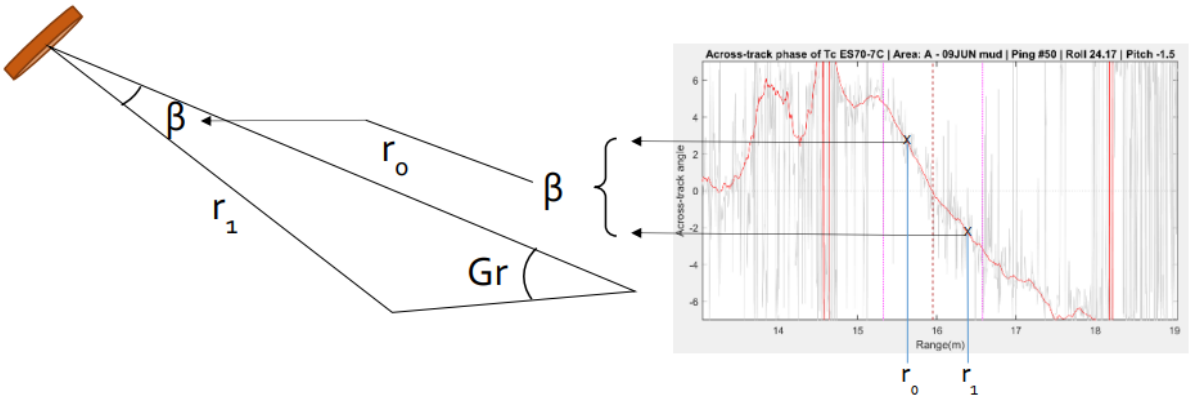

Figure 5.1: Geometric calculation of the grazing angle based on information from the across-track phase difference. From Guimarães (2020).

Another complication at near normal incidence, where the ensonified area is beamwidth limited, results from that ensonified area extending over several degrees (typically 5°, the two-way beamwidth of the used SBES), thus spanning through a wide range of grazing angles and, consequently, smearing the ARC at high grazing angles.

It is important to emphasize that any miscalculation in the grazing angle, besides the obvious effect in the ARC aspect, will affect the ensonified area calculation thus having a detrimental effect on the S_b reduction process.

5.1.1.2. Systematic ripple in the reference ARC frequency trend

Guimarães (2020) identified the average frequency trend, at different grazing angles, for the observed reference areas. Superimposed over that trend, however, was a rapid systematic S_b fluctuation, generally within ± 2dB (Figure 5.2). Furthermore, by removing the frequency trend at every grazing angle, a similar systematic ripple can be observed regardless of either grazing angle or sediment type (Figure 5.3) thus clearly indicating that this was a data reduction artifact and not the manifestation of a physical phenomenon. As the artifact is also present in the transducers' frequency dependent calibration curves, imperfect data processing during the calibration stage is deemed as the probable cause for this anomaly.

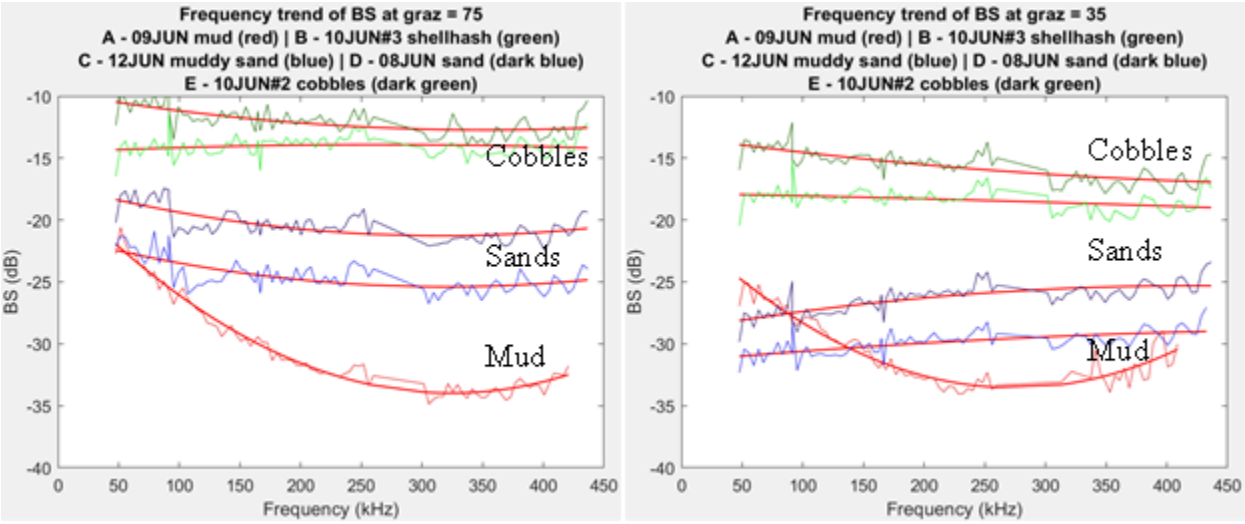

Figure 5.2: S_b frequency dependence for several reference areas (Cobbles: green hue; Sands: blue hue; Muds: red hue) at grazing angles of 75° (left) and 35° (right) with quadratic fitting curves (red) to better visualize the trend. From Guimarães (2020).

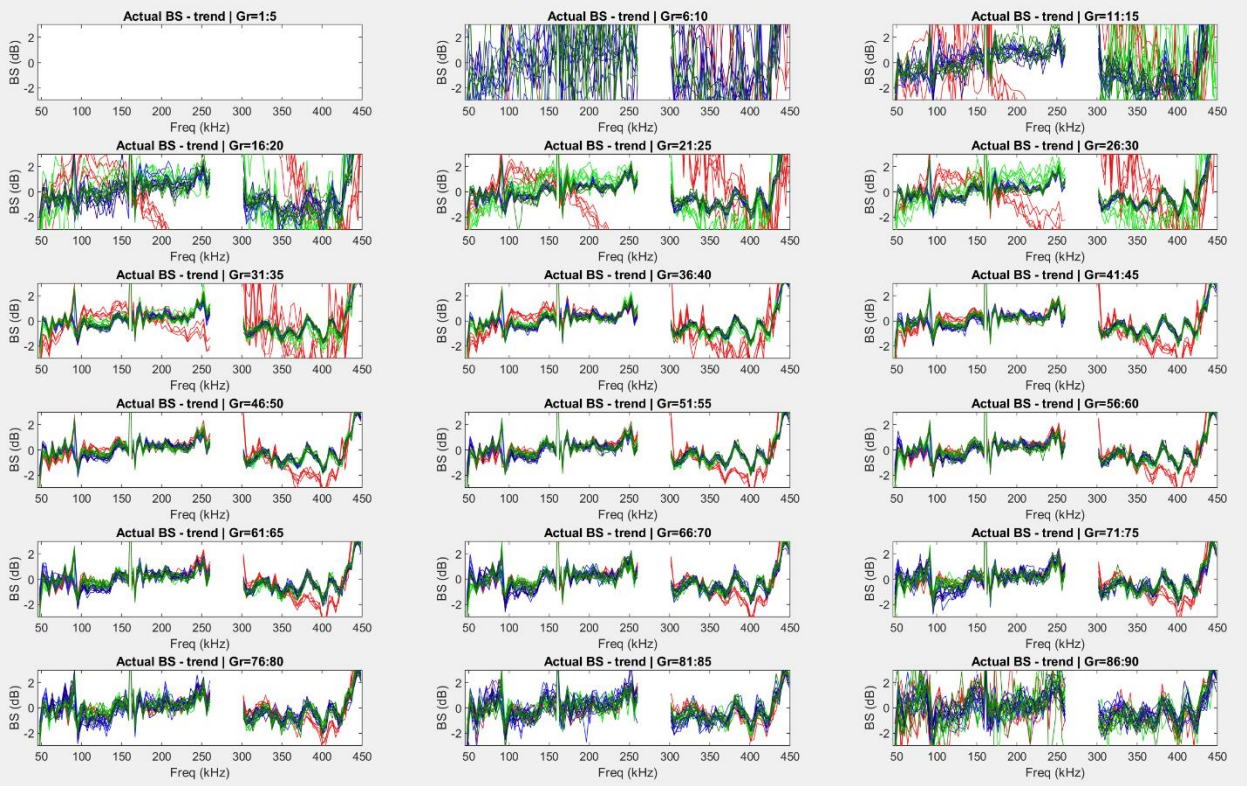

Figure 5.3: Difference between the estimated S_b frequency dependence and the associated quadratic fitting curve, presented at 5° grazing angle steps. Each color is associated to a different reference area: Cobbles: green hue; Sands: blue hue; Muds: red hue. From Guimarães (2020).

5.1.2. Extracting usable ARCs

To effectively extract a usable ARC for the center frequency of each sector of the MBES, the systematic ripple described in Subsubsection 5.1.1.2 and the noise in the data must be addressed.

5.1.2.1. Mitigating the effects of the systematic ripple in the reference ARC frequency trend

As explained in Subsubsection 5.1.1.2 and illustrated in Figure 5.3, a systematic ripple in frequency is superimposed on the multispectral ARC. The technique developed in this research

deals with that by identifying the average ripple at a certain grazing angle range and subsequently subtracting it from every S_b value.

Initially, a slice of the reference dataset containing the grazing angles between 40 and 50° is considered (Figure 5.4). This range was selected since it is not affected by the distinctive specular component of near normal incidence geometries and is commonly a less angle-variant region of the ARC.

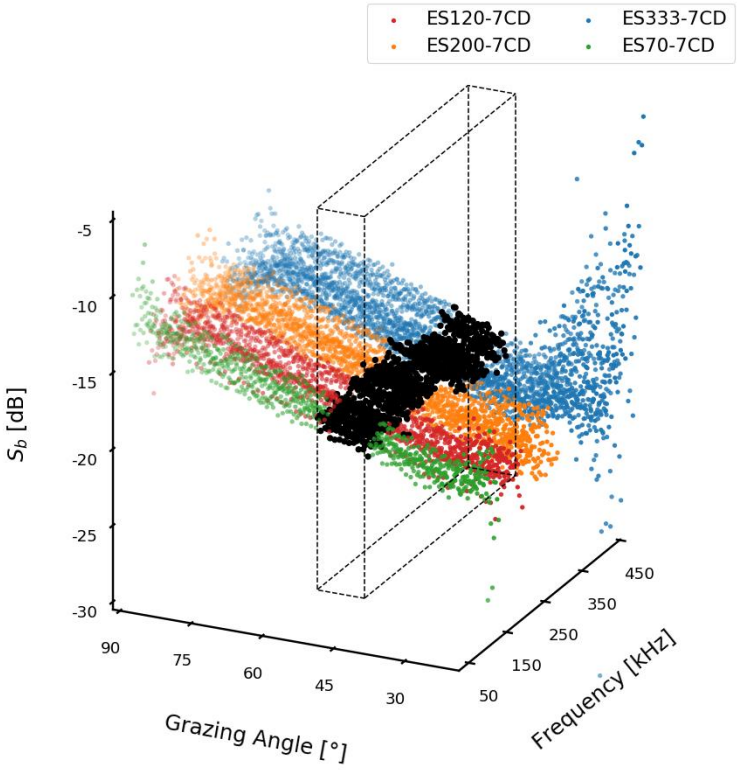

Figure 5.4: Slice of the multispectral ARC containing the grazing angles between 40 and 50°. The colors refer to data collected by different SBES transducers. Data from Guimarães (2020) – Shell hash reference area.

Secondly, the systematic ripple at every grazing angle (within the selected 40-50° range) is calculated by subtracting the S_b values from the respective frequency trend, determined by fitting a quadratic polynomial to the data through the method of least squares. This permits the estimation

of the average rapid S_b fluctuation as a function of frequency for the considered grazing angle range.

Finally, the average ripple, calculated with the grazing angles between 40 and 50°, is subtracted from the original multispectral ARC, mitigating the effects of the rapid systematic S_b fluctuation (Figure 5.5).

5.1.2.2. Fitting a Generic Seafloor Acoustic Backscatter model

As depicted in Figure 5.5 (bottom), the data still remains noisy (±~0.5 dB), especially at high grazing angles, and, if adjacent frequencies were to be considered, some discontinuities between ARCs would emerge. To deal with that, a Generic Seafloor Acoustic Backscatter (GSAB) model is applied to the data. The GSAB model was first introduced by Hellequin et al. (1997) and is commonly used to produce a continuous ARC (e.g., Eleftherakis et al., 2018; Fezzani & Berger, 2018; Hellequin et al., 2003) or to provide an empirical understanding of the angle dependent S_b variation (e.g., Fezzani & Berger, 2018; Lamarche et al., 2011). In reality, despite the fact that the GSAB model is not a physical model, when fitted to backscattering estimates, it returns empirical parameters that act as proxies of physical properties such as roughness and impedance contrast, enabling the clustering of different sediment types (Fezzani & Berger, 2018; Lamarche et al., 2011).

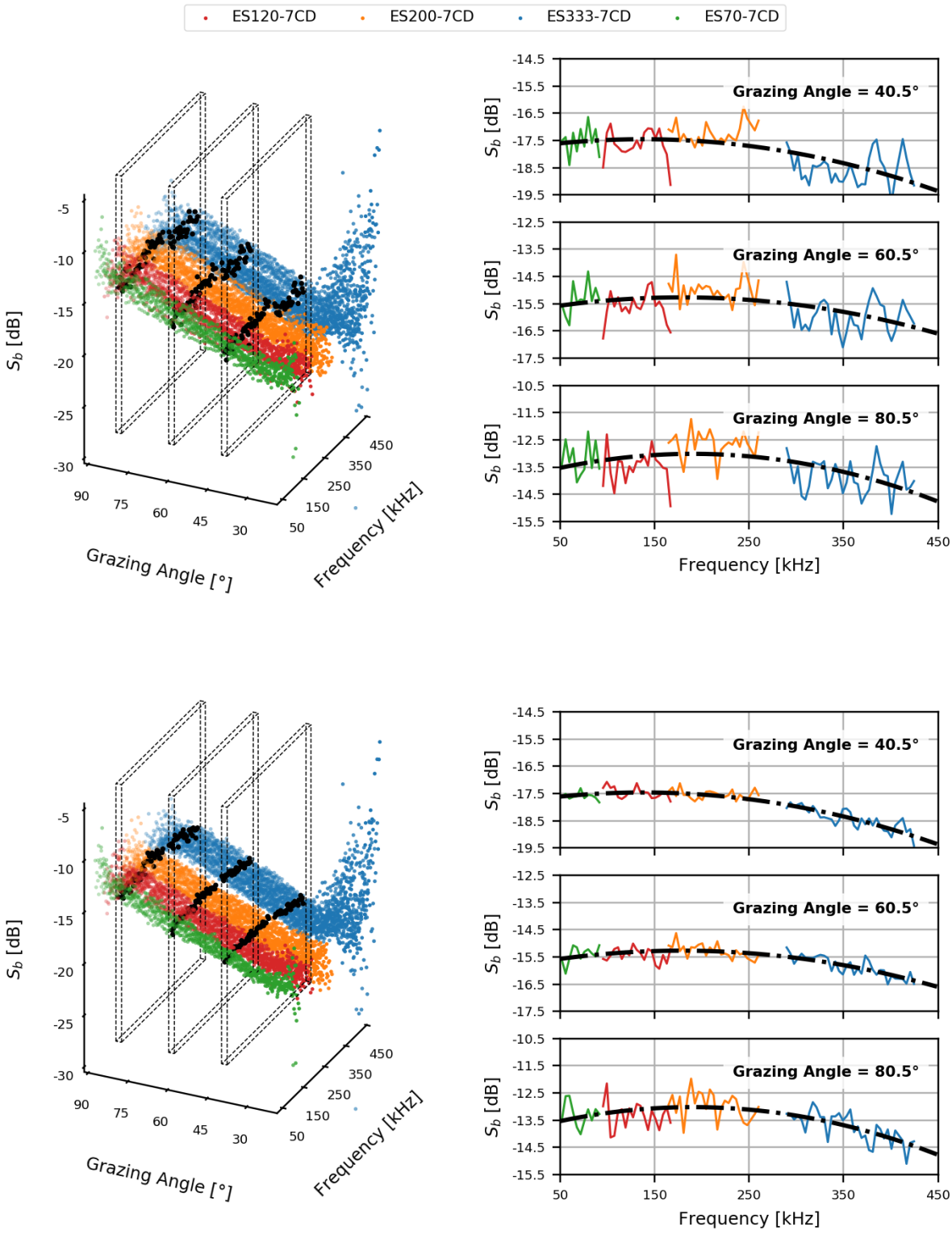

Figure 5.5: Mitigation of the systematic ripple in frequency. Top: original data; bottom: after the mitigation procedure. The colors refer to data collected by different SBES transducers. Data from Guimarães (2020) – Shell hash reference area.

The GSAB model represents the ARC with a Gaussian law for the specular component and a Lambert-like law for the remaining angular roll-off, as illustrated in Figure 5.6 and depicted in equation 5.1:

$$S_b^{GSAB}(\theta_i) = 10\log_{10}\left(A\exp\left(\frac{-\theta_i^2}{2B^2}\right) + C\cos^D\theta_i\right) \quad 5.1$$

where S_b^{GSAB} is the output of the model, A quantifies the specular maximum amplitude, B represents the angular extent of the specular regime, C embodies the average S_b level at oblique incidence, D controls the angular roll-off and θ_i is the incidence angle (Lamarche et al., 2011). While some other studies (e.g., Fezzani & Berger, 2018; Lamarche et al., 2011) introduce a second Lambert-like law to better account for the transition between the specular and Lambertian regimes (two extra parameters), this research uses the four parameter GSAB model presented in equation 5.1.

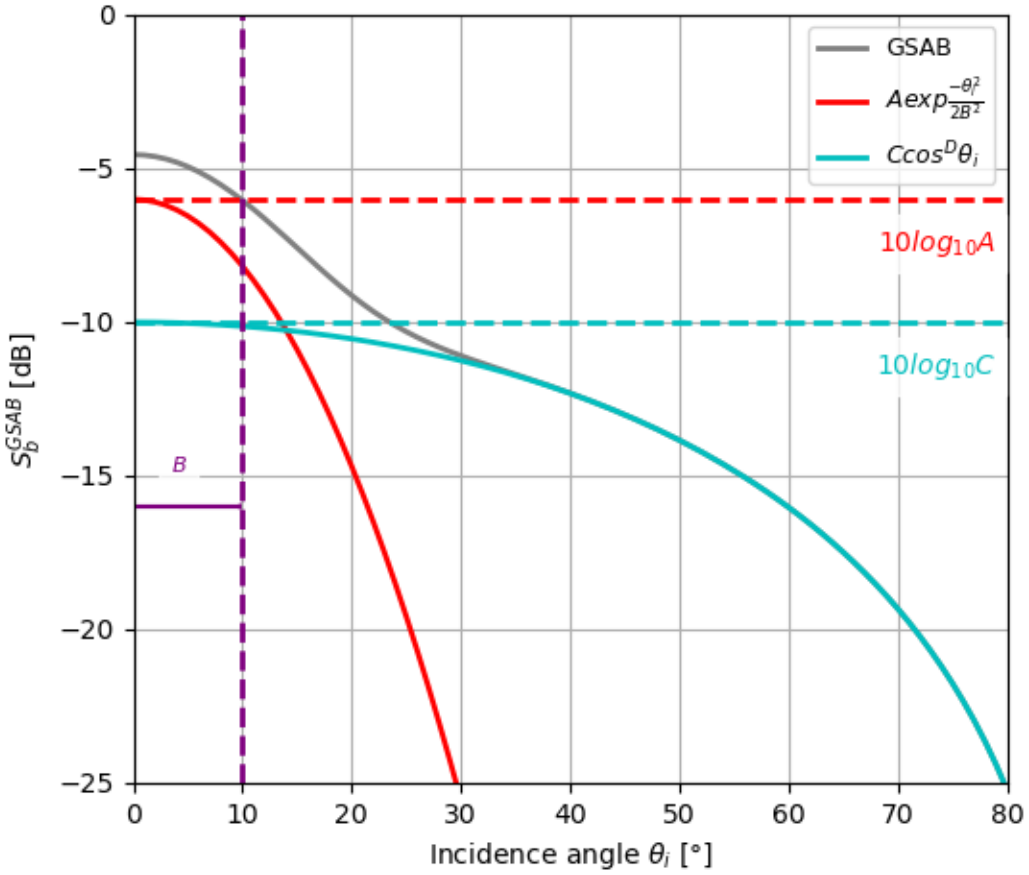

Figure 5.6: GSAB model components.

After processing the multispectral ARC as described in Subsubsection 5.1.1.2, the GSAB model is used to describe the S_b angular dependence at the center frequency of each sector of the MBES undergoing the calibration process. For each sector, a 10 kHz wide slice of the multispectral ARC, centered as close as possible to the sector's center frequency, is considered. Then, the GSAB model is fitted into that slice using the non-linear method of least squares. Since the original data might be especially noisy at near normal incidence and at low grazing angles, the range of angles used to fit the GSAB model is defined *ad hoc*, as shown in Figure 5.7.

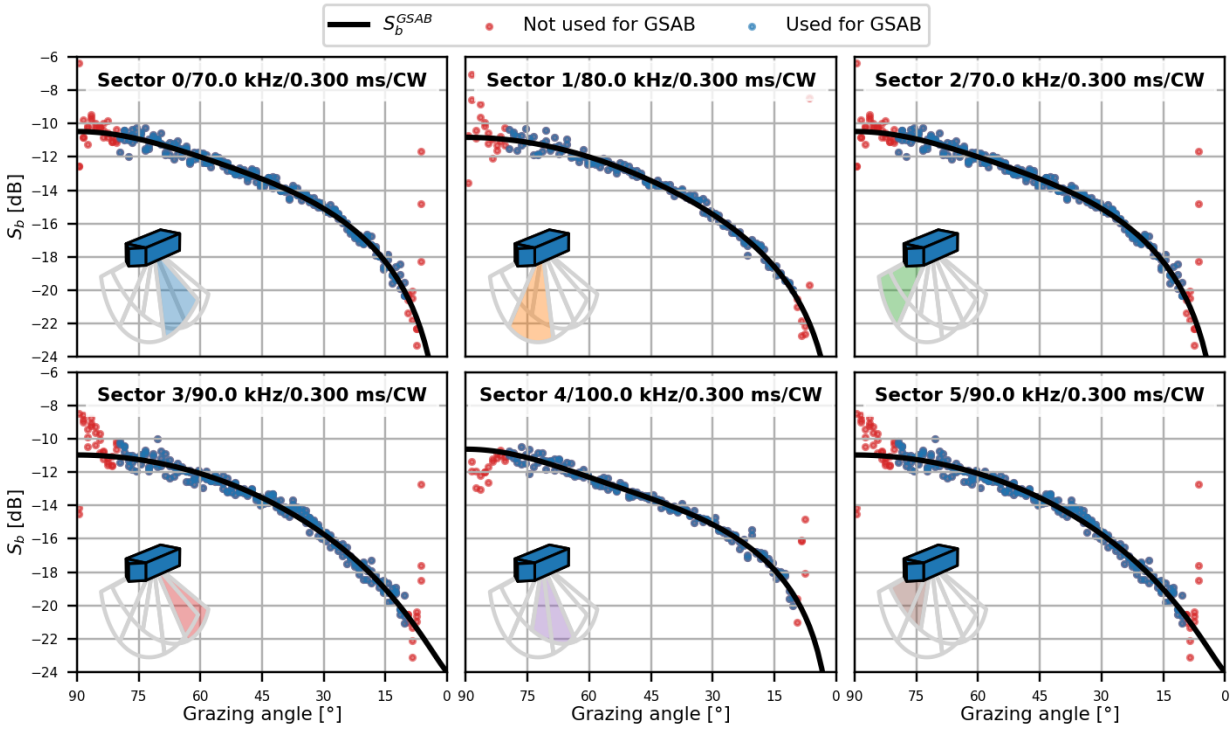

Figure 5.7: Reference ARCs obtained from the Cobbles reference area for the sector frequencies of an EM710 operating in Very Shallow / 70-100 kHz / Dual swath. Only observations with grazing angles within 10 and 80° were considered to generate the GSAB models, as outside that range the data was too noisy.

5.2. Dealing with the S_b estimates reported by KM MBES

To provide a uniform representation of the bottom backscatter strength across the swath, KM MBES standardly attempt to flatten the S_b angular dependence in the stored data, thereby highlighting the reflectivity contrasts between different bottom types (Hammerstad, 2000). This is achieved through a function known as Time Varying Gain (TVG), predicted before reception and applied in real time, the net result of which is to reduce the amount of dynamic range necessary to represent the outputted S_b estimates. Parameters describing their flattening algorithm are stored along with data so that, in principle, it can be removed.

The following subsections address how the S_b estimates are retrieved from MBES data, including the description of the TVG functions applied in the KM data formats, .ALL and .KMALL.

5.2.1. Details of the MBES data collection

The final goal of the MBES data collection is to compare its S_b estimates with the respective sector frequency independently-calibrated ARCs and to generate correction curves to obtain absolutely referenced S_b values. An additional complication, however, is that KM MBES, depending either on the user's decisions or on a look-up table indexed by depth, are capable of changing key parameters such as the number of transmit sectors, the number of swaths, the center frequency of each sector and the pulse length of each transmission. This is routinely done in order to maintain adequate signal to noise ratio over a wide range of depths. Each permutation of these parameters is designated as a mode, each with a different set of associated correction curves. As a result, data acquisition is performed with the objective of calibrating a MBES operating in a specific mode. That acquisition must then be repeated for each mode to be considered.

Furthermore, to confirm that the MBES data is free from azimuth dependence problems, survey lines are planned in a star-shaped pattern, enabling the comparison of the ARCs acquired with the vessel steaming in different azimuths. An additional benefit of running extra lines is that the repeatability can be tested, as operationally a single line can be compromised by steaming through a previous line's wash.

5.2.2. Averaging the S_b estimates

Every bottom detection is performed by analyzing the intensity timeseries of each beam. Rather than just associating a single intensity to a sounding, an envelope around the bottom detection instant (i.e., a patch of the ensonified area) is sampled many times, providing several bottom backscatter strength estimates, known as the snippets of a particular beam. Notably the length of these snippets corresponds to an angular subset of the receiver beamwidth that is small compared to the -3 dB beamwidth. Thus, all samples are considered valid without the need to compensate for the roll-off of the individual receiver beam, across-track sensitivity pattern. Although, the snippets are registered in the raw files, throughout this thesis a single bottom backscatter strength estimate is used to represent each beam (S_b^{all}). Equation 5.2 is used to convert each snippet (si_b^{all}) of a beam to linear units, perform an unweighted average, and convert it back to dB.

$$S_b^{all} = 10\ \log_{10}\left(\frac{1}{N}\sum_{n=1}^{N} 10^{si_b^{all}/10}\right) \qquad 5.2$$

This previously explained methodology is solely applied to data using the .ALL format. For the .KMALL format, the S_b value used to represent each beam is the *reflectivity1_dB* data field (S_b^{kmall}), since the available documentation unambiguously states that these are affected by the TVG (*TVG_dB* data field) also recorded in the datagrams (Kongsberg Maritime, 2021).

5.2.3. The TVG function in the .ALL format

The TVG function applied to S_b^{all} estimates in the .ALL format (TVG_{all}) is classically described by Hammerstad (2000), and has been addressed by several studies (Hiroji, 2016; Teng, 2011). It can be understood as the sum of the three terms that deal with the following processes: a

near normal incidence correction to remove the specular component ($NNIC_{all}$), a Lambertian correction to flatten the angular roll-off (LC_{all}) and an ensonified area correction (EAC_{all}):

$$TVG_{all} = NNIC_{all} + LC_{all} - EAC_{all} \quad 5.3$$

To retrieve unflattened S_b^{noTVG} values from the .ALL format, it is necessary to reconstruct TVG_{all}, subtract it from S_b^{all} and compute an improved estimate for the ensonified area (EAC_{imp}):

$$S_b^{noTVG} = S_b^{all} - TVG_{all} - EAC_{imp} \quad 5.4$$

Before addressing each component of the TVG_{all}, it is valuable to establish how the grazing angles are estimated. Since the morphology of the bottom is unknown, a planar seafloor assumption is made and no along-track slope is assumed. Concurrently, normal incidence is attributed to the minimum slant range, allowing conversion of two-way travel times into grazing angles (θ_g^{all}) throughout the swath, as depicted in Figure 5.8 and defined as

$$\theta_g^{all} = \arcsin\left(\frac{R_0}{R}\right) \quad 5.5$$

where R_0 is the minimum slant range and R is the range of a particular bottom detection.

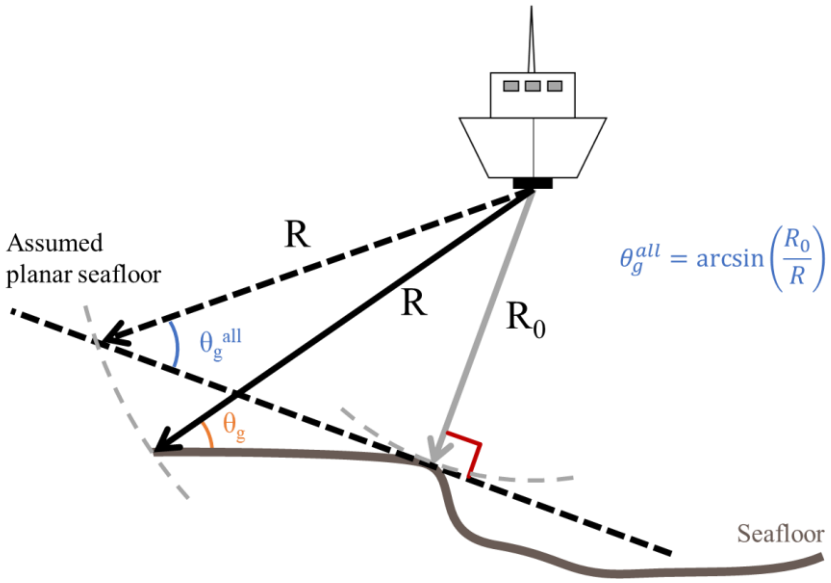

Figure 5.8: KM TVG planar seafloor assumption and subsequent grazing angle estimation.

5.2.3.1. The Near Normal Incidence Correction (.ALL)

The $NNIC_{all}$ assumes that the bottom backscatter strength varies linearly with grazing angle and is defined by equation 5.6, where BS_N and BS_O are, respectively, the S_b values at normal incidence and at a predefined oblique angle known as the crossover angle (CA). While R is the outcome of converting the two-way travel time of the bottom detection to a slant range, BS_N, BS_O, CA is user selected and R_0 is estimated based on the previously acquired swaths, both being recorded in the .ALL files.

$$NNIC_{all} = \begin{cases} BS_O - BS_N, & R \leq R_0 \\ (BS_O - BS_N)\left(1 - \sqrt{\dfrac{R - R_0}{R_0 \sec(CA) - R_0}}\right), & R_0 \geq R \geq R_0 \sec(CA) \\ 0, & R \geq R_0 \sec(CA) \end{cases} \quad 5.6$$

The applied $NNIC_{all}$ model is used to flatten the specular peak of the ARC. To that end, it operates under the assumption that the S_b values, between normal incidence and the 90°-CA, vary linearly with grazing angle, as depicted in Figure 5.9.

5.2.3.2. The Lambertian Correction (.ALL)

The applied TVG_{all} model assumes that the ARC will have a Lambertian law superimposed on it. To remove that component of the angular dependence, LC_{all}, defined by equation 5.7, is used.

$$LC_{all} = \begin{cases} 0, & R \leq R_0 \\ 20 \log_{10}\left(\dfrac{R_0}{R}\right), & R \geq R_0 \end{cases} \quad 5.7$$

The process is illustrated in Figure 5.9.

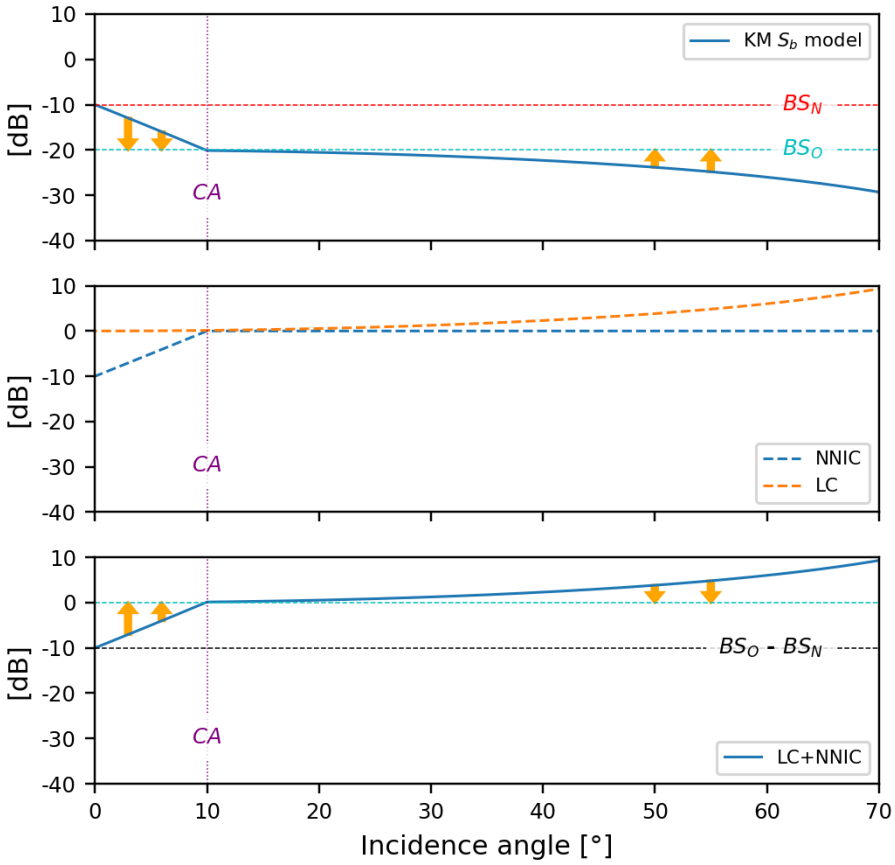

Figure 5.9: KM S_b model (top) and plotting of the LC and NNIC TVG components, both individually (center) and added together (bottom). Note the orange arrows, illustrating the flattening of the S_b angular dependence by applying LC + NNIC.

5.2.3.3. The Ensonified Area Correction (.ALL)

As previously mentioned in Section 2.2, the ensonified area is a function of the grazing angle, pulse length and transmit and receive beamwidths. According to Hammerstad (2000), the ensonified area used to estimate S_b^{all} in real-time is defined by equations 5.8 – 5.10.

$$A_{bl}^{TVG} = \Omega^{rx}\Omega^{tx}R^2 \qquad 5.8$$

$$A_{pl}^{TVG} = \frac{\mathrm{c}\,\tau\,\Omega^{tx} R}{2\sqrt{1-\left(\frac{R_0}{R}\right)^2}} \tag{5.9}$$

$$EAC_{all} = \begin{cases} 10\log_{10}(A_{bl}^{TVG}) \ , & R \leq R_0 \\ 10\log_{10}\left(A_{pl}^{TVG}\right), & R > R_0 \end{cases} \tag{5.10}$$

This model highly favors the usage of a pulse limited ensonified area, which might not be the best representation of the underlying acoustic process. At some point, some studies (Eleftherakis et al., 2018; Hiroji, 2016; Weber et al., 2018) started recreating the EAC_{all} by considering the smallest between the beamwidth and pulse limited ensonified areas:

$$EAC_{all} = 10\log_{10}\min\left(A_{pl}^{TVG}, A_{bl}^{TVG}\right) \tag{5.11}$$

Throughout this research, equation 5.11 will be used to reconstruct EAC_{all}. Unfortunately, although it is apparent that this model is now used in the KM TVG for .ALL format, it is not clear when exactly KM first implemented this model.

Regrettably, some ambiguities emerge when reconstructing EAC_{all}. The existing documentation (Hammerstad, 2000; Kongsberg Maritime, 2018a) does not specify if the used receive and transmit beamwidths (Ω^{rx} and Ω^{tx}) account for steering and frequency changes. Furthermore, KM MBES transmissions are typically tapered with a Hanning window and it is not indicated if the used τ is either the total or the effective pulse length. Throughout this work, it is assumed that EAC_{all} is computed by using the total pulse length (τ_t) and nominal beamwidths that do not account either for beam steering or for frequency changes (Ω_{nom}^{rx} and Ω_{nom}^{tx}). Note that the only data in the .ALL format used in this thesis comes from an EM710.

Even assuming, however, that adequate pulse length and beamwidths were being used, the applied grazing angles are still calculated assuming a planar seafloor (θ_g^{all} defined in equation 5.5).

Moreover, the morphology of the bottom in the along-track direction (perpendicular to the swath) is not considered at all. Thus, clearly, a better estimate of the grazing angle is needed.

In view of the above, EAC_{all} should be removed and replaced by an improved ensonified area estimate (EAC_{imp}), capable of accounting for the two-dimensional bottom morphology and calculated using the correct beamwidths and pulse lengths, ultimately contributing to a better S_b^{noTVG} computation.

5.2.4. The TVG function in the .KMALL format

The TVG applied in the .KMALL format (TVG_{kmall}) serves the main purpose of the already described TVG_{all}. While very similar to the TVG_{all}, the TVG_{kmall} has some noteworthy particularities. Arguably, the main difference is that the applied TVG_{kmall} is stored in the .KMALL files, removing the need to reconstruct it (Kongsberg Maritime, 2021). Its structure is identified in equation 5.12, where 2TL is as defined by equation 2.6.

$$TVG_{kmall} = NNIC_{kmall} + LC_{kmall} - EAC_{kmall} + 2TL \quad (5.12)$$

Obtaining S_b^{noTVG} values requires subtracting TVG_{kmall} from the flattened estimates (S_b^{kmall}), but now a compensation for both the ensonified area and the transmission loss must be provided (equation 5.13).

$$S_b^{noTVG} = S_b^{kmall} - TVG_{kmall} - EAC_{imp} + 2TL \quad (5.13)$$

Computing 2TL involves the calculation of both the spherical spreading, purely geometric, and the attenuation, dependent on the slant range and on the attenuation coefficient throughout the water column. The acquisition software used with KM MBES, the Seafloor Information System (SIS), allows the user to specify both the sound speed profile and the local salinity, enabling the computation of the attenuation coefficient α as a function of the acoustic frequency of the

transmission. Since α is stored for every beam, 2TL can be easily reconstructed and applied as depicted in equation 2.7.

Both the Lambertian and Near Normal Incidence corrections are functionally identical in .ALL and in .KMALL. Nevertheless, there are some minor differences. In the .KMALL format, the R_0 parameter is no longer stored in the raw data. In principle, it is not needed as TVG_{kmall} is supplied. In practice, for some early versions of the .KMALL format, it was calculated incorrectly. According to K. Nilsen (personal communication, March 3, 2022), despite the data having the correct TVG applied, the stored TVG_{kmall} value was computed considering $NNIC_{kmall}$ with the wrong sign. Actually, this issue was identified in EM2040P data (.KMALL Rev. F). In order to confirm whether the stored TVG corresponds to the described model, an educated guess for the R_0 value was used throughout this work: R_0 was estimated through the minimum slant range of the swath under investigation. This is highly likely as KM no longer actually applies the TVG as a real time gain. Rather, they apparently log data in 24bit resolution and apply it after the fact.

5.2.4.1. The Ensonified Area Correction (.KMALL)

There are significant differences between the .KMALL version of the ensonified area correction and its .ALL counterpart. The fact that the TVG_{kmall} is stored in the raw files enables other users, through trial and error, to understand what assumptions were made in its computation

The pulse tapering is accounted for by the usage of the effective pulse length (recorded in the .KMALL) and both transmit and receive beamwidths account for the sector frequency.

Regarding the beam steering effects, these are only considered to compensate the receive beamwidth. Even if the transmit beamwidth remains uncorrected for this effect, the reality is that

the steering on transmission, even for a multi-sector yaw-stabilized MBES, is usually much smaller than on reception, well within ±10°, resulting on an almost insignificant widening of the beam.

The nominal beamwidths stored in .KMALL and .ALL (Ω_{nom}) refer to an unsteered beam and assume the MBES is operating at a nominal frequency (f_{nom}), e.g., 100 kHz for the KM EM712 and 300 kHz for the KM EM2040P (K. Nilsen, personal communication, March 18, 2022). Equation 5.14 defines how to compensate the Ω_{nom} for a frequency shift and beam steering (Ω_{3dB}), where f is the actual transmission frequency and θ_s is the receive steering angle.

$$\Omega_{3dB} = \Omega_{nom} \times \frac{f_{nom}}{f} \times \frac{1}{\cos\theta_s} \tag{5.14}$$

Another significant change consists of the transition between pulse and beamwidth limited ensonified areas. According to K. Nilsen (personal communication, April 26, 2022), the .KMALL format uses the model expressed in equation 5.15 instead of equation 5.11.

$$EAC_{kmall} = 5\log_{10}\left(\frac{1}{(A_{bl}^{TVG})^{-2} + (A_{pl}^{TVG})^{-2}}\right) \tag{5.15}$$

Figure 5.10 compares the ensonified area corrections obtained with equations 5.11 (.ALL) and 5.15 (.KMALL). As expected, when using the EAC_{kmall}, a much smoother transition between the pulse and beamwidth limited regimes is observed, avoiding the step seen with EAC_{all}. The correction difference at the pulse to beam limited transition is ~1.5 dB.

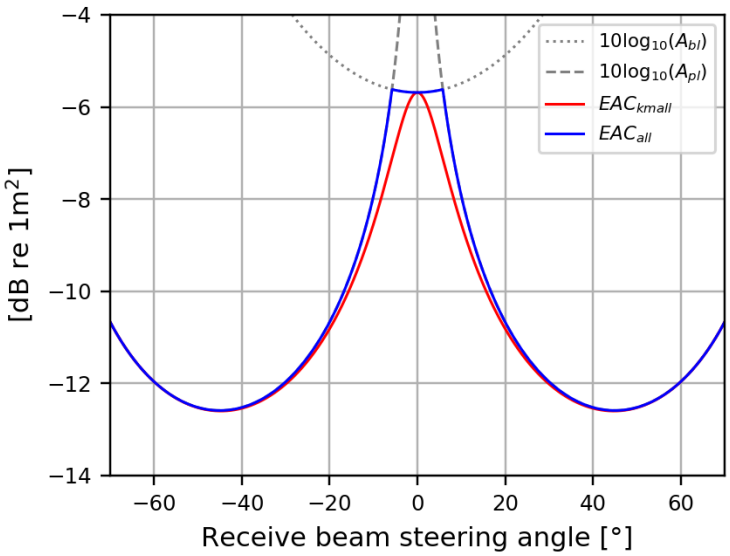

Figure 5.10: Comparison between EAC_{kmall} and EAC_{all}. Pulse length: 1ms; transmit/receive beamwidths: 1°/ 2°; depth = 20m; sound speed = 1500 m/s; flat seafloor.

While EAC_{kmall} might be an improvement, to compute the grazing angles, a flat bottom assumption is still used. Therefore, to obtain optimal S_b^{noTVG} values, it is still desirable to replace EAC_{kmall} with a more refined estimate for the ensonified area.

5.3. Estimating the acoustic seafloor grazing angle

For every retrieved $S_b^{all/kmall}$ estimate, it is necessary to estimate the respective grazing angle, required to link the MBES data to the reference ARC and to refine the ensonified area correction estimate.

Estimating the grazing angle will rely on two main steps: defining the vector at which the beam intersects the bottom and modelling the seafloor relief.

5.3.1. Estimating the beam vector at the bottom

KM MBESs provides all the necessary metadata – lever arms, vessel instantaneous orientation and sonar mounting angles – to position a bottom detection with respect to the sonar, in a local vertically referenced frame – the SCS. Moreover, beamforming and raytracing considerations such as non-concentric cone intersection and refraction due to the sound speed profile are accounted for in the real-time along and across-track positioning of each bottom detection.

To estimate the beam direction at the bottom, a three-dimensional vector is established in the SCS, between the transmit array at the time of transmission and the bottom detection. The limitation of this approach is that the refraction effects are not fully incorporated into the obtained vector, as illustrated in Figure 5.11.

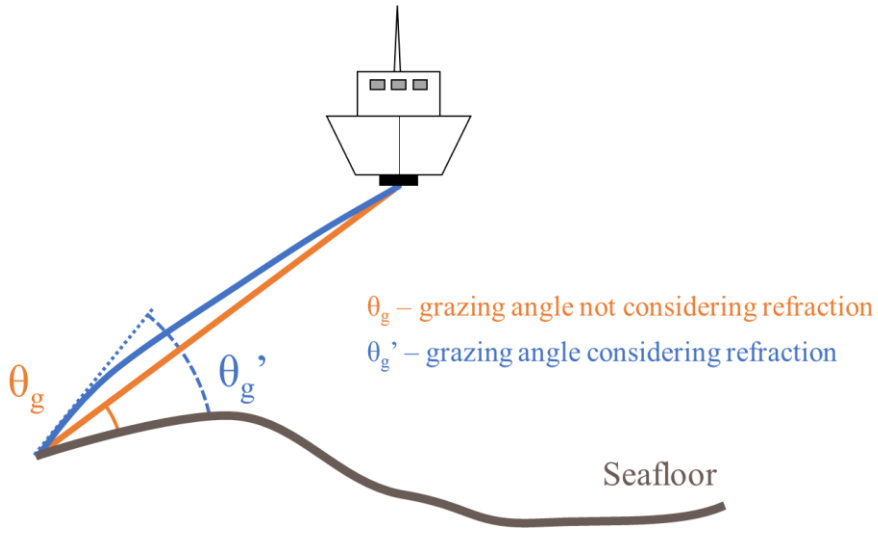

Figure 5.11: Effect of refraction on determining the beam direction at the bottom and consequences for the subsequent grazing angle estimation.

5.3.2. Estimating the bottom relief

The estimation of the bottom morphology around the beam strike location relies on using a digital terrain model (DTM), generated with the soundings collected by the MBES undergoing calibration.

First, every depth is shifted to common vertical reference through tide reduction and the soundings' horizontal coordinates are transformed into a GCS – in this case, a UTM coordinate system. Secondly, a rectangular grid is superimposed over the area of interest, and each sounding is binned into the cell it falls under. The grid resolution is defined ad hoc. Finally, each cell outputs a single depth value (Z_{cell}), obtained through the weighted averaging described in equation 5.16,

$$Z_{cell} = \frac{1}{N}\sum_{i=1}^{N} Zi \ \cos^2 \theta i_s^{ac} \qquad 5.16$$

where N is total the number of soundings binned into that cell, and Zi and θi_s^{ac} are the depth and the across-track steering angle associated to sounding i. Figure 5.12 shows how different steering angles influence the weight of each sounding in the generation of a cell's depth estimate, illustrating how the weighting decreases as θi_s^{ac} grows. The geometric centers of each cell are the nodes of the DTM.

The result is a bathymetry DTM that enables the computation of the grazing angle associated to each bottom detection. Figure 5.13 illustrates the bathymetry and the associated bottom relief for a single survey line, revealing the potential impact of the bottom detection noise on the computation of the across- and along-track slopes. Nonetheless, as several lines are typically used to generate the DTM, the resulting slope noise is mitigated.

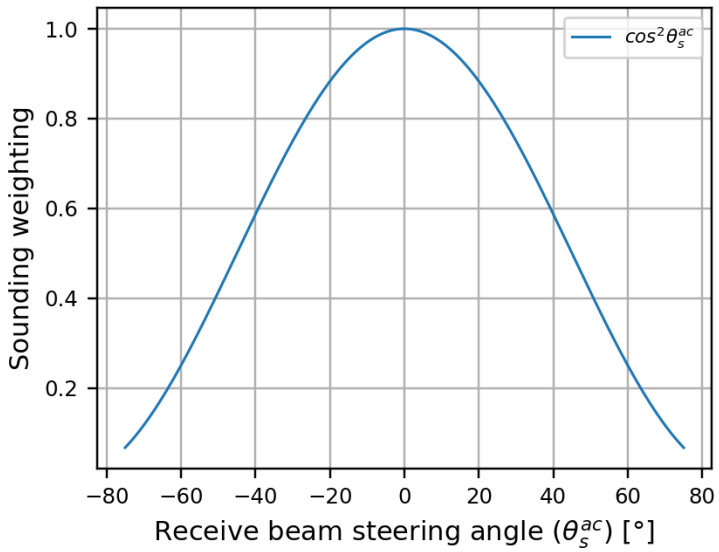

Figure 5.12: Weighting of each sounding as a function of the across-track steering angle.

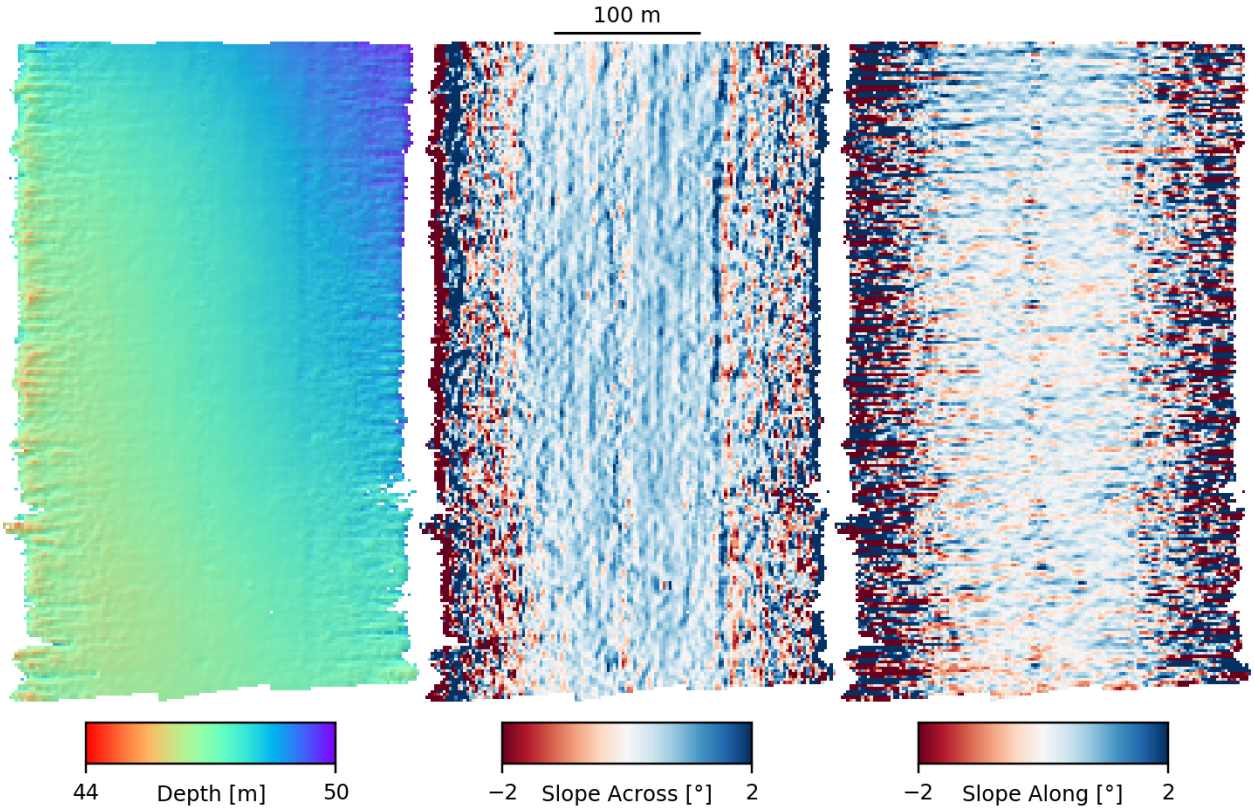

Figure 5.13: DTMs generated with data from a single survey line (2m resolution). Left: Depth; Center: Across-track bottom slope; Left: Along-track bottom slope. Data from an EM710 operating in Very Shallow / 70-100 kHz / Dual swath.

5.3.3. The grazing angle computation

With the beam vector and the DTM defined, the next step is to retrieve the grazing angle associated to each bottom detection. To that end, the node of the DTM closest to a sounding is identified. Then, through least squares regression, a plane is fitted on that node and its adjacent eight neighbors. Subsequently, a vector orthogonal to the plane is defined and described in the SCS. Then, by calculating the complement of the angle between the beam vector ($\vec{b}$) and the seabed plane's orthogonal vector ($\vec{n}$), the three dimensional (θ_g^{3D}), across- (θ_g^{ac}) and along-track (θ_g^{al}) grazing angles are determined (equations 5.21-5.23). A similar approach is used by Hiroji (2016).

$$\overrightarrow{b_{y0z}} = \vec{b} - (\vec{b} \cdot (1,0,0))(1,0,0) \quad 5.17$$

$$\overrightarrow{n_{y0z}} = \vec{n} - (\vec{n} \cdot (1,0,0))(1,0,0) \quad 5.18$$

$$\overrightarrow{b_{x0z}} = \vec{b} - (\vec{b} \cdot (0,1,0))(0,1,0) \quad 5.19$$

$$\overrightarrow{n_{x0z}} = \vec{n} - (\vec{n} \cdot (0,1,0))(0,1,0) \quad 5.20$$

$$\theta_g^{3D} = \arcsin \frac{\left|\vec{b} \cdot \vec{n}\right|}{\left\|\vec{b}\right\| \times \|\vec{n}\|} \quad 5.21$$

$$\theta_g^{ac} = \arcsin \frac{\left|\overrightarrow{b_{y0z}} \cdot \overrightarrow{n_{y0z}}\right|}{\left\|\overrightarrow{b_{y0z}}\right\| \times \left\|\overrightarrow{n_{y0z}}\right\|} \quad 5.22$$

$$\theta_g^{al} = \arcsin \frac{\left|\overrightarrow{b_{x0z}} \cdot \overrightarrow{n_{x0z}}\right|}{\left\|\overrightarrow{b_{x0z}}\right\| \times \left\|\overrightarrow{n_{x0z}}\right\|} \quad 5.23$$

5.4. Refining the ensonified area estimate

To provide better estimates for the ensonified area, equations 2.4 and 2.5 are used to model the beamwidth and pulse limited regimes, incorporating the calculated along- and across-track grazing angles in the calculation.

Since the pulses are tapered, the effective pulse length (τ_{eff}) is used to compute A_{pl}. Unlike the .KMALL format, the .ALL format does not register the τ_{eff}. In that case, and assuming a tapering using a 100% Hanning window, τ_{eff} is calculated through

$$\tau_{eff} = \tau_t \times 0.375 \tag{5.24}$$

where τ_t is the pulse length of the tapered pulse and 0.375 is the ratio between the mean square amplitude of the rectangular window and the mean square amplitude of the used window (Ladroit et al., 2018).

Regarding the transmit and receive beamwidths, the -3dB beamwidths are used instead of the equivalent beamwidths. The -3dB beamwidths are derived from Ω_{nom} by applying equation 5.14 to account for the effects of beam steering and shifts from the nominal frequency.

Finally, the transition between A_{pl} and A_{bl} is done in a similar fashion to the one in EAC_{kmall}, resulting in the improved ensonified area (EAC_{imp}) defined by equation 5.25.

$$EAC_{imp} = 5\log_{10}\left(\frac{1}{(A_{bl})^{-2} + \left(A_{pl}\right)^{-2}}\right) \tag{5.25}$$

5.5. Estimating the sonar referenced angles

As already discussed in Chapter 3, the transmit and receive beam patterns will respectively vary the most in the across- and along-track directions. In reality, while the receiver sensitivity across-track is relatively flat near the center, for angles beyond 60°, it starts to roll-off steeply and

can become more of a factor than the transmit across-track pattern. Therefore, to describe the variability of the combined beam pattern in a sonar referenced frame, every S_b^{noTVG} estimate is mapped in a feature space where the coordinates are the across-track sonar referenced angle at transmission (SRAT) and the along-track sonar referenced angle at reception (SRAR). The following two subsections describe how these geometric constructs, originally proposed by Hiroji (2016), are implemented in the present thesis.

5.5.1. Calculating SRAT

In essence, the SRAT is the angle between a vector orthogonal to the transmit transducer's face and the across-track component of the beam vector at the time of transmission represented in the ACS_{tx} (ACS centered in the transmit array at the time of the transmission) ($\overrightarrow{b_{tx}^{ACS}}$). A proxy of $\overrightarrow{b_{tx}^{ACS}}$ can be estimated by considering the registered beam steering angle at reception (θ_s^{ac}) with respect to the receive array, allowing representation of the beam vector in the ACS_{rx} (ACS centered in the receive array at the time of the reception):

$$\overrightarrow{b_{rx}^{ACS}} = \begin{bmatrix} 0 \\ -\sin\theta_s^{ac} \\ \cos\theta_s^{ac} \end{bmatrix} \tag{5.26}$$

Furthermore, the instantaneous attitude of the vessel at transmission and reception must be considered, as well as the distinct mounting orientations of the receive and transmit array. So, $\overrightarrow{b_{tx}^{ACS}}$ is estimated through the following equations,

$$R(\kappa,\psi,\omega) = \begin{bmatrix} c_\kappa c_\psi & c_\kappa s_\psi s_\omega - s_\kappa c_\omega & c_\kappa s_\psi c_\omega + s_\kappa s_\omega \\ s_\kappa c_\psi & s_\kappa s_\psi s_\omega + c_\psi c_\omega & s_\kappa s_\psi c_\omega - c_\kappa s_\omega \\ -s_\psi & c_\psi s_\omega & c_\psi c_\omega \end{bmatrix}, \tag{5.27}$$

$$where\ c_\kappa = \cos\kappa\,;\ s_\kappa = \sin\kappa\,;\ etc..$$

$$\overrightarrow{b_{tx}^{ACS}} = \begin{bmatrix} x_{b_{tx}} \\ y_{b_{tx}} \\ z_{b_{tx}} \end{bmatrix} = R_{ma,tr}^{T} R_{t,tx}^{T} R_{t,rx} R_{ma,rc} \overrightarrow{b_{rx}^{ACS}} \quad 5.28$$

$$SRAT = \arctan\left(-\frac{y_{b_{tx}}}{z_{b_{tx}}}\right) \quad 5.29$$

where $R_{t,tx}$, $R_{t,rx}$, $R_{ma,tr}$, $R_{ma,rc}$ are the rotation matrices that respectively take in the following (heading, pitch, roll) triplets: vessel attitude at time of transmission and reception (subscripts t,tx and t,rx) and mounting angles of the transmit and receive transducers (subscripts ma,tr and ma,rc). Then, SRAT can be understood as the angle between the projection of $\overrightarrow{b_{tx}^{ACS}}$ in the y0z plane ($\overrightarrow{b_{tx,y0z}^{ACS}}$) and the z-axis of ACS_{tx}, easily obtained through equation 5.29. The geometry associated to the SRAT computation is represented in Figure 5.14 (left).

While this approach is not affected by refraction problems, it simplifies the shift from the receive to the transmit transducer to a strictly angular problem, solvable by a sequence of rotations. Hence, the impacts on the SRAT estimation due to the transducers not sharing the same coordinates in the VCS (especially in the across-track axis) are avoided.

5.5.2. Calculating SRAR

The SRAR is the angle between the beam vector at the time of reception ($\overrightarrow{b_{rx}^{ACS}}$) and the projection of that same vector in the y0z plane ($\overrightarrow{b_{rx,y0z}^{ACS}}$) (Figure 5.14 right), both defined in the ACS_{rx}. Despite the along-track transmit steering angle of each sector being registered, it is not enough information to construct a proxy of $\overrightarrow{b_{rx}^{ACS}}$. When the transmit beam is steered, it assumes a conical surface, resulting in an ensonified area of the seafloor with a complex shape. On top of that, the same effect occurs with the receive beams, where, for the outer beams, much heavier steering is used, resulting in an even more intricate geometry. The net result is that the angle of the

beam vector relative to the receiver along-track pattern cannot be simply approximated by the single along-track transmit steering angle per sector.

An alternative approach, used herein, consists of representing the beam vector at reception in the SCS ($\overrightarrow{b_{rx}^{SCS}}$), established between the receive array at the time of reception and the sounding, analogously to what was performed in Subsection 5.3.1 to estimate the grazing angles. Likewise, this method does not account for refraction effects. The beam vector at reception must be represented in the ACS_{rx}, which requires considering the attitude of the vessel at reception and the mounting orientation of the receive transducer:

$$\overrightarrow{b_{rx}^{ACS}} = R_{ma,rc}^{T}\, R^{T}(0, \psi_{rx}, \omega_{rx})\, \overrightarrow{b_{rx}^{SCS}}), \tag{5.30}$$

$$\overrightarrow{b_{rx,y0z}^{ACS}} = \begin{bmatrix} x_{b_{rx,y0z}^{ACS}} \\ y_{b_{rx,y0z}^{ACS}} \\ z_{b_{rx,y0z}^{ACS}} \end{bmatrix} = \overrightarrow{b_{rx}^{ACS}} - (\overrightarrow{b_{rx}^{ACS}} \cdot (1,0,0))(1,0,0) \tag{5.31}$$

$$SRAR = \begin{cases} \arccos \dfrac{\left|\overrightarrow{b_{rx}^{ACS}} \cdot \overrightarrow{b_{rx,y0z}^{ACS}}\right|}{\left\|\overrightarrow{b_{rx}^{ACS}}\right\| \times \left\|\overrightarrow{b_{rx,y0z}^{ACS}}\right\|}, & x_{b_{rx,y0z}^{ACS}} \geq 0 \\ -\arccos \dfrac{\left|\overrightarrow{b_{rx}^{ACS}} \cdot \overrightarrow{b_{rx,y0z}^{ACS}}\right|}{\left\|\overrightarrow{b_{rx}^{ACS}}\right\| \times \left\|\overrightarrow{b_{rx,y0z}^{ACS}}\right\|}, & x_{b_{rx,y0z}^{ACS}} < 0 \end{cases} \tag{5.32}$$

where ψ_{rx} and ω_{rx} are the pitch and roll at the time of reception. The SRAR associated geometry is represented in Figure 5.14 (right).

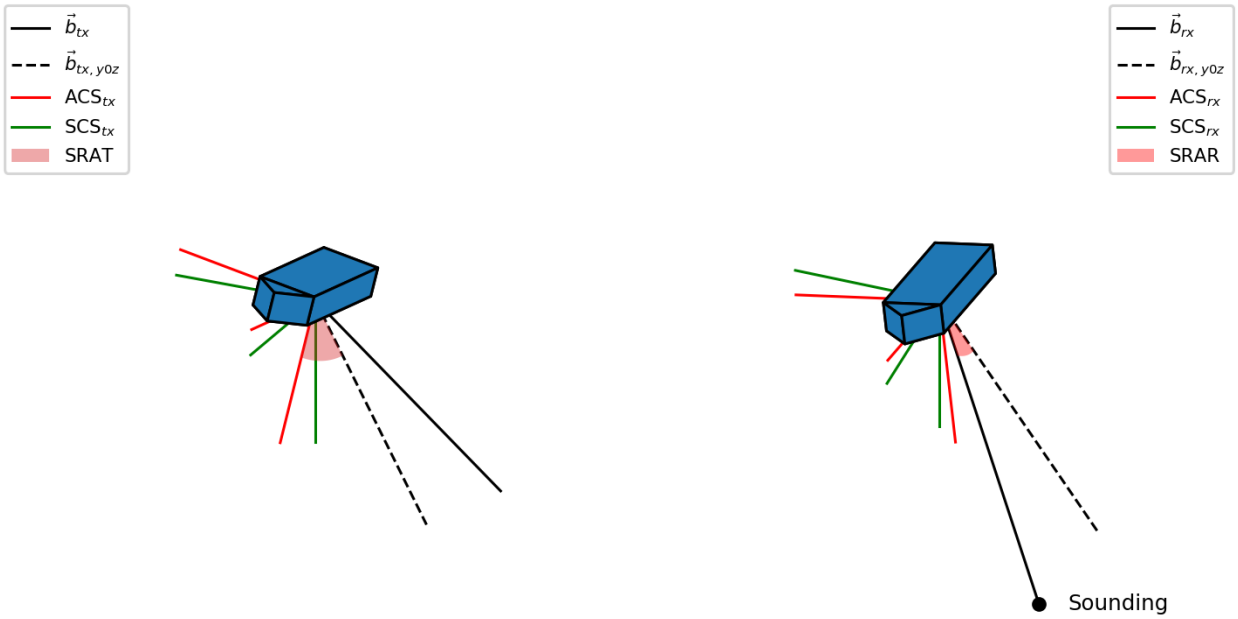

Figure 5.14: SRAT (left) and SRAR (right) associated geometries.

5.6. Extracting the S_b corrector

At this stage of the calibration process, the MBES bottom backscatter strength estimates are free from the TVG function and incorporate an improved ensonified area reduction. Furthermore, each estimate has an associated SRAT, SRAR and grazing angle (θ_g^{3D}).

Considering a particular transmit sector of a particular sonar mode, it is assumed that its calibration will be a function of SRAT and SRAR. Therefore, all the S_b^{noTVG} estimates are grouped by sector and by 1° bins of SRAT, SRAR and θ_g^{3D}, similar to the sorting performed by Hiroji (2016).

Note that this assumes that the transmit beam pattern is not roll-stabilized. There has been a suggestion that the two-dimensional transmit array of an EM712 do stabilize the transmit sectors across-track using roll at transmission (Kongsberg Maritime, 2018b). Looking at real EM710 and EM712 data (Figure 5.15), however, it is clear that the across-track pattern is rolling in a sonar

referenced frame. Part of this may be the receiver across-track component, especially at the outer most beams, but the fact that the roll-correlated pattern is seen also in the center sector suggests that the transmit pattern is not stabilized. For this thesis, it is therefore assumed that the EM710/EM712 transmitter is not roll-stabilized. For the EM2040P, of course, as the transmit arrays are one-dimensional, the transmit beam pattern cannot be roll-stabilized.

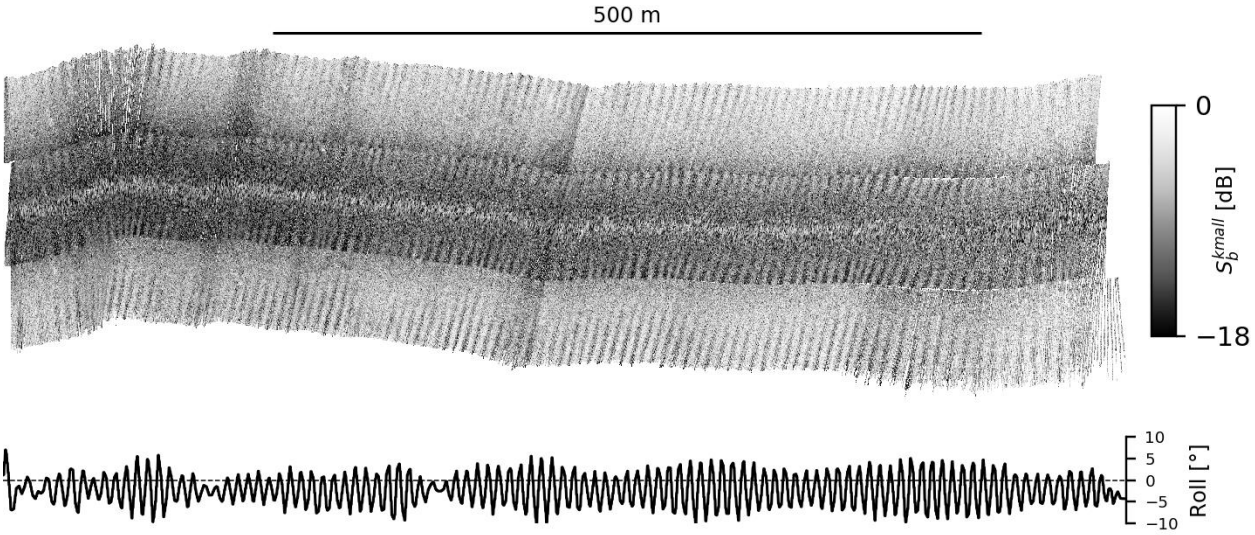

Figure 5.15: S_b^{kmall} mosaic generated with data collected under heavy roll, with visible beam pattern artifact. Data from an EM710 operating in Very Shallow / 70-100 kHz / Dual swath.

5.6.1. Obtaining an S_b correction from each sector/SRAT/SRAR/grazing angle bin

Each sector/SRAT/SRAR/θ_g^{3D} bin is evaluated individually with the objective of identifying a single S_b^{noTVG} value to compare to the respective sector reference ARC and deriving a correction (corr). Note that, unlike Hiroji (2016), the receiver and transmit patterns effects are not separated.

Identically to what is performed in equation 5.2, the bottom backscatter strength average of each bin (S_b^{bin}) is obtained through the unweighted average of the S_b^{noTVG} values in linear units.

Considering a bin defined by sector s, SRAT t, SRAR r, and θ_g^{3D} g, the associated reference bottom backscatter strength (S_b^{ref}) is obtained by inspecting the sector s reference ARC at the grazing angle g. From there, corr is obtained by subtracting S_b^{bin} from S_b^{ref} (equation 5.33). The process is illustrated by Figure 5.16.

$$corr = S_b^{ref} - S_b^{bin} \quad 5.33$$

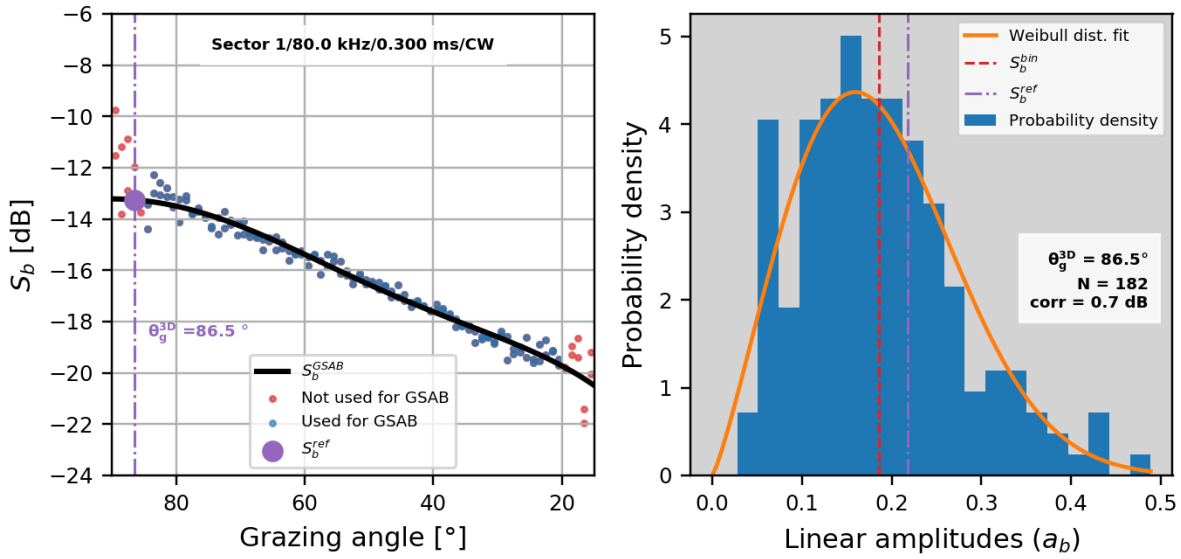

Figure 5.16: Estimating corr for a specific sector/SRAR/SRAT/ θ_g^{3D} bin. Left: Obtaining the S_b^{ref} from the sector's reference ARC at the adequate θ_g^{3D}. Right: Probability densities of bottom backscatter strength amplitudes (linear units) contained in a specific bin, overlayed by S_b^{bin} (red dashed line) and S_b^{ref} (purple dash dotted line).

5.6.2. Disambiguation of the correction for a specific sector/SRAT/SRAR combination

Since bins with the same sector/SRAT/SRAR but different θ_g^{3D} might provide different correction values (Figure 5.17), a disambiguation procedure is needed to obtain a single correction for each sector/SRAT/SRAR triplet. To deal with that, the bin containing the most S_b^{noTVG} values (N) is selected to provide the correction for the considered sector/SRAT/SRAR, while the remaining bins are neglected.

An alternate approach, although not utilized herein, could be to average the correctors for multiple bins (as long as there was a statistically significant number of samples in that bin). Indeed, the average could be weighed by the number of samples in each utilized bin.

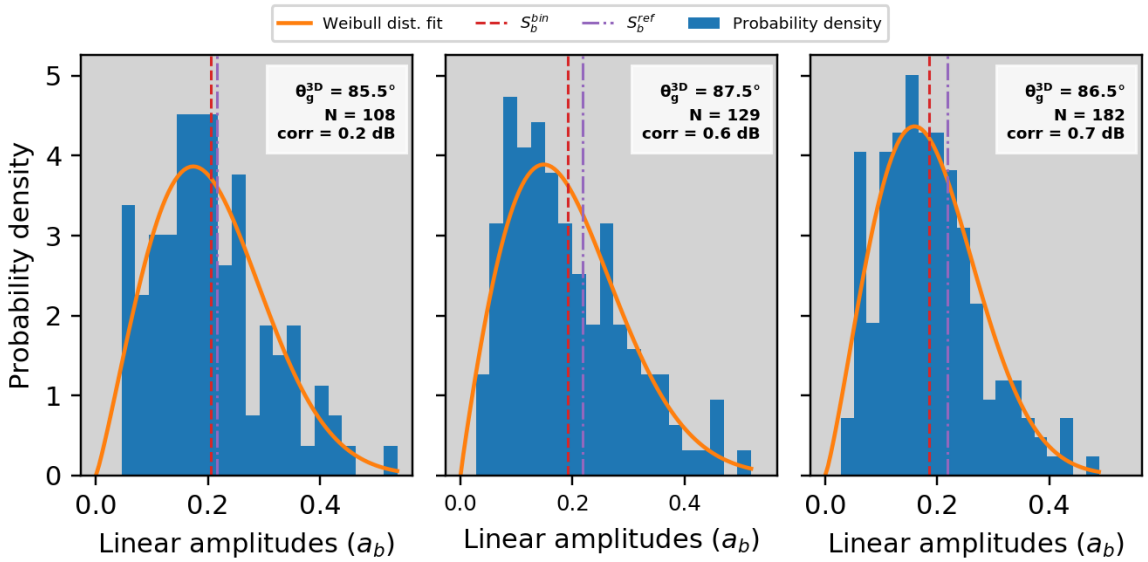

Figure 5.17: Bins sharing the same sector/SRAT/SRAR and different θ_g^{3D}. The correction for the considered sector/SRAT/SRAR would be derived from the bin represented in the center plot, since it has the largest number of S_b^{noTVG} values (N).

5.6.3. The final product: the correction heatmap

To offer an intuitive representation of the distribution of these calibration values, a correction heatmap is provided. It is valid for a specific sonar operating in a specific mode, and its purpose is to show how, for each sector, the correction varies with SRAR and SRAT. Figure 5.18 depicts a correction heatmap for an EM710 operating in the Very Shallow mode (70-100kHz) and dual swath:

- The 6 color coded maps provide, for each sector, the S_b correction associated to a SRAR/SRAT pair. The sectors of the first and second swath are respectively

described by the maps in the second and third rows. Conversely, the n^{th} column contains the correction maps associated to the n^{th} sector of each swath.

- The line plots in the top row describe how the S_b correction varies with SRAT for each sector. To achieve that, the correction maps are sliced at a specific SRAR (represented by a dashed grey line), illustrating the correspondent S_b correction SRAT dependence.
- The line plots on the right-hand side column describe how the S_b correction varies with SRAR. To accomplish that, a mean S_b correction per SRAR is obtained by averaging each sector's correction map SRAT-wise.

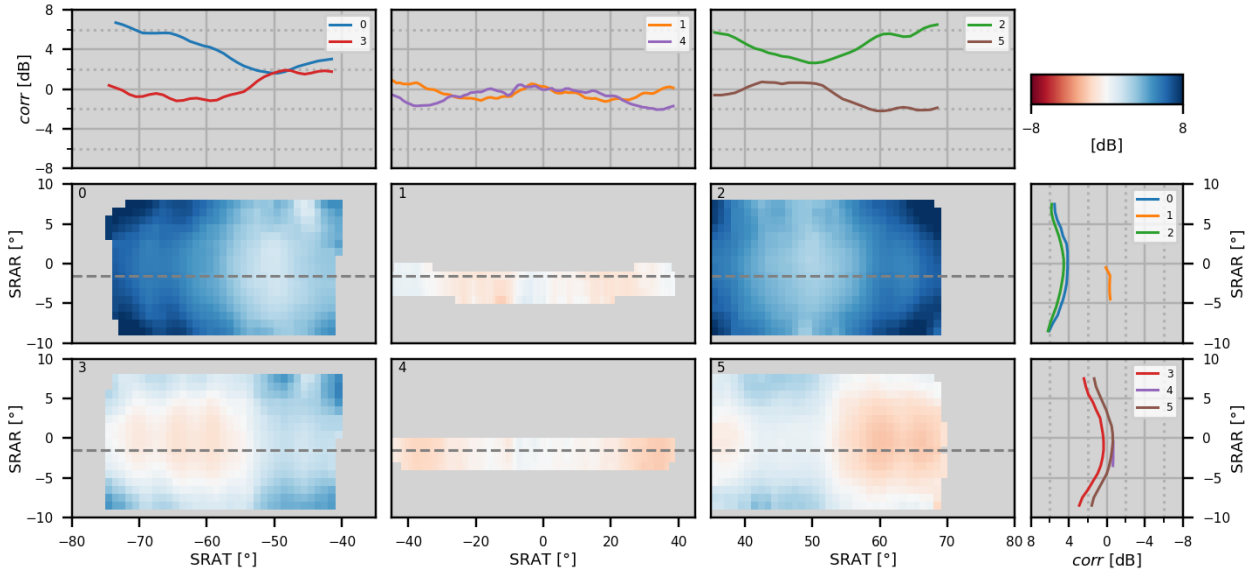

Figure 5.18: The correction heatmap generated for an EM710 operating in Very Shallow mode (70-100 kHz) and dual swath, with data acquired in the Cobbles reference area.

After the disambiguation step is performed for every sector/SRAT/SRAR, a two-dimensional centered moving average is applied to smooth the corr transition between adjacent

one degree SRAT/SRAR bins. While the window of the moving average is adjustable, it is by default set to consider only the adjacent SRAT/SRAR bins of a specific sector. This was done to remove rapid fluctuations in the SRAT/SRAR over a degree step that would not realistically be present in the radiation pattern of these arrays – Figure 5.19 represents a correction heatmap before applying the moving average.

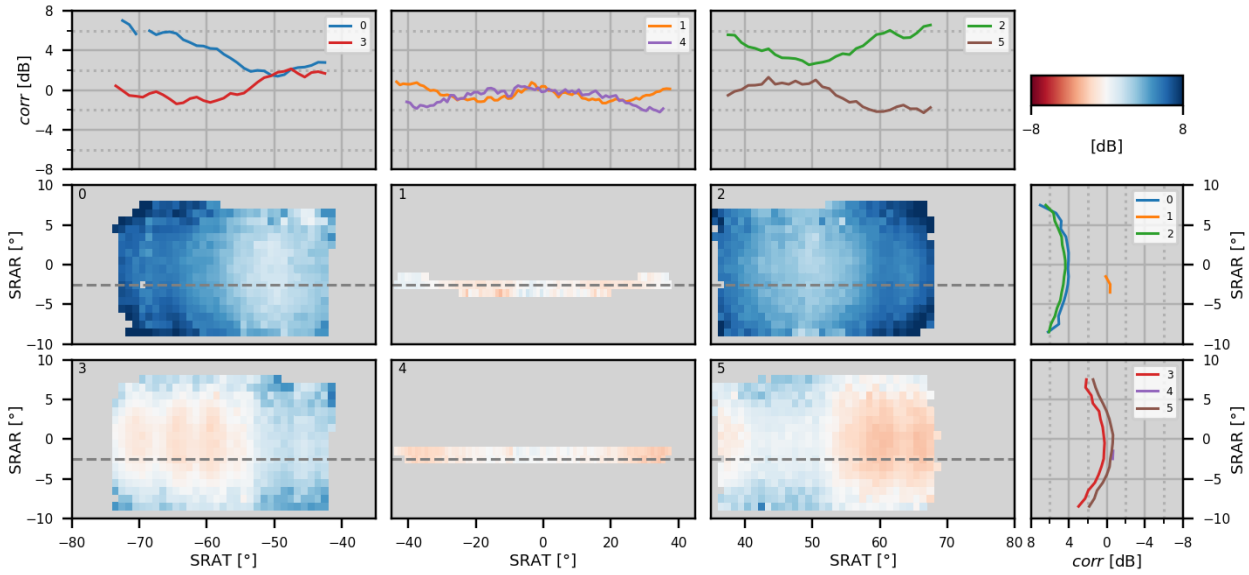

Figure 5.19: The correction heatmap generated for an EM710 operating in Very Shallow mode and dual swath, with data acquired in the Cobbles reference area, before applying the moving average.

To apply this heatmap to compatible data (same sonar and mode), every S_b^{noTVG} value must be correspondingly sorted by sector/SRAR/SRAT. After that step, the heatmap can be applied as defined in equation 5.34, where S_b^{corr} is the absolutely referenced (and calibrated) bottom backscatter strength, and S_b^{noTVG} and corr fall under the same sector/SRAT/SRAR bin.

$$S_b^{corr} = S_b^{noTVG} + corr \quad 5.34$$

6. RESULTS AND DISCUSSION

This chapter presents and discusses the final product of the methodology depicted in Chapter 5, describing the generated combined transmit/receive beam pattern corrections for different KM MBES, operating at different depth modes and with data acquired over different reference areas. Additionally, an attempt to establish a new reference area at another location by using a calibrated MBES through the methodology developed in this research is also addressed.

6.1. The reference data

The reference data used throughout this research consist of the multispectral absolutely referenced ARCs obtained by Guimarães (2020), for several areas in British Columbia, Canada, illustrated in Figure 6.1 and Figure 6.2.

As Guimarães (2020) points out, the multibeam data shows each area is reasonably flat with homogeneous sediment coverage. Furthermore, these areas are away from major navigation corridors and, since they are surrounded by islands, oceanographic conditions are generally favorable to surveying activities.

The multispectral ARCs of each area are presented in Figure 6.3. Considering that reference areas should have a specular component as negligible as possible, the Shell hash and Cobbles areas were deemed as the most suitable to apply the developed methodology.

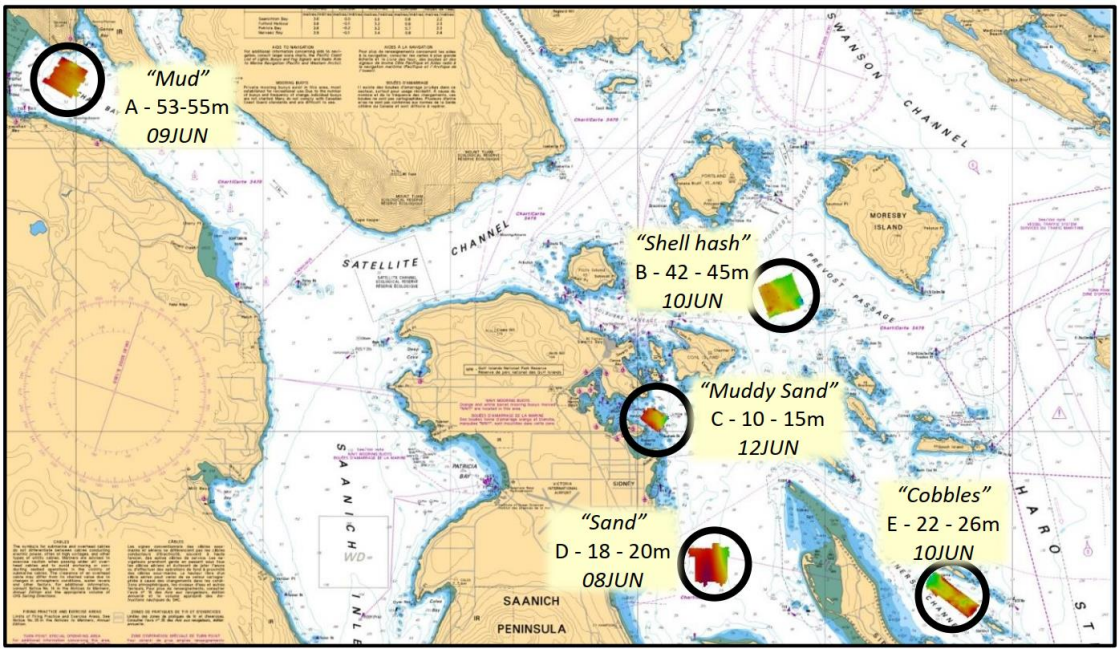

Figure 6.1: The location of the reference areas on the Nautical Chart CHS 3441 - Haro Strait Boundary Pass and Satellite Channel. From Guimarães (2020).

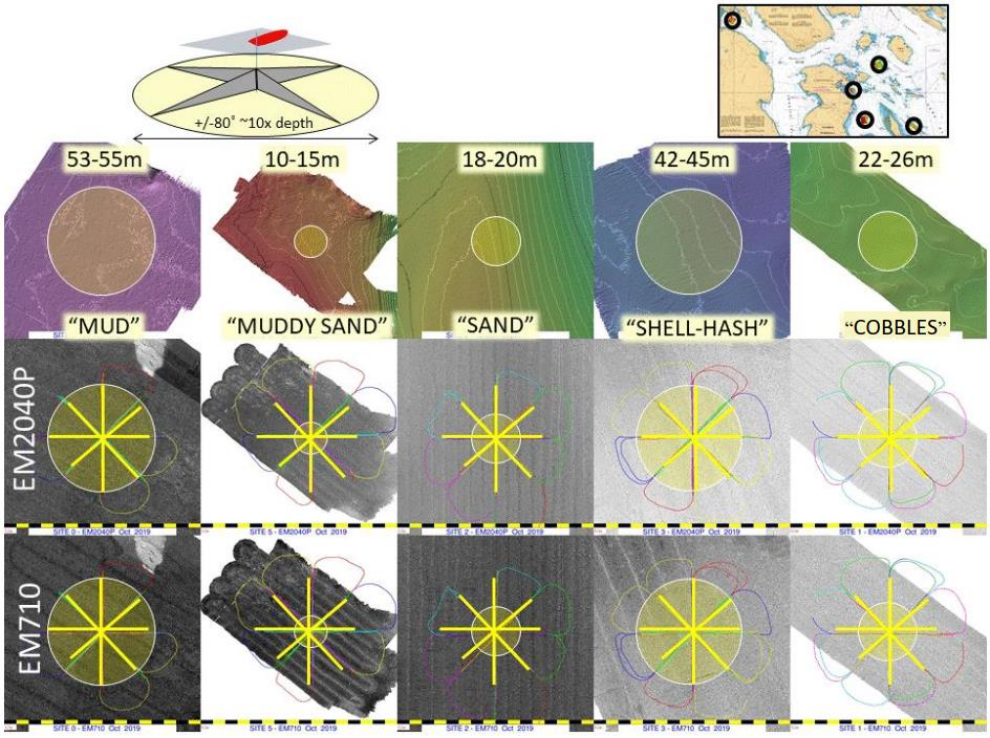

Figure 6.2: Bathymetry and backscatter acquired using EM710 and EM2040P over the five calibration sites. The sites are ordered from lowest (left) to highest S_b (right). The yellow circles indicate the radius of the area within which calibrated S_b was collected. From Guimarães (2020).

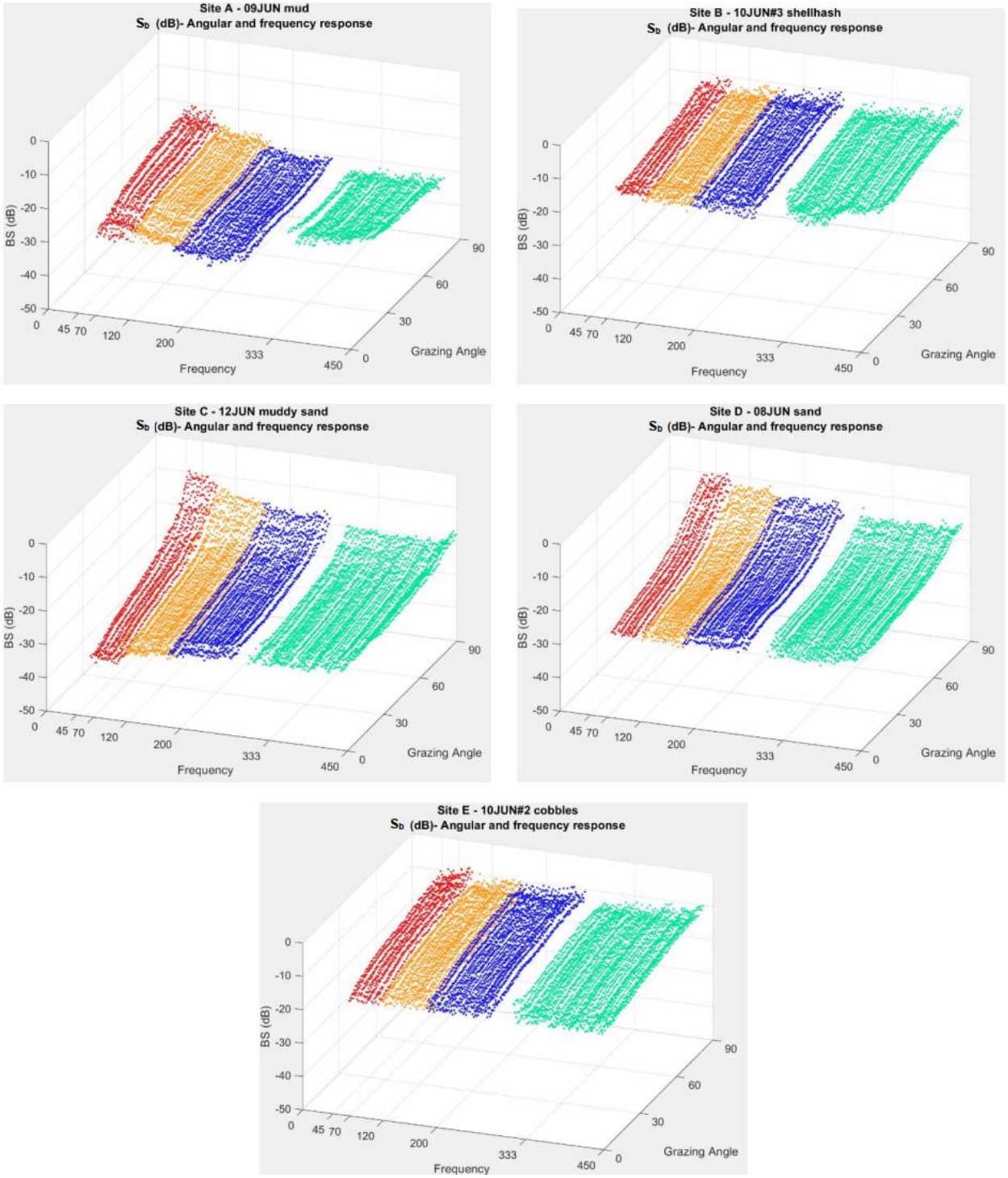

Figure 6.3: Multispectral ARC of each reference area. From Guimarães (2020).

6.2. The available uncalibrated MBES data

The already mentioned reference areas have been surveyed by several KM MBES with several modes, always with dual swath, as described in Table 6.1.

Table 6.1: KM MBES and depth modes used to survey the reference areas.

MBES model and main features	Modes (Frequency / τ_t / pulse modulation / bandwidth)	Reference areas
EM710 Multi-sector / Dual swath Beamwidths at 100 kHz: - Transmit/Receive: 1 ° - Receive: 2 ° Data format: .ALL Acquisition date: 2019	**Very Shallow** (70-100kHz / 0.300ms / CW / 5000Hz)	All
	Shallow (70-100kHz / 0.750ms / CW / 2000Hz)	Shell hash, Cobbles
	Medium (70-100kHz / 3.000ms / CW / 500Hz)	Shell hash, Cobbles
EM2040P Multi-sector / Dual swath Beamwidths at 400 kHz: - Transmit: 1 ° - Receive: 1 ° Data format: .KMALL (Rev. F) Acquisition date: 2019	**Shallow** (200kHz / 0.145ms / CW / 9974Hz) (300kHz / 0.101ms / CW / 14283Hz)	All
	Medium (200kHz / 0.288ms / CW / 5004Hz) (300kHz / 0.288ms / CW / 5004Hz)	Shell hash, Cobbles
	Deep (200kHz / 0.865ms / CW / 1661Hz) (300kHz / 0.865ms / CW / 1661Hz)	Shell hash, Cobbles
	Very Deep (200kHz / 3.000ms / FM / 1627Hz) (300kHz / 2.000ms / FM / 1675Hz)	Shell hash, Cobbles
EM712 Multi-sector / Dual swath Beamwidths at 100 kHz: - Transmit: 1 ° - Receive: 2 ° Data format: .KMALL (Rev. H) Acquisition date: 2022	**Very Shallow** (70-100kHz/ 0.299ms / CW / 5000Hz)	Sand, Shell hash, Cobbles
	Shallow (70-100kHz / 0.733ms / CW / 1999Hz)	Sand, Shell hash, Cobbles
	Medium (70-100kHz / 2.887ms / CW / 500Hz)	Sand, Shell hash, Cobbles
	Very Shallow (40-70kHz / 0.299ms / CW /5000Hz)	Sand, Shell hash, Cobbles
	Shallow (40-70kHz / 0.733ms / CW / 1999Hz)	Shell hash, Cobbles
	Medium (40-70kHz / 2.887ms / CW / 500Hz)	Shell hash
EM2040C ~~Multi-sector~~ / Dual swath Beamwidths at 400 kHz: - Transmit: 1 ° - Receive: 1 ° Data format: .KMALL (Rev. I) Acquisition date: 2022	**Shallow** (300kHz / 0.073ms / CW / 19949Hz)	Sand, Cobbles
	Medium (300 kHz / 0.145ms / CW / 9963Hz)	Sand, Shell hash, Cobbles
	Deep (300kHz / 0.361ms / CW / 3994Hz)	Sand, Shell hash, Cobbles
	Deeper (300kHz / 0.865ms / CW / 1661Hz)	Sand, Shell hash, Cobbles
	Extra Deep (300kHz / 3.000ms / FM / 2603Hz)	Cobbles

6.3. From S_b^{all} to S_b^{corr}

Throughout this section, the methodology presented in Chapter 5 will be applied to a specific dataset, where the MBES data was acquired over the Shell hash reference area with an EM710 operating in Very Shallow / 70-100 kHz / dual swath (characterized in Table 6.2).

Table 6.2: KM EM710 Very Shallow depth mode main characteristics.

EM710 / VERY SHALLOW MODE / 70-100 kHz / DUAL SWATH					
Sector ID	Swath	Frequency [kHz]	τ_t / τ_{eff} [ms]	Pulse modulation	Bandwidth [kHz]
0	0	70	0.300 / 0.111	CW	5
1		80			
2		70			
3	1	90			
4		100			
5		90			

6.3.1. The reference ARCs

The reference ARC in a 10 kHz band around the center frequency of each sector was extracted from the multispectral ARC associated to the Shell hash area as described in Subsection 5.1.2. The grazing angle range used to fit the GSAB model spanned between 20 and 85°, avoiding the noisy data at low grazing angles and at near normal incidence (Figure 6.4).

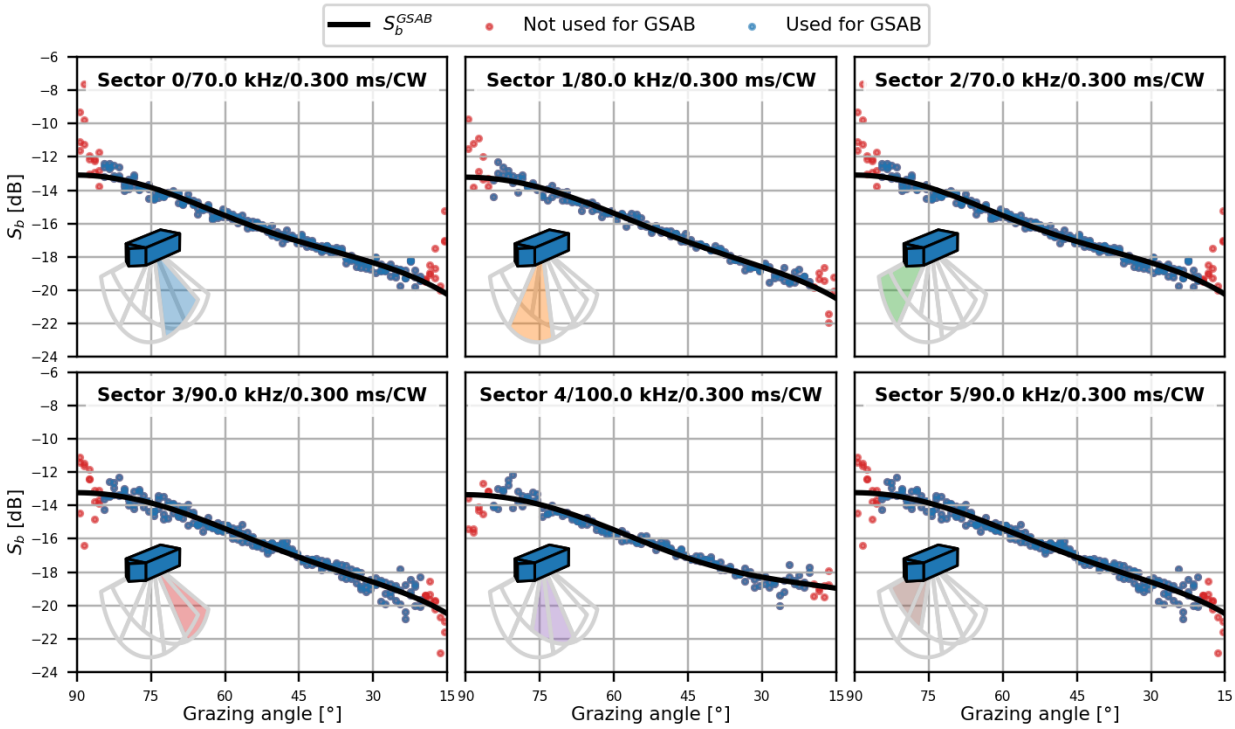

Figure 6.4: Reference ARCs obtained from the Shell hash reference area for the sector frequencies of an EM710 operating in Very Shallow / 70-100 kHz / Dual swath. Only grazing angles within 25 and 80° were considered to generate the GSAB models.

The resulting 100 kHz reference ARC looks slightly different from the others, especially at low grazing angles. By examining Table 6.3, which contains the parameters for each sector's frequency associated GSAB model, it becomes apparent that the D parameter for 100 kHz is considerably different.

Table 6.3: GSAB model parameters retrieved from the Shell hash reference area for the frequencies used by an EM710 operating in Very Shallow / 70-100 kHz / Dual swath.

Frequency [kHz]	10 log A [dB] (specular peak)	B [°] (specular peak extent)	10 log C [dB] (Oblique Sb)	D (Angular roll-off)
70	-15.8	18.84	-16.4	0.65
80	-15.6	21.64	-17.0	0.60
90	-15.6	21.58	-17.0	0.61
100	-15.0	23.47	-18.3	0.13

Slicing the multispectral ARC (before fitting the GSAB model) at discrete grazing angles, reveals that there is a step between the data collected with the ES70-CD and the data collected with the ES120-7CD, more evident at low grazing angles (Figure 6.5). Furthermore, the 100 kHz reference ARC is the only one obtained with data acquired with the ES120-7CD (all other being derived from the ES70-CD). This suggests that the blending between individual spectra from each SBES transducer is slightly imperfect (see Subsubsection 5.1.2.1 where the ripples and trends were smoothed) and that this is leaking into the fidelity of the reference.

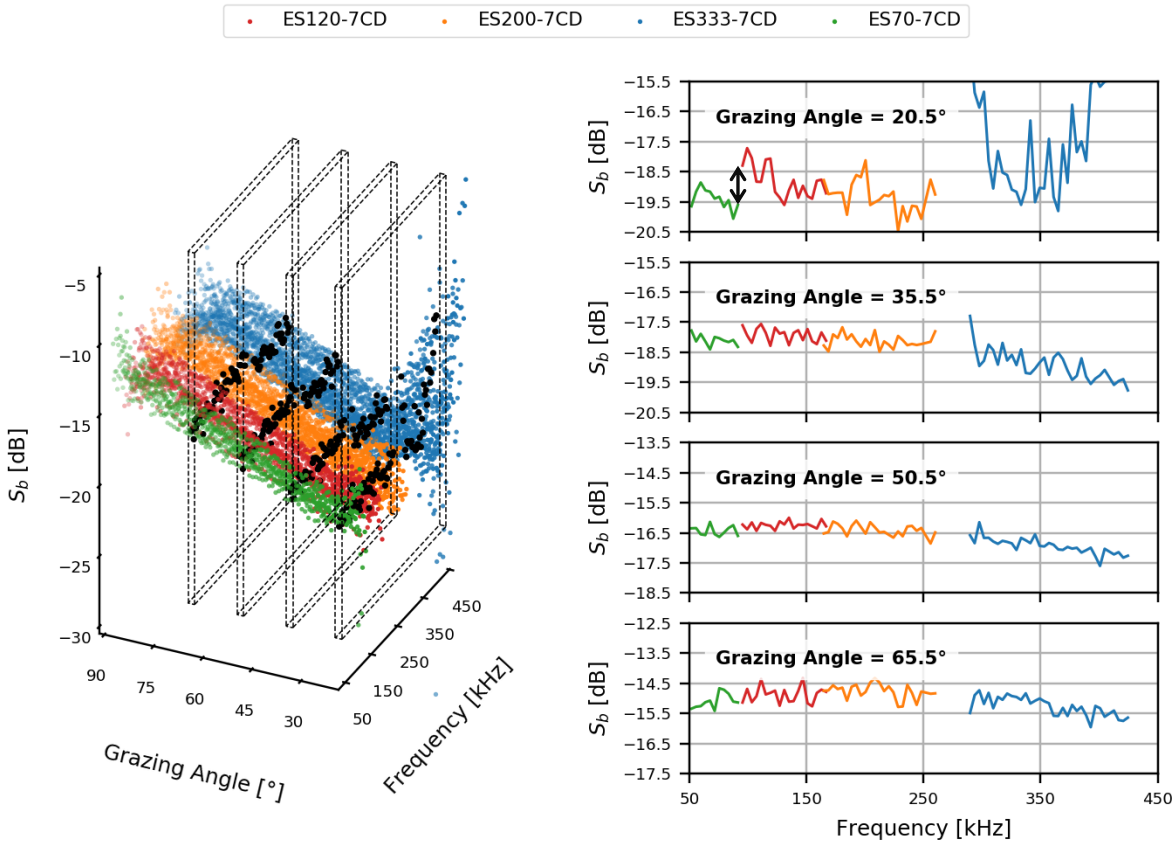

Figure 6.5: Slices of the multispectral ARC associated with the Shell hash reference area at several discrete grazing angles. For low grazing angles, note the difference between the frequency response obtained with the ES70-7CD and the ES120-7CD (black arrow) and how the low signal to noise ratio impacts the output of the ES333-7CD.

6.3.2. Computing the TVG

The MBES data under consideration is in the .ALL format, thus the TVG must be estimated according to Subsection 5.2.3, since, unlike the .KMALL format, the applied gain is not recorded in the raw data. Figure 6.6 shows the computed TVG_{all} applied to the S_b^{all} values of a specific swath of a specific survey line, as well as its components: $NNIC_{all}$, EAC_{all} and LC_{all}.

It is important to highlight that the existing documentation (Hammerstad, 2000; Kongsberg Maritime, 2018a) does not specify all the details required for computing EAC_{all}. For this dataset, the total pulse length (not accounting for amplitude shading) and the nominal beamwidths (not accounting for steering or frequency shifts) were used.

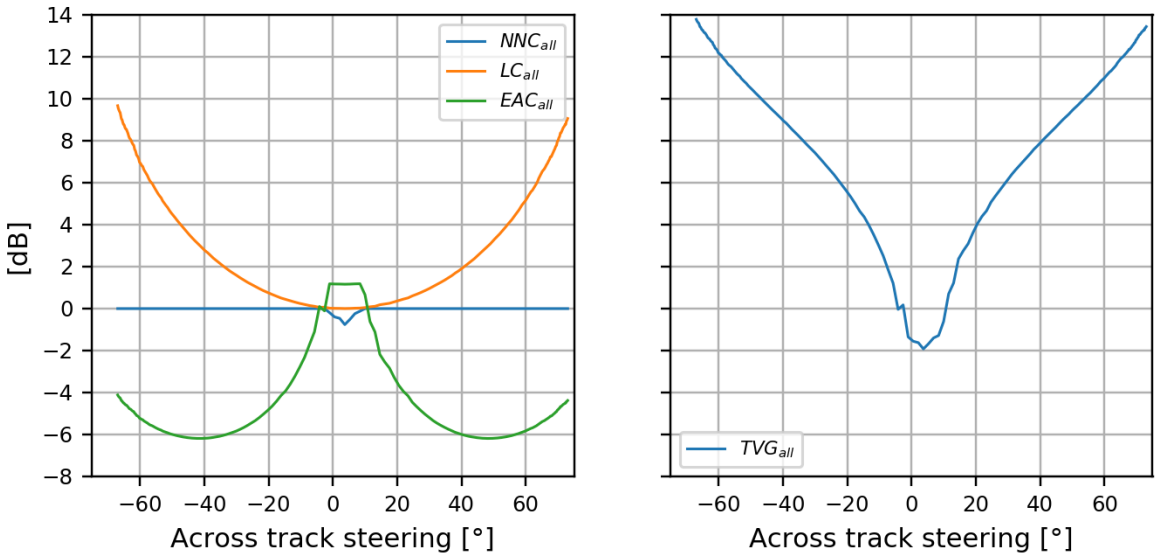

Figure 6.6: TVG_{all} and its components applied to the S_b^{all} values in a particular swath/line of the dataset under analysis: EM710 / Very Shallow / 70-100 kHz / Dual swath / Shell hash.

6.3.3. Grazing angle determination

The estimation of the grazing angle associated to each S_b^{all} value is required to construct the reference area ARC with the MBES data and to obtain improved ensonified area estimates (EAC_{imp}). The methodology involved in computing the grazing angle uses a DTM created with the MBES bathymetric data. For the dataset under analysis, the DTM depicted in Figure 6.7, with a resolution of 2 m, was used. Subsequently, by computing the beam vector for each S_b^{all} value, as described in Section 5.3, the across-track, along-track and 3D grazing angles were computed (Figure 6.8).

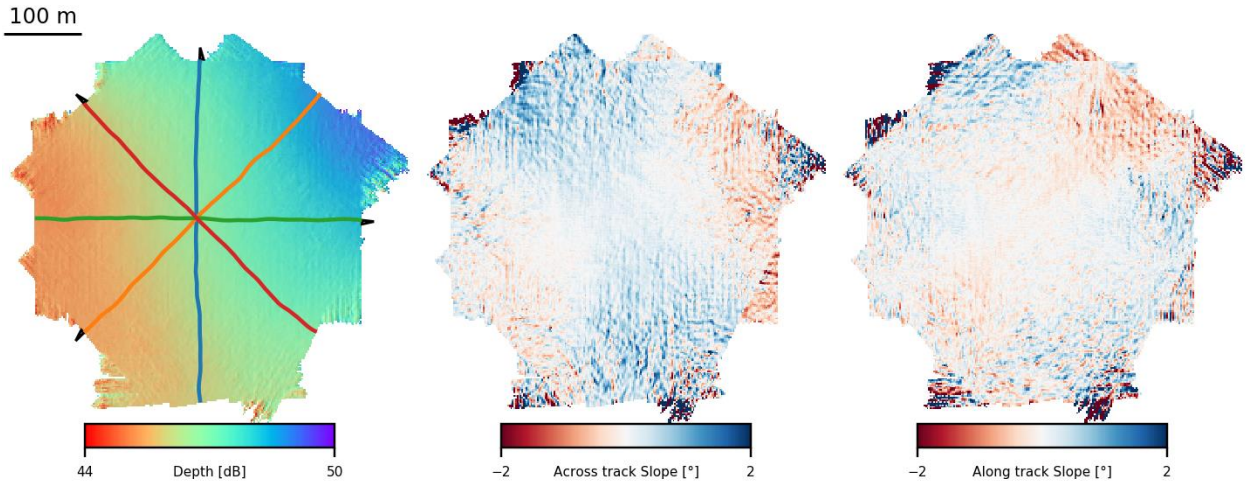

Figure 6.7: Left: Tide corrected depth DTM overlayed with the navigation-track of the survey lines; Center: Across-track bottom slope; Left: Along-track bottom slope. All grids with 2 m resolution. Dataset under analysis: EM710 / Very Shallow / 70-100 kHz / Dual swath / Shell hash.

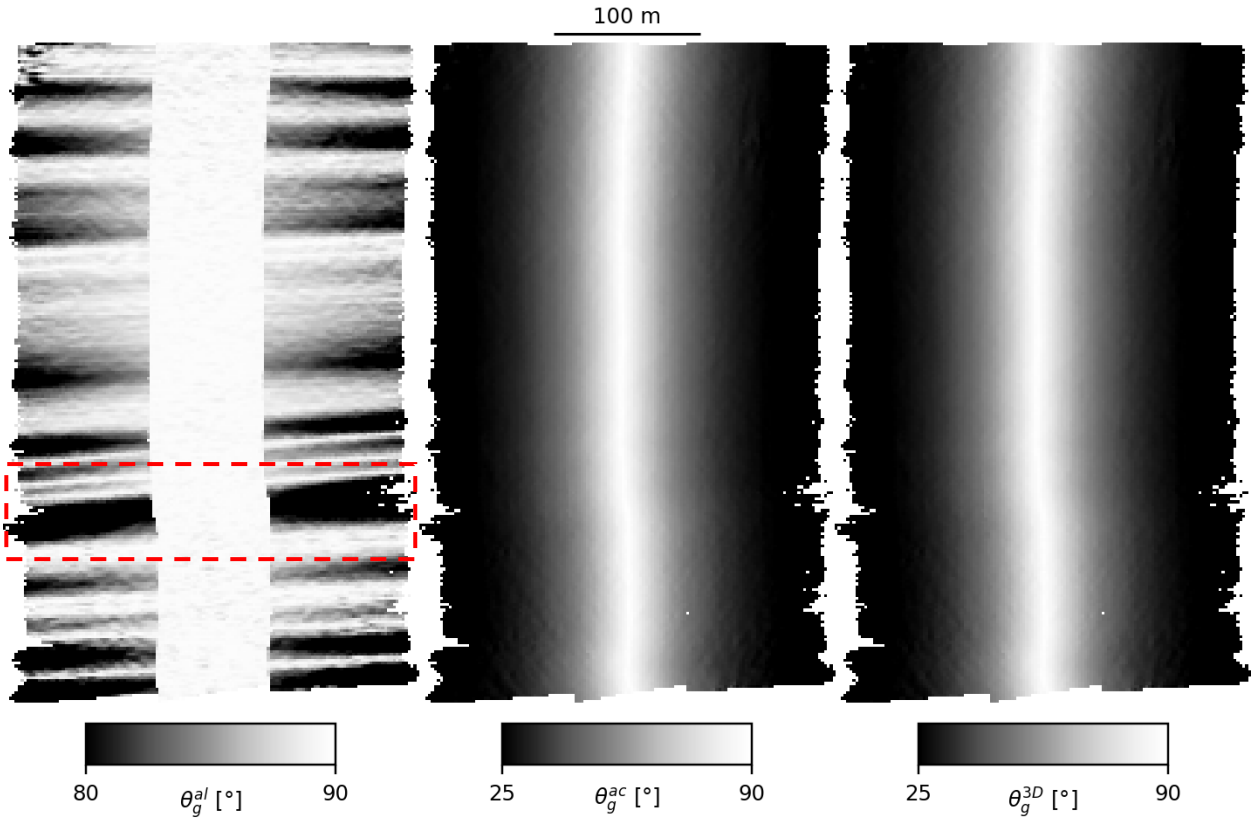

Figure 6.8: Computed grazing angles for one survey line of the dataset (2m resolution grids). Left: Along-track grazing angle. Center: Across-track grazing angle. Right: 3D grazing angle. The red dashed box identifies an area with low along-track grazing angles for the outer sectors. Dataset under analysis: EM710 / Very Shallow / 70-100 kHz / Dual swath / Shell hash.

6.3.4. Improving the ensonified area correction

Improving the ensonified area correction requires knowledge of the along- and across-track grazing angles, the actual transmit and receive beamwidths (by applying equation 5.14) and the effective pulse length (by applying equation 5.24). For a specific survey line of the dataset under analysis, EAC_{all} and EAC_{imp} are depicted in Figure 6.9. Furthermore, the EAC_{all} and EAC_{imp} computed for the dataset under analysis are binned by the 3D grazing angle in Figure 6.10.

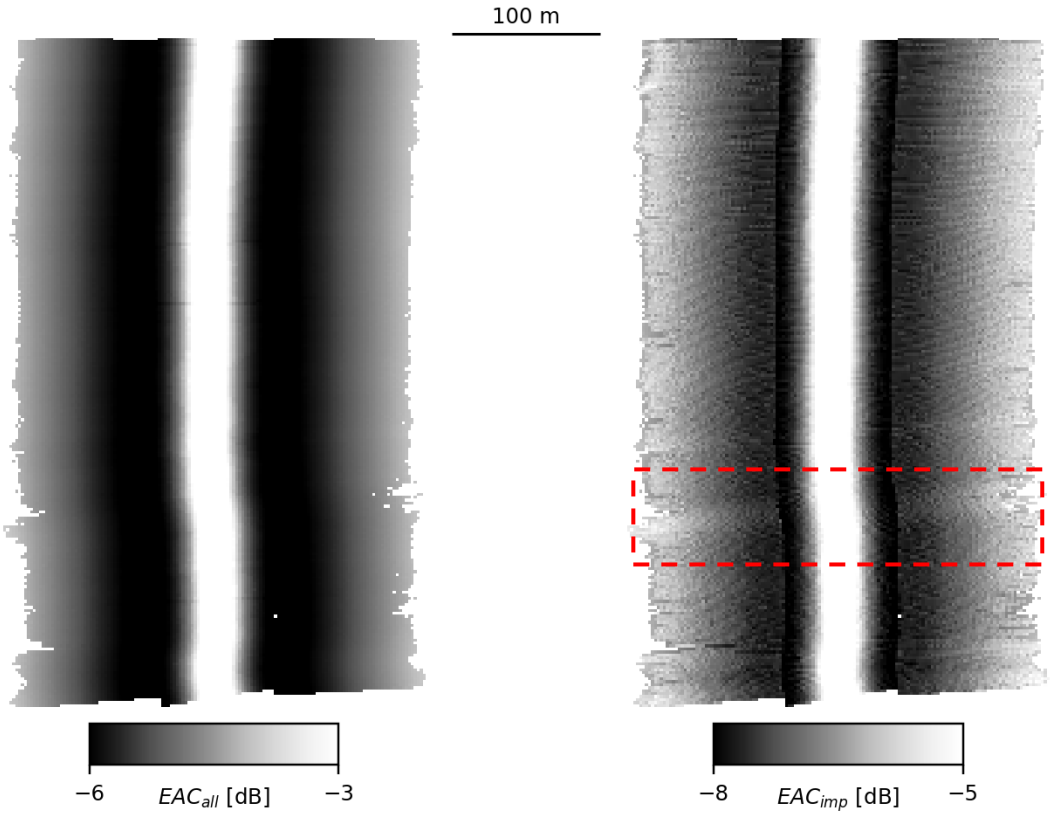

Figure 6.9: EAC_{all} (left) and EAC_{imp} (right) for a specific survey line (2m resolution grids). The red dashed box highlights the effect of particularly low along-track grazing angles in the EAC_{imp} (outer sectors). Dataset under analysis: EM710 / Very Shallow / 70-100 kHz / Dual swath / Shell hash.

Contrasting with EAC_{all}, EAC_{imp} is clearly sector dependent, which is explained by the beamwidth dependence on each sector's frequency. This frequency dependence is not noticeable for sectors of different swaths since Figure 6.9 does not have enough resolution to represent each individual profile. Nevertheless, the effect of the second swath using different frequencies is evident on Figure 6.10.

Additionally, EAC_{imp} is modulated by the computed along and across-track grazing angles. The influence of the along-track grazing angle is quite noticeable, especially for high grazing angles, as observed in Figure 6.9. On the other hand, EAC_{all}, while incorporating an estimate of

the grazing angle throughout the swath, by virtue of the algorithm, cannot account at all for the along-track morphology of the bottom.

In Figure 6.10, EAC_{all} presents a step that corresponds to the transition from a pulse length to a beamwidth limited ensonified area. EAC_{imp} handles that regime change through equation 5.25, smoothing the transition.

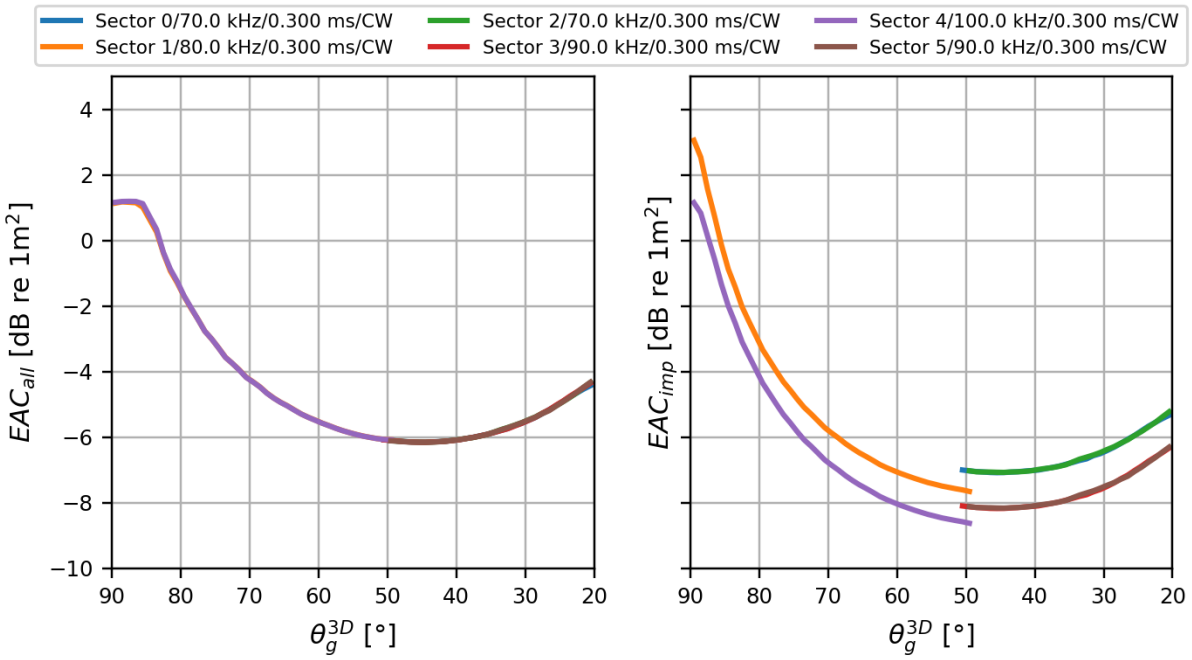

Figure 6.10: EAC_{all} (left) and EAC_{imp} (right), binned by 3D grazing angle. The entire dataset under analysis was used to generate this figure. Dataset under analysis: EM710 / Very Shallow / 70-100 kHz / Dual swath / Shell hash.

6.3.5. Sonar referenced angles computation

The computed sonar referenced angles, SRAR and SRAT, are presented side to side to the transmit and receive steering angles in Figure 6.11 and Figure 6.12, respectively. In this particular case, the steering angles and the sonar referenced angles appear to be inversely correlated. That occurs because the heading mounting angles of the transmit and receive transducers are offset by 180°.

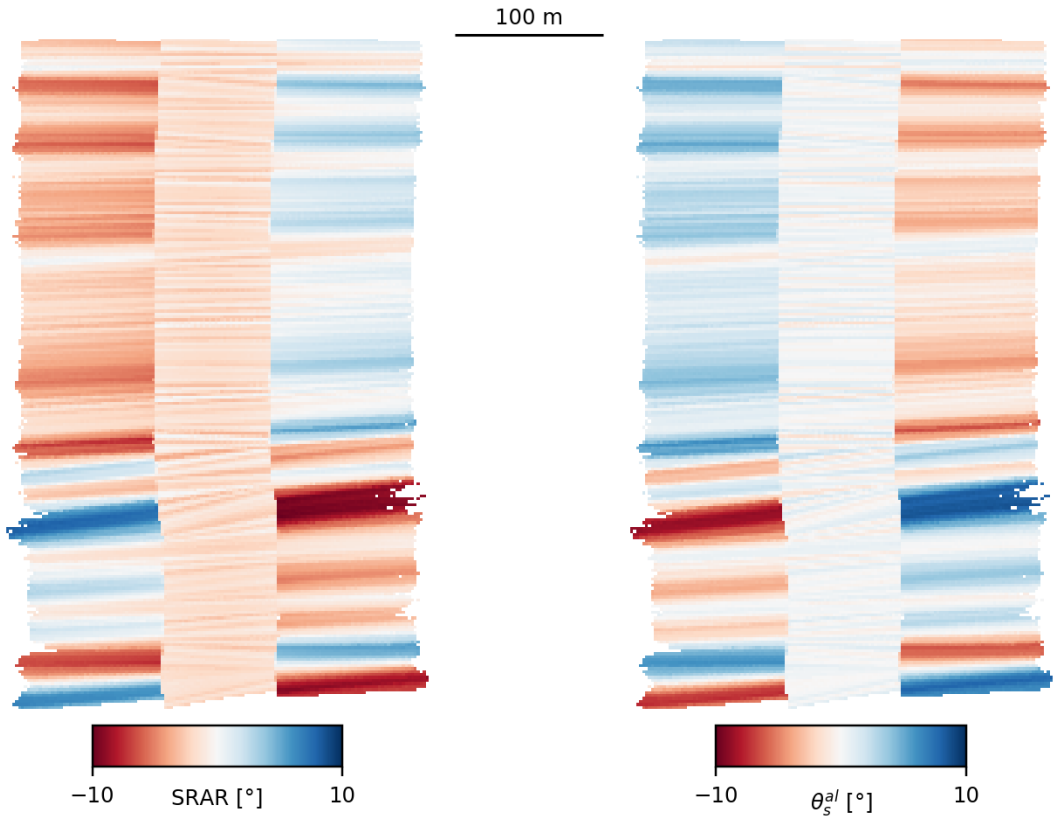

Figure 6.11: SRAR (left) and transmit steering angle (right) for a specific survey line (2m resolution grids). Dataset under analysis: EM710 / Very Shallow / 70-100 kHz / Dual swath / Shell hash.

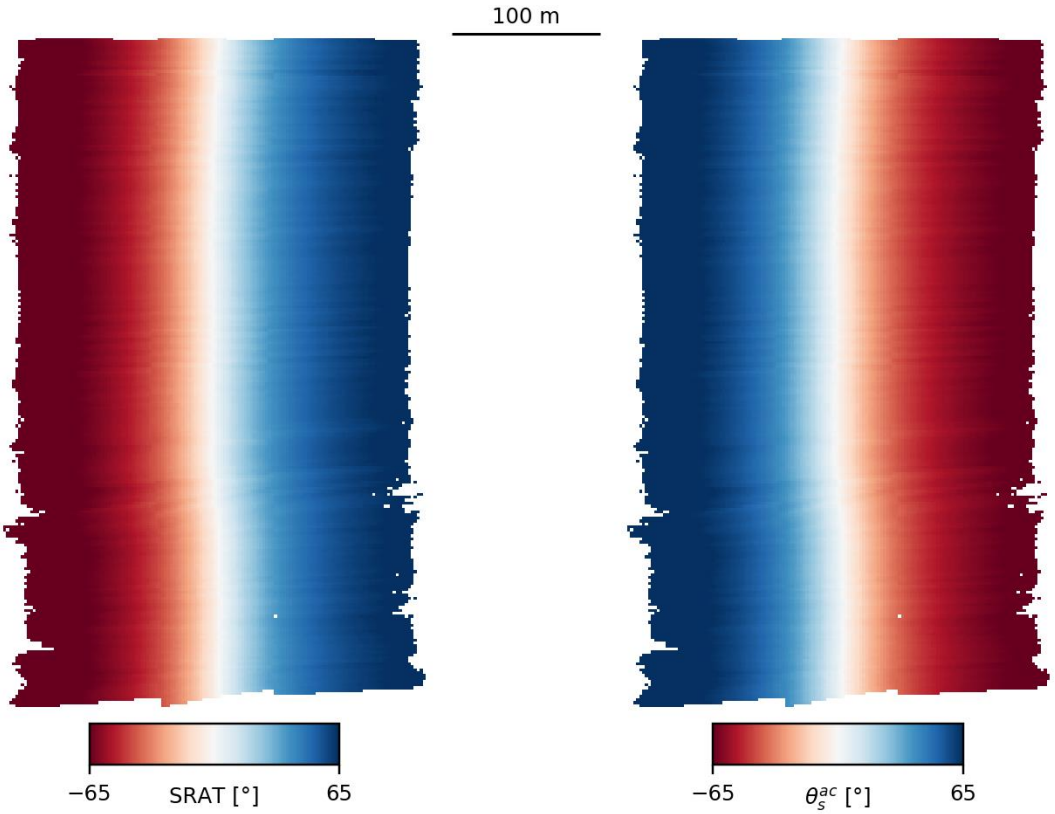

Figure 6.12: SRAT (left) and receive steering angle (right) for a specific survey line (2m resolution grids). Dataset under analysis: EM710 / Very Shallow / 70-100 kHz / Dual swath / Shell hash.

6.3.6. The correction heatmap

The final product of the entire process is the correction heatmap. For each sector/SRAT/SRAR permutation, an adequate correction is provided. The heatmap obtained with this particular dataset (Figure 6.13) shows corrections that span from -2 to 8 dB. Still, while not mentioned in the .ALL format documentation, there must be an undisclosed SL and M model applied to the S_b^{all} values. The corrections provided for the heatmap operate on top of that SL and M models.

Notably, each sector's SRAT averaged correction curve (maps on the further right column of Figure 6.13) presents a 2 dB drop (SRAR = ± ~10°) from its maximum (SRAR = ~0°). This

pattern is only evident for the outer sectors, whose SRAR values vary more expressively as a consequence of the transmit steering required to perform yaw stabilization. The center sectors are not steered as heavily, resulting in this correction roll-off not being as perceptible.

Figure 6.14 shows the count heatmap. This map should be read in the same fashion as the correction heatmap. However, each pixel now corresponds to the number of S_b^{noTVG} values used to compute each sector/SRAT/SRAR correction. Note that the represented number of observations is also constrained by the considered grazing angle to generate the correction (see Subsection 5.6.2). The map is compatible with an equidistant beam spacing (which was in fact used during acquisition). Furthermore, it reveals that the port side sectors (0 and 3) were predominantly steered aft, meaning that the corrections computed for large positive SRAR are generated from fewer S_b^{noTVG} values and probably less accurate. The opposite is valid for the starboard side sectors (2 and 5). Regarding the center sectors (1 and 4), the smaller associated transmit steering prevents the computation of a valid correction for large absolute SRAR values.

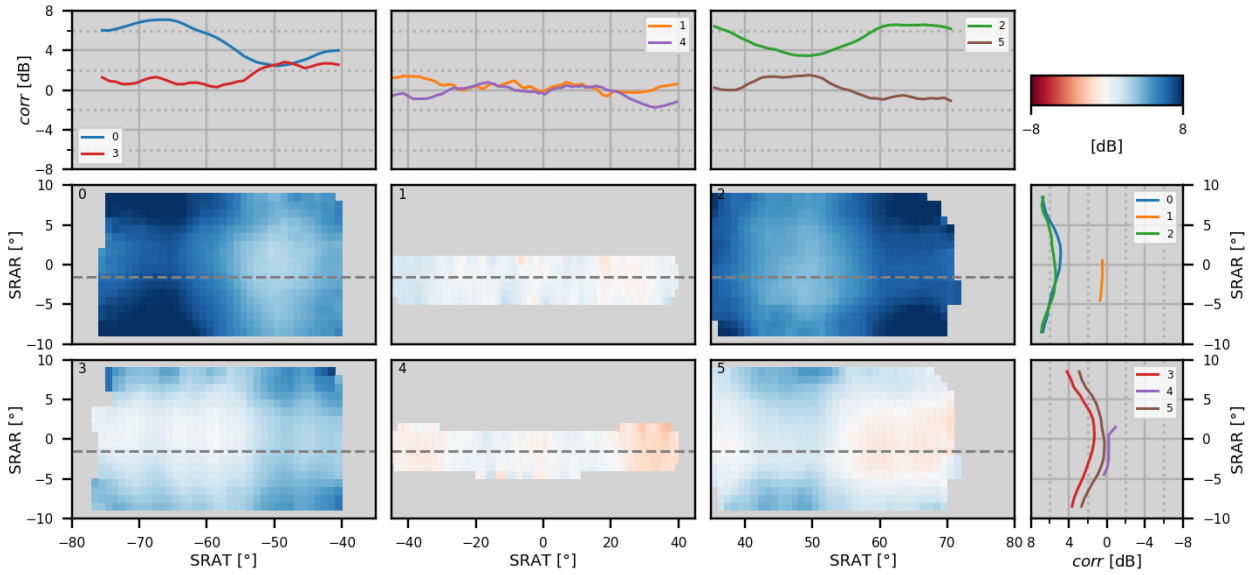

Figure 6.13: The correction heatmap generated with the dataset under analysis: EM710 / Very Shallow mode / Shell hash reference area.

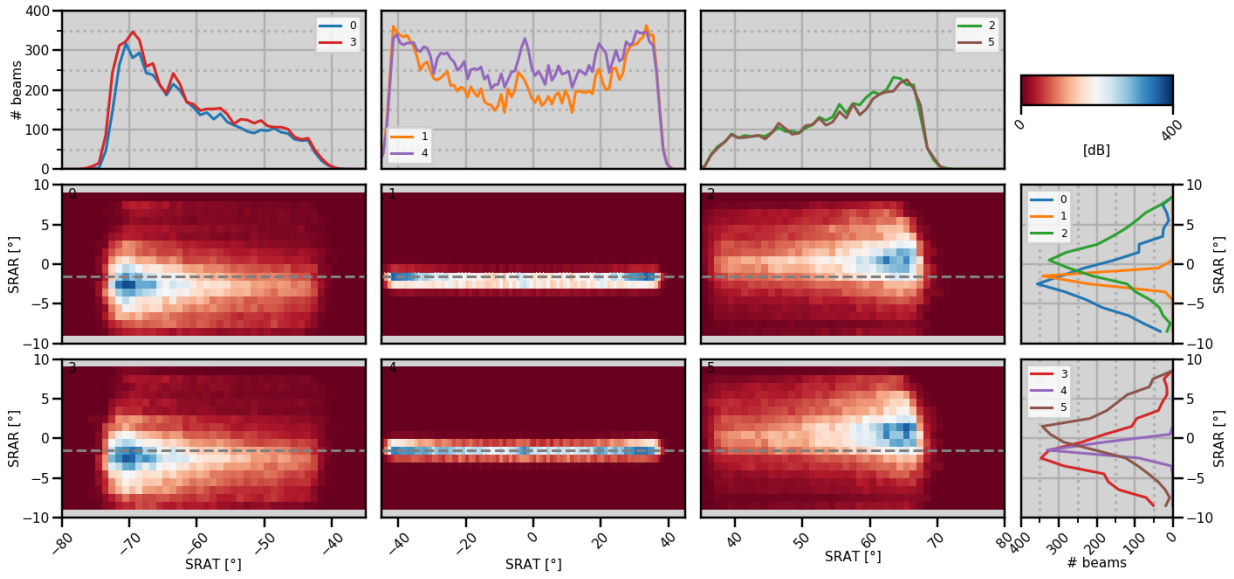

Figure 6.14: The count heatmap generated with the dataset under analysis: EM710 / Very Shallow mode / Shell hash reference area.

6.3.7. S_b estimates throughout the process

The bottom backscatter strength values initially provided by the MBES (S_b^{all}), which utilize the original TVG_{all}, can be binned by grazing angle to obtain an ARC. Figure 6.15 presents such an attempt, revealing how far apart the obtained angular dependence is from the reference ARCs. While far from the reference, since a distinct ARC is computed for each survey line (all performed in different directions) and each line shares the same biases, this analysis has the merit to rule out azimuth dependency as every line's ARC seems to match the remaining reasonably well.

The same exercise can be performed with the S_b^{noTVG} values, as depicted in Figure 6.16. Although the ARC now obviously looks less flattened (the TVG has been removed – no Lambertian or near normal incidence corrections applied), it still presents departures from the reference ARC of up to ~6 dB.

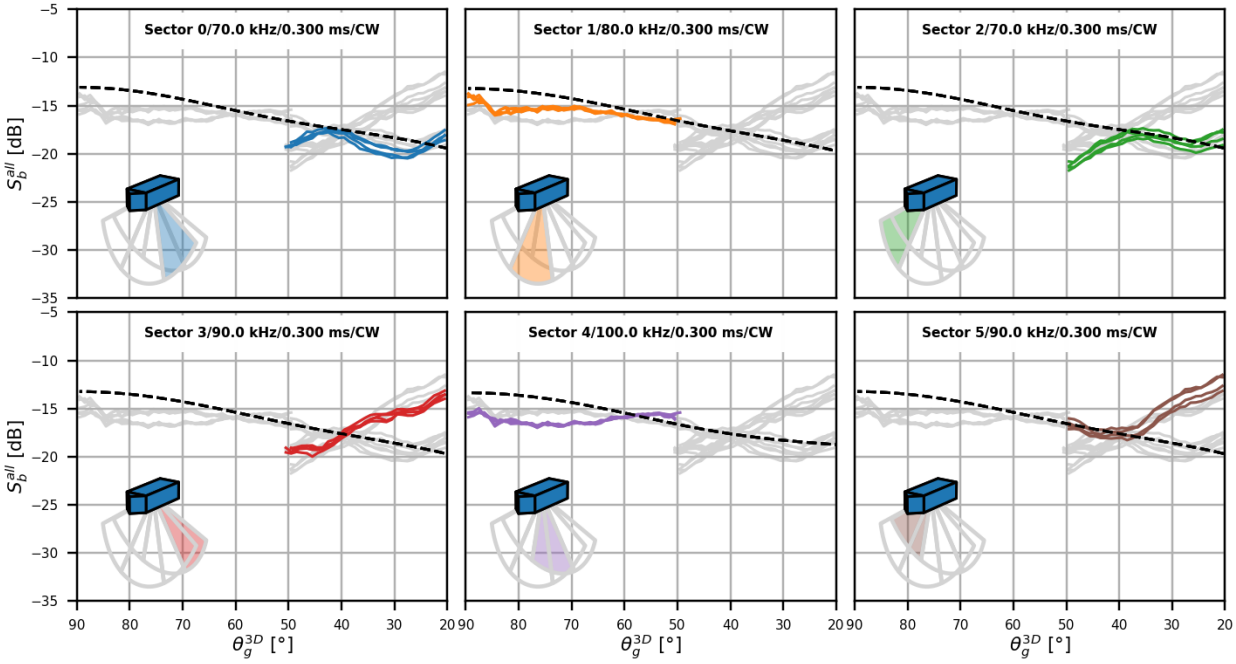

Figure 6.15: S_b^{all} ARC per survey line, separated by sector. S_b^{all} has a flattened ARC since it encompasses the TVG_{all}, which includes the LC_{all} and the $NNIC_{all}$. The dashed black line represents the reference ARC for the respective sector. Dataset under analysis: EM710 / Very Shallow / 70-100 kHz / Dual swath / Shell hash.

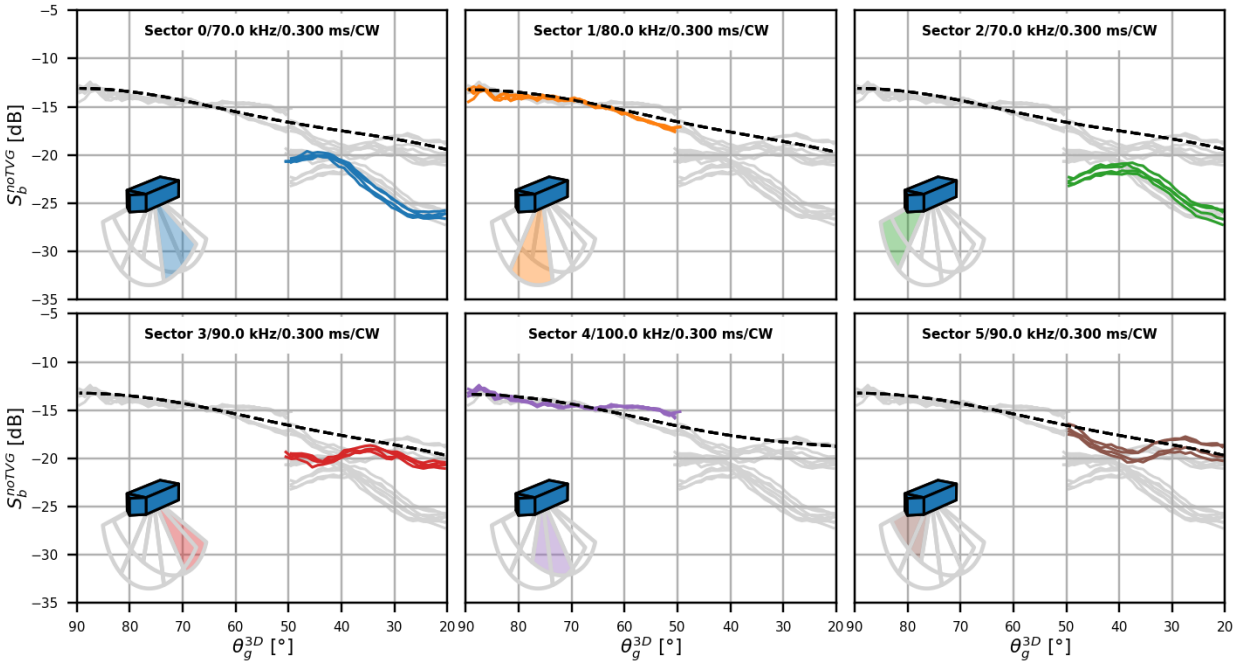

Figure 6.16: S_b^{noTVG} ARC per survey line, separated by sector. The dashed black line represents the reference ARC for the respective sector. Dataset under analysis: EM710 / Very Shallow / 70-100 kHz / Dual swath / Shell hash.

After the application of the correctors indicated in the correction heatmap (Figure 6.13), when the S_b^{corr} values are considered, the obtained angular dependences now closely match the corresponding sector reference ARC (Figure 6.17).

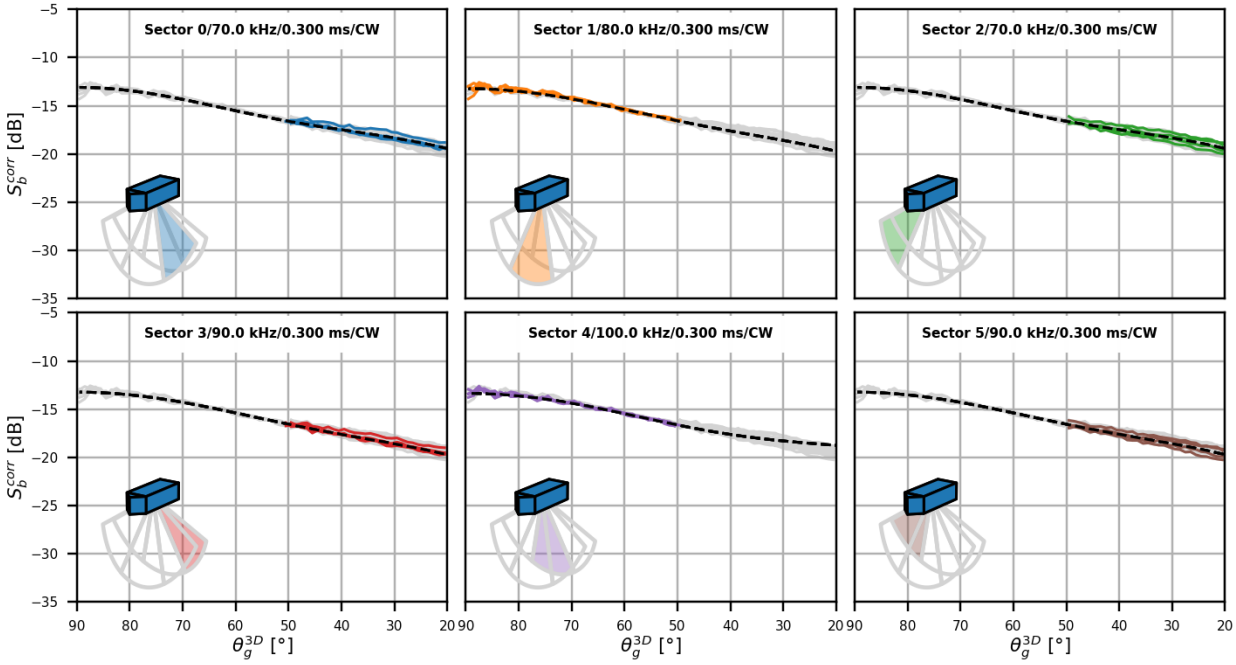

Figure 6.17: S_b^{corr} ARC per survey line, separated by sector. The dashed black line represents the reference ARC for the respective sector. Dataset under analysis: EM710 / Very Shallow / 70-100 kHz / Dual swath / Shell hash.

To provide an alternate perspective of the transition between each processing stage, Figure 6.18 shows the obtained mosaics with S_b^{all}, S_b^{noTVG} and S_b^{corr}. The S_b^{corr} mosaic no longer presents sector boundaries and is free of most artifacts visible in the earlier processing stages. The highlighted area of the S_b^{corr} mosaic with no information occurs because the corresponding SRARs are outside of the correction heatmap range – there were not enough samples throughout the dataset to compute a correction for that sector/SRAT/SRAR bin. A future development could be to intelligently extrapolate those heatmaps in the SRAR direction, using the theoretically expected roll-off of those patterns.

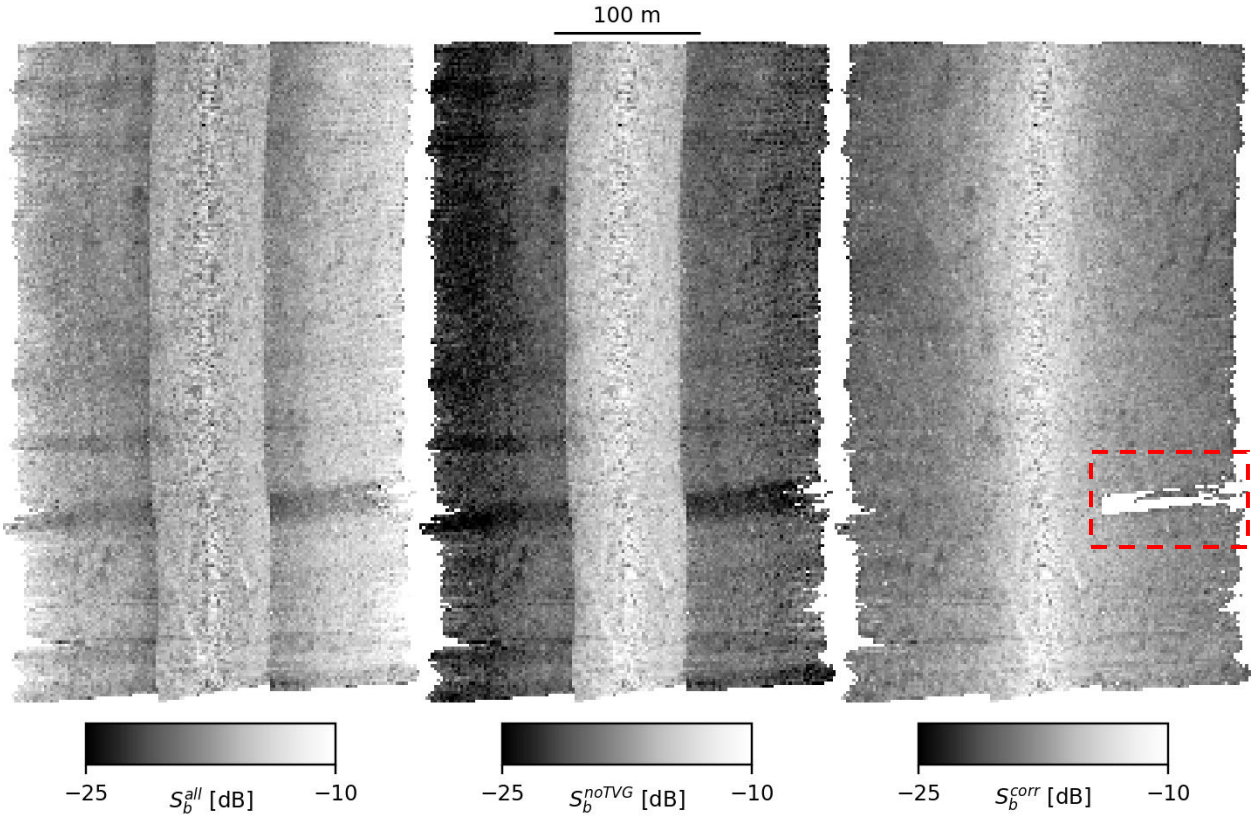

Figure 6.18: Mosaics generated with S_b^{all} (left), S_b^{noTVG} (center), S_b^{corr} (right) for a specific survey line of the dataset under analysis (2m resolution grids). The red dashed box highlights the lack of an available corr due to the associated SRAT/SRAR being outside the correction heatmap range. Dataset under analysis: EM710 / Very Shallow / 70-100 kHz / Dual swath / Shell hash.

6.4. Comparing correction heatmaps for the same sonar/mode but from different reference areas

The correction heatmaps generated for a specific MBES, operating in the same mode, should, in principle, be independent of the reference area used. Hence, to get some sort of repeatability metric for the developed methodology, correction heatmaps generated with data from different reference areas, using the same MBES and mode, are compared.

Throughout the following subsections, the Shell hash and Cobbles reference areas will be used to generate different correction heatmaps for the EM710 operating in Very Shallow mode at

70-100 kHz and the EM2040P in Shallow mode at 200 kHz, both using dual swath. Then, a difference heatmap is obtained by subtracting one correction heatmap from the other, resulting in each pixel corresponding to the correction difference for each sector/SRAT/SRAT bin.

6.4.1. EM710 / Very Shallow / 70-100 kHz

The difference heatmap computed from the EM710 / Very Shallow / 70-100 kHz / Dual swath correction heatmaps generated with the Shell hash and Cobbles reference areas (Figure 6.13 and Figure 5.18, respectively) is presented in Figure 6.19.

The difference between heatmaps ranges approximately between 0 and 2 dB, with the mean difference being ~1 dB. Departures from this mean difference are observed in the outer sectors, in SRATs beyond 60°. One factor that might contribute to this is that SIS uses the same cumulative attenuation coefficient (α) for every beam in a transmit sector, resulting in a slant range dependent bias. Additionally, as an attempt to establish how wrong α would have to be to produce the observed range dependent bias, $2\alpha_{error}R$ was modeled for different attenuation coefficient biases (α_{error}), as depicted in Figure 6.20. Considering α_{error} = -5 dB/km in a flat seafloor with a depth of 50 m (as for the Shell hash area), mitigates the range dependent bias that affected the difference heatmap (Figure 6.21). Obviously, α_{error} must be understood as the combined attenuation coefficient bias for the two reference sites. However, a -5 dB/km error, especially for the involved frequencies (~70-100 kHz), would result from a gross misevaluation of the environmental conditions (T and S), which does not seem to be likely: assuming T = 11°C, S = 30 PSU, depth = 50 m; an α_{error} = -5 dB/km would imply a T_{error} = -8°C or a S_{error} = -6 PSU.

In the center sectors, deviations from the mean difference are also identified. These could occur due to the assumptions made while estimating EAC_{all}, namely the considered pulse length

and beamwidths. Given that there are ambiguities in the interpretation of KM's method of deriving the TVG for the .ALL format, this is considered likely.

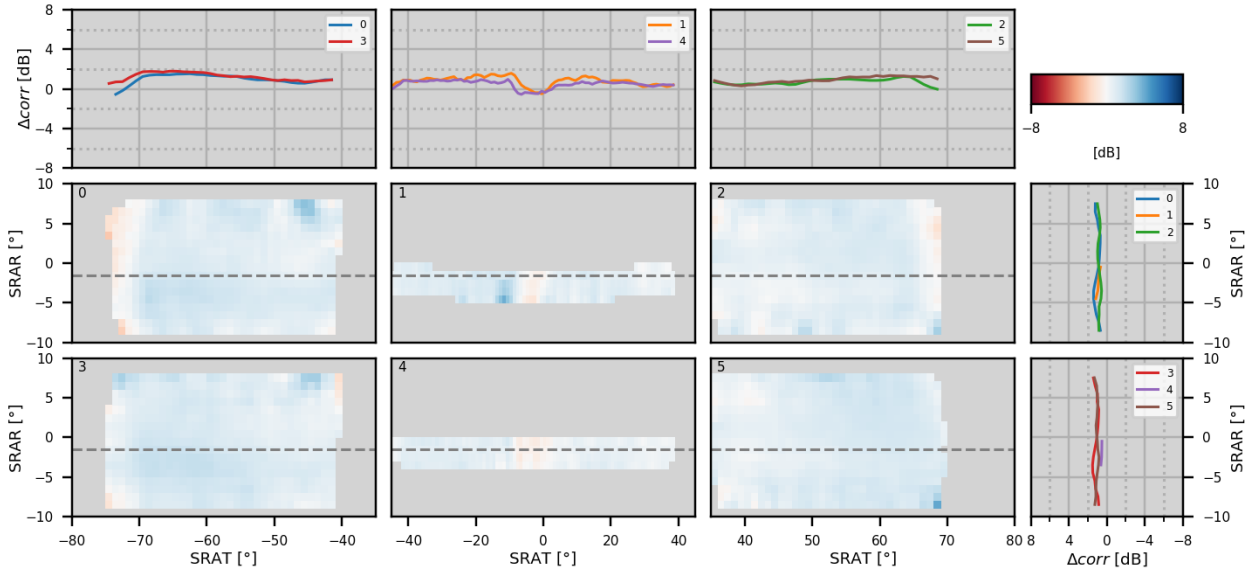

Figure 6.19: Difference heatmap obtained with the EM710 / Very Shallow / 70-100 kHz / Dual swath datasets: Shell hash – Cobbles.

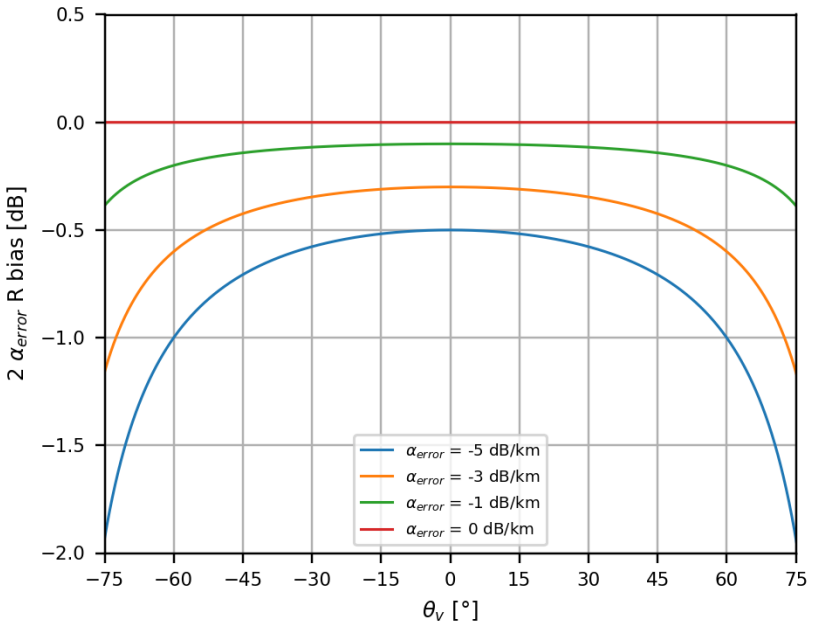

Figure 6.20: Impact of using a attenuation coefficient (α) bias in 2αR, as a function of the local vertically referenced angle (θ_v), considering a flat seafloor and a depth of 50 m.

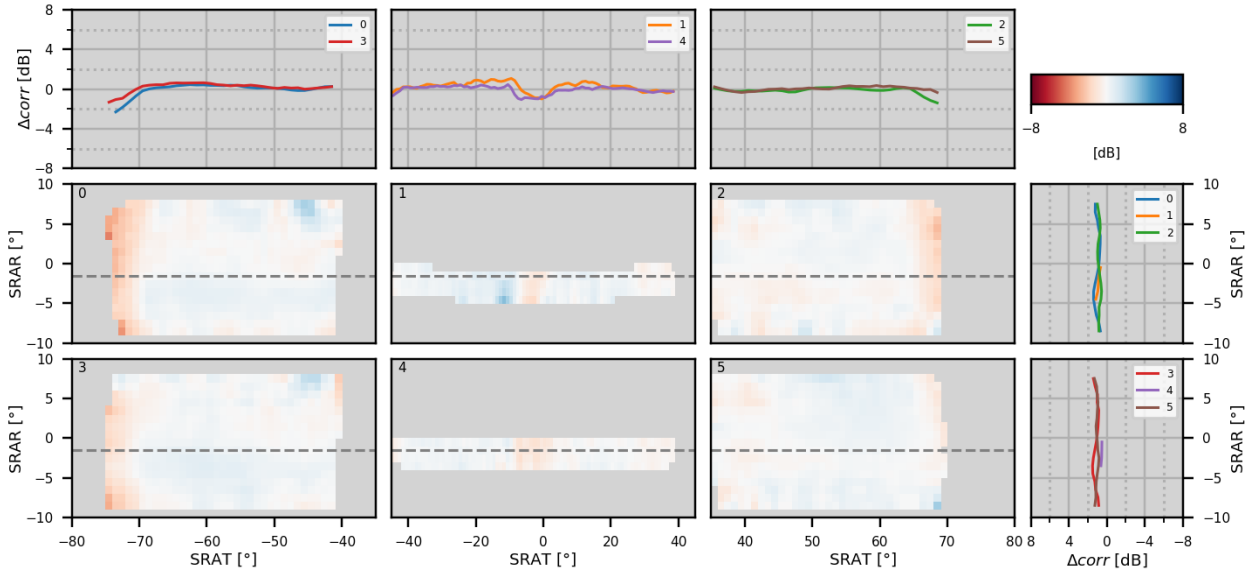

Figure 6.21: Difference heatmap obtained with the EM710 / Very Shallow / 70-100 kHz / Dual swath datasets: Shell hash – Cobbles. A correction of $2\alpha_{error}R$ (α_{error} = -5 dB/Km) was applied to the Shell hash dataset.

Finally, despite all the unresolved systematic biases that might come from applying this dissertation's methodology, it is important to emphasize that the reference ARCs will ultimately determine how good the correction heatmaps will turn out.

6.4.2. EM2040P / Shallow / 200 kHz

Figure 6.22 and Figure 6.23 are the correction heatmaps for the EM2040P / Shallow / 200 kHz / Dual swath, generated with data acquired over the Shell hash and Cobbles reference areas respectively, and Figure 6.24 is the correspondent difference heatmap.

The difference between heatmaps is generally contained within ± ~1 dB, with the mean difference being ~0 dB. In this comparison, the data is in the .KMALL format, meaning that TVG_{kmall} is well understood and, unlike the .ALL format, no assumptions regarding beamwidth or pulse length are required.

Still, and similarly to what is described in the previous subsection, departures from the mean difference (up to ± ~2 dB) are observed for the outer SRATs and near SRAT = 0°. Again, the cause might be related to how absorption is treated (especially considering the now higher frequencies where the short-range attenuation is more significant), as there again seems to be a slight range dependent trend; to how EAC_{imp} is being computed, especially near normal incidence; and/or to how accurate the reference ARCs are.

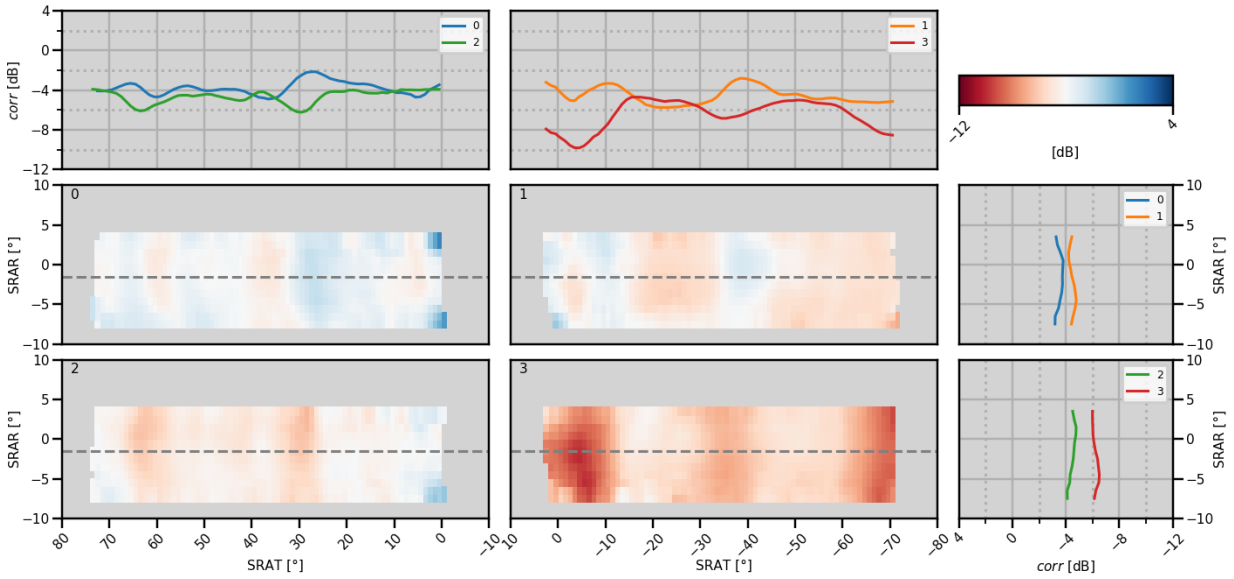

Figure 6.22: The correction heatmap generated with the following dataset: EM2040P / Shallow / 200 kHz / Dual swath / Shell hash.

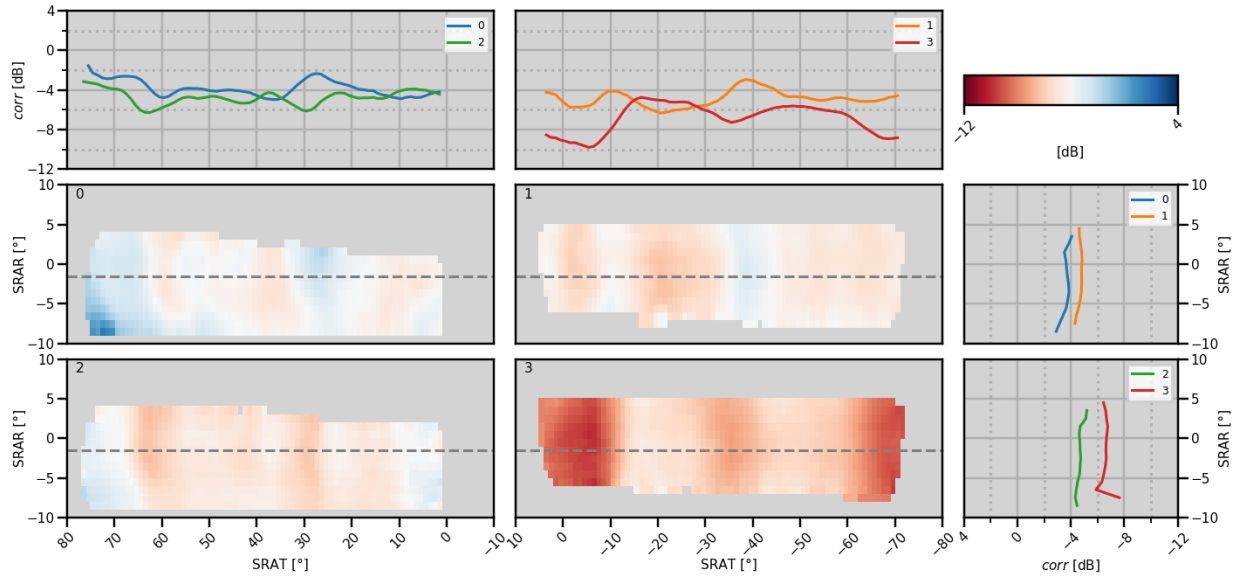

Figure 6.23: The correction heatmap generated with the following dataset: EM2040P / Shallow / 200 kHz / Dual swath / Cobbles.

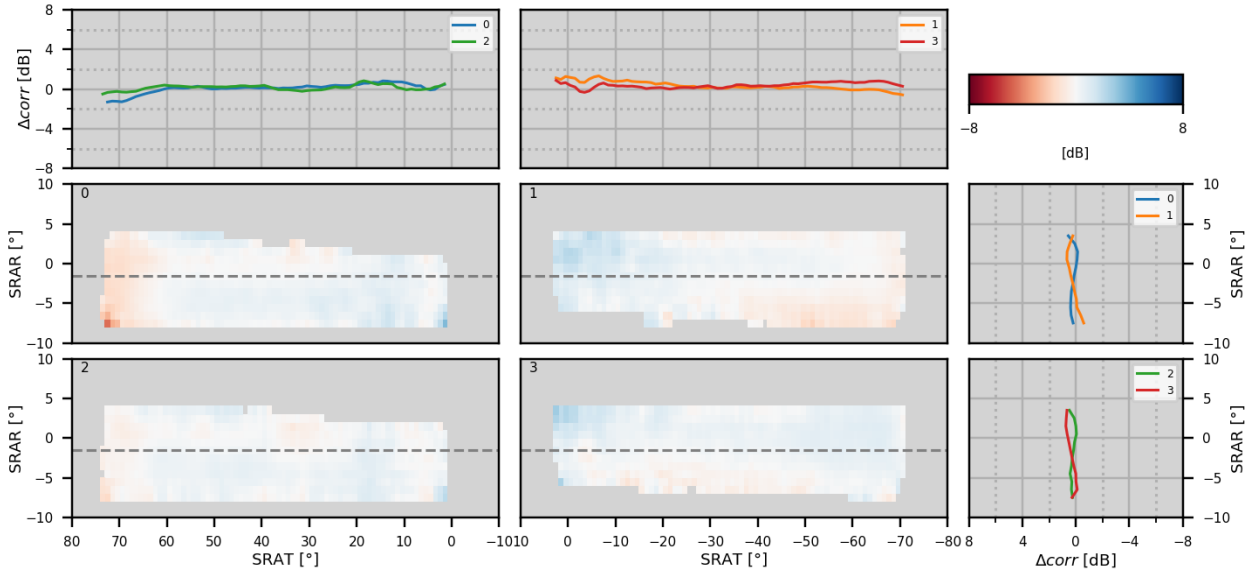

Figure 6.24: Difference heatmap obtained with the EM2040P / Shallow / 200 kHz / Dual swath datasets: Shell hash – Cobbles.

6.4.3. EM712 / Very Shallow / 70-100 kHz

As a third example, the correction heatmaps generated from the datasets acquired with the EM712 / Very Shallow / 70-100 kHz / Dual swath over the Shell hash and Cobbles reference areas are respectively illustrated in Figure 6.25 and Figure 6.26, and their difference in Figure 6.27.

The difference between heatmaps is generally contained within ± ~2 dB, and the mean difference is ~0 dB. The difference heatmap again suggests a range dependent bias, especially visible in the outer sectors, which might indicate some attenuation coefficient bias.

At near normal incidence geometries, there is a significant departure from the mean difference. Since the data is in the .KMALL format, it is unlikely that the TVG is not being correctly removed. As an alternate explanation, issues associated with the computation of EAC_{imp} might be responsible for it: biases in the grazing angles, effective pulse length and/or beamwidths.

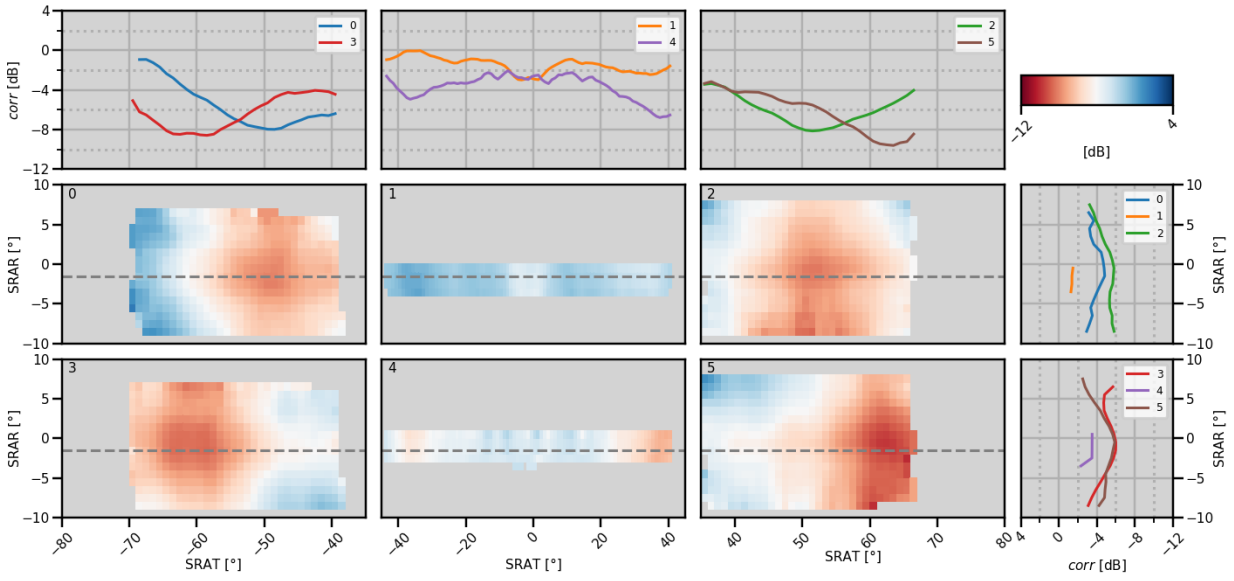

Figure 6.25: The correction heatmap generated with the following dataset: EM712 / Very Shallow / 70-100 kHz / Dual swath / Shell hash.

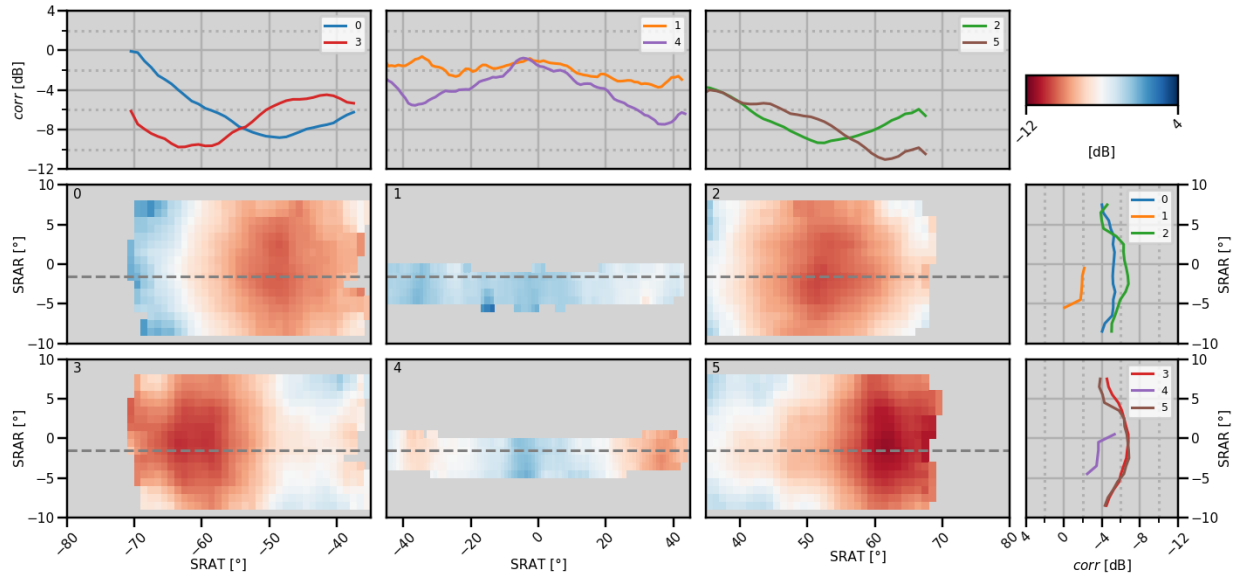

Figure 6.26: The correction heatmap generated with the following dataset: EM712 / Very Shallow / 70-100 kHz / Dual swath / Cobbles.

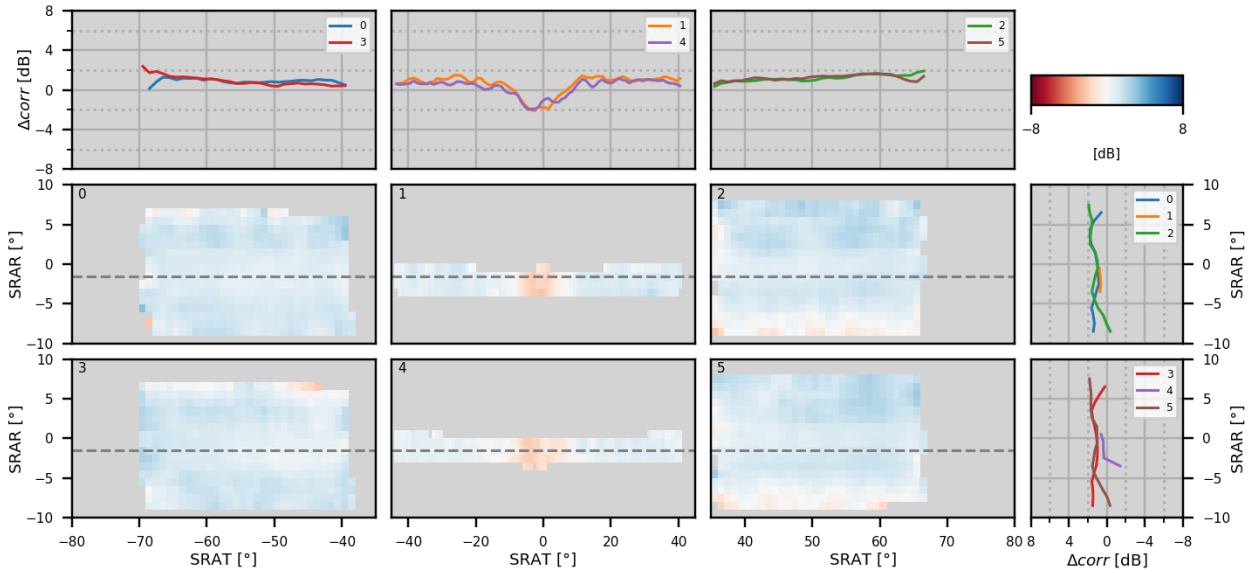

Figure 6.27: Difference heatmap obtained with the EM712 / Very Shallow / 70-100 kHz / Dual swath datasets: Shell hash – Cobbles.

6.5. KMALL format SL and M models

By analyzing the correction heatmaps depicted in Figure 6.22 and Figure 6.23 regarding EM2040P / Shallow / 200 kHz / Dual swath datasets, the corrections seem to be independent of the SRAR, unlike the observed for the EM710 & EM712 / Very Shallow / 70-100 kHz / Dual swath datasets. This remark suggests the applied SL and M models are accounting for this effect. Fortunately, the .KMALL format stores the used models, which can be presented in their own heatmap and thus this hypothesis can be tested.

Figure 6.28 illustrates the SL model heatmap, suggesting that the modeled SL is SRAT dependent, but independent of SRAR. On the other hand, the M model heatmap (Figure 6.29) suggests M is dependent on both SRAT and SRAR, explaining why the resulting EM2040P correction heatmaps seem to be independent of SRAR variations.

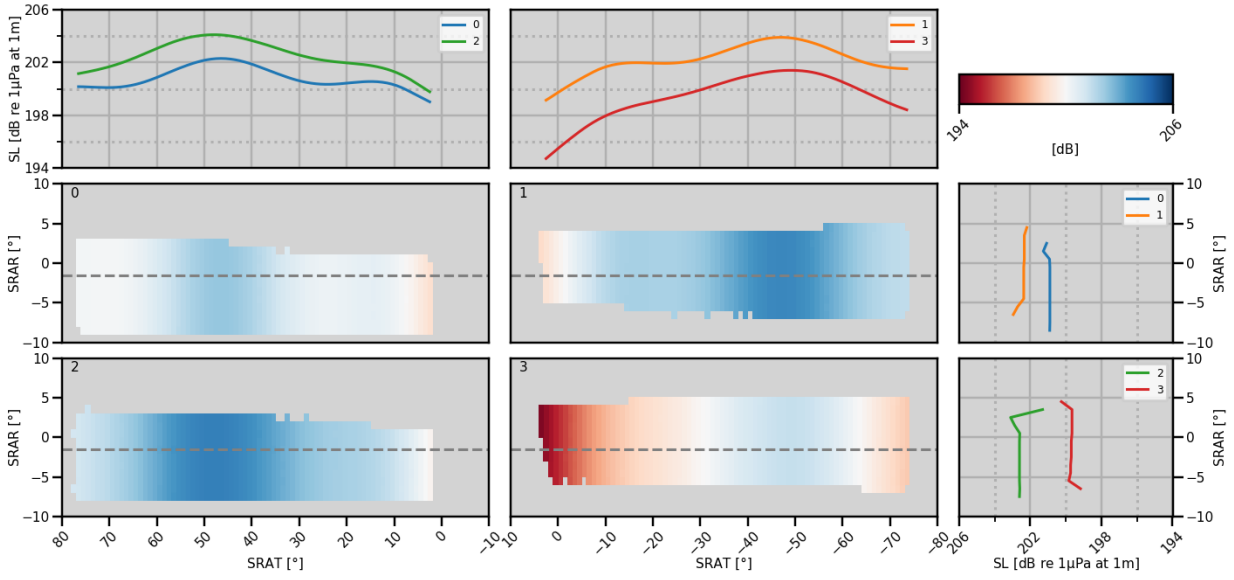

Figure 6.28: SL heatmap obtained from the EM2040P / Shallow / 200 kHz / Dual swath / Cobbles dataset.

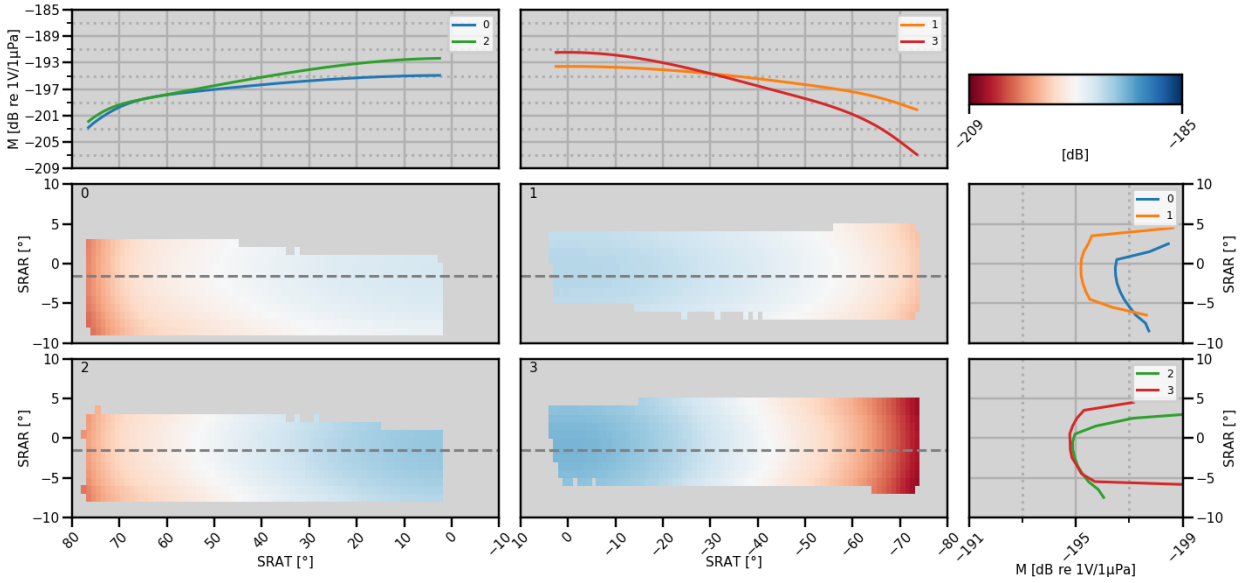

Figure 6.29: M heatmap obtained from the EM2040P / Shallow / 200 kHz / Dual swath / Cobbles dataset.

Although it seems the EM2040P M model clearly does have a SRAR component, not every KM multi-sector MBES operating with the .KMALL format includes such complete models of M. Figure 6.30 and Figure 6.31 show the EM712 / Very Shallow / 70-100 kHz / Dual swath SL and M model heatmaps, revealing that, unlike the EM2040P M model, the modeled receiver sensitivity does not respond to changes in SRAR.

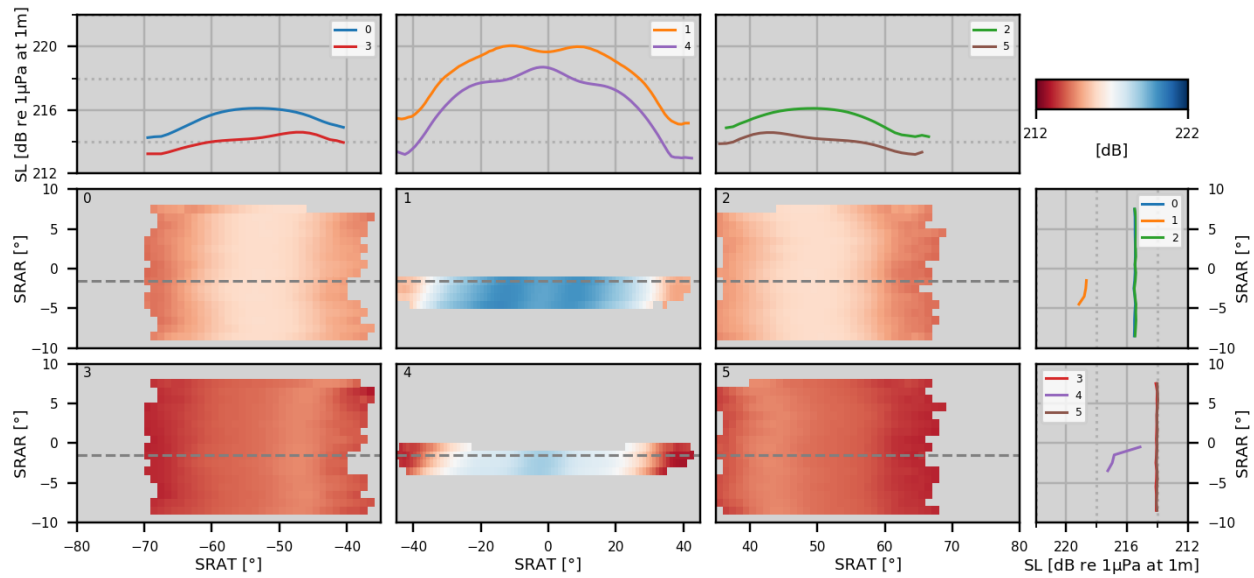

Figure 6.30: SL heatmap obtained with the EM712 / Very Shallow / 70-100 kHz / Dual swath / Cobbles dataset.

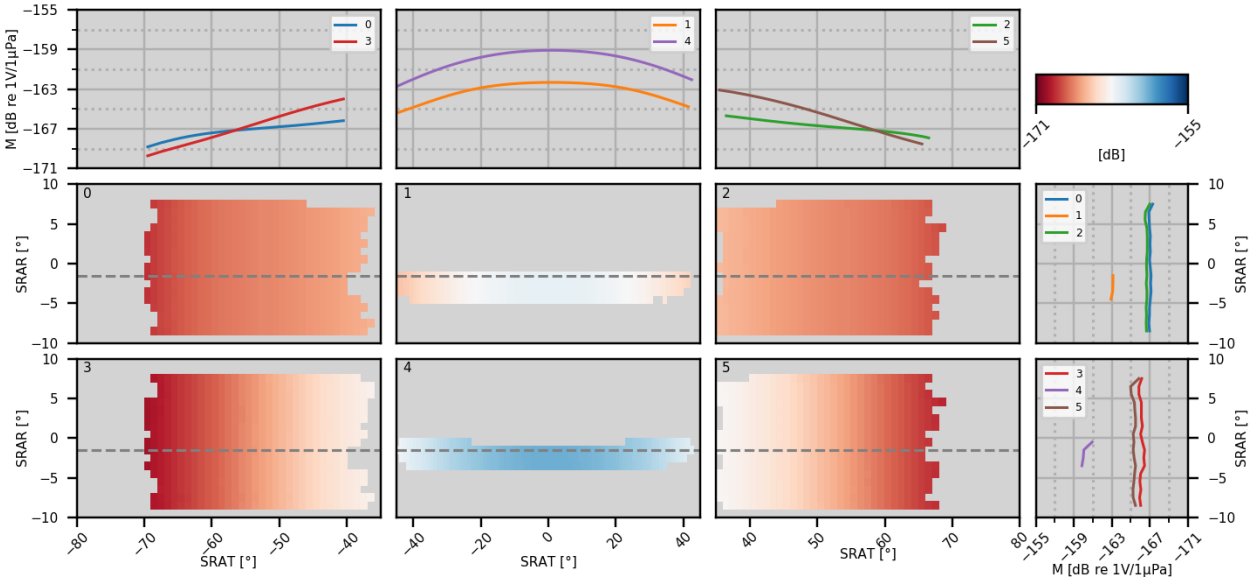

Figure 6.31: M heatmap obtained with the EM712 / Very Shallow / 70-100 kHz / Dual swath / Cobbles dataset.

With the goal of trying to estimate the equivalent width of the transmit arrays used by an EM712, the KM SL model used in the Very Shallow mode was compared to the beam pattern of unshaded continuous line arrays with different widths (Figure 6.32). Perhaps unsurprisingly, the

unshaded line array model does not explain the used KM SL model, especially in the center sectors. The fact that a drop in SL is observed in the middle of the center sector might perhaps suggest that it is being deliberately defocused to reduce the near normal echo level (as was reported for the old Sea Beam 2100 transmitter (L-3 Communications SeaBeam Instruments, 2000)).

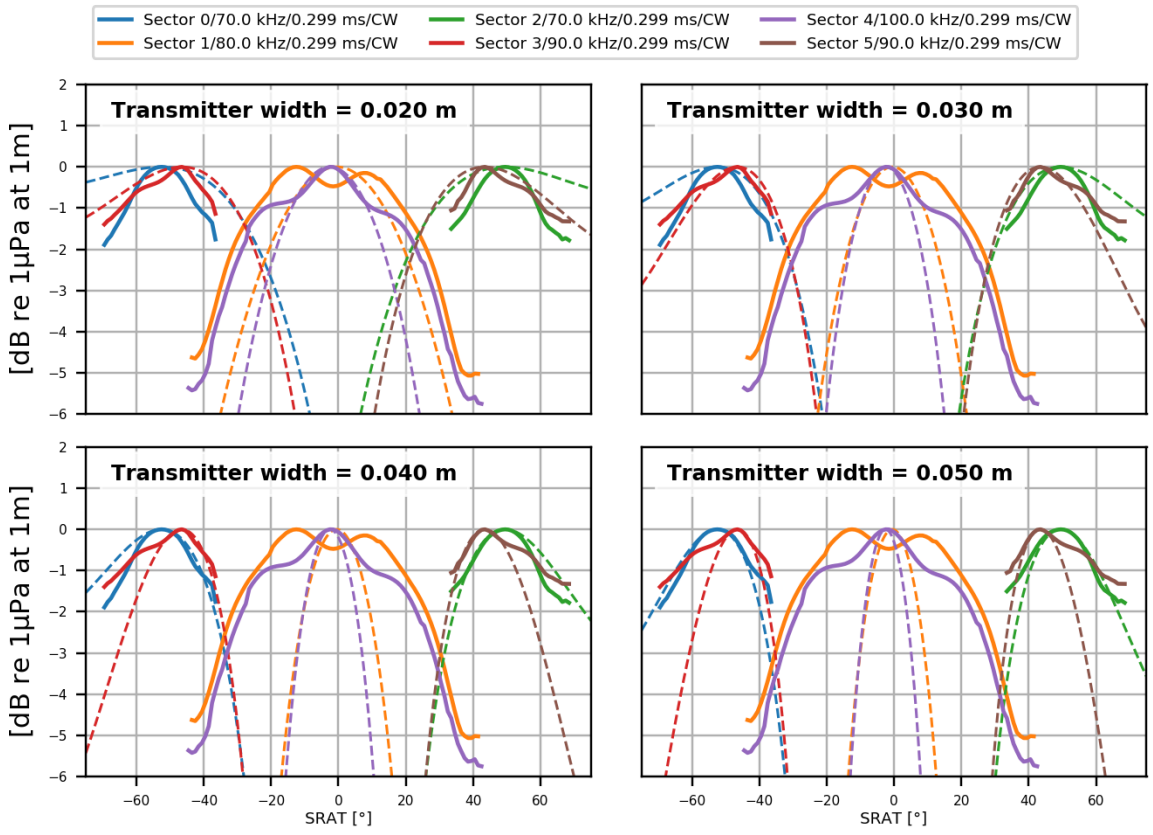

Figure 6.32: Comparing KM SL model of an EM712 operating in Very Shallow mode (solid lines) with the beam pattern of steered unshaded line arrays with different widths (dashed lines).

6.6. Establishing a reference area with a calibrated MBES rather than with a reference SBES

The original approach of Guimarães (2020) was to utilize the calibrated SBES as reference. That approach implies however, that these have to be available each time to be deployed in a suitable area. An alternate approach, however, could be that subsequent to one SBES reference at a specific location, MBES that are calibrated there could then carry that calibration to other sites.

To test the feasibility of this approach, in April 2022, some of the reference areas established by Guimarães (2020) were resurveyed with an uncalibrated EM712 MBES, as depicted in Table 6.1. Using the reference multispectral ARCs from 2019, correction heatmaps were generated for the EM712 operating in various modes.

As explained above, in principle, this now-calibrated MBES is capable of acquiring absolutely referenced S_b in other locations, ultimately allowing the possibility of generating equivalent reference ARCs for that new location. Note that, unlike the original SBES reference covering a broad range of frequencies, the new reference is just for the specific subset of frequencies at which the transferring sonar operates. These new reference datasets can in turn be used to calibrate subsequent sonars operating at the same frequencies. In practice, many national agencies operate the same systems and thus only the same range of frequencies needs to be established.

To demonstrate the viability of this approach, and with the goal of establishing a more accessible reference area that would be better suited for larger federal platforms from both US and Canadian agencies to operate without having to cross borders, a section of the US-Canada border in the eastern end of the Strait of Juan de Fuca, between Victoria and Port Angeles, was surveyed (Figure 6.33). Conveniently, this transect is in a more suitable depth range for an EM712 (~100m, rather than the ~25-50 m of the original sites), avoids the shipping lanes and is located in protected

waters, where oceanographic conditions are often favorable for surveying (well mixed water column).

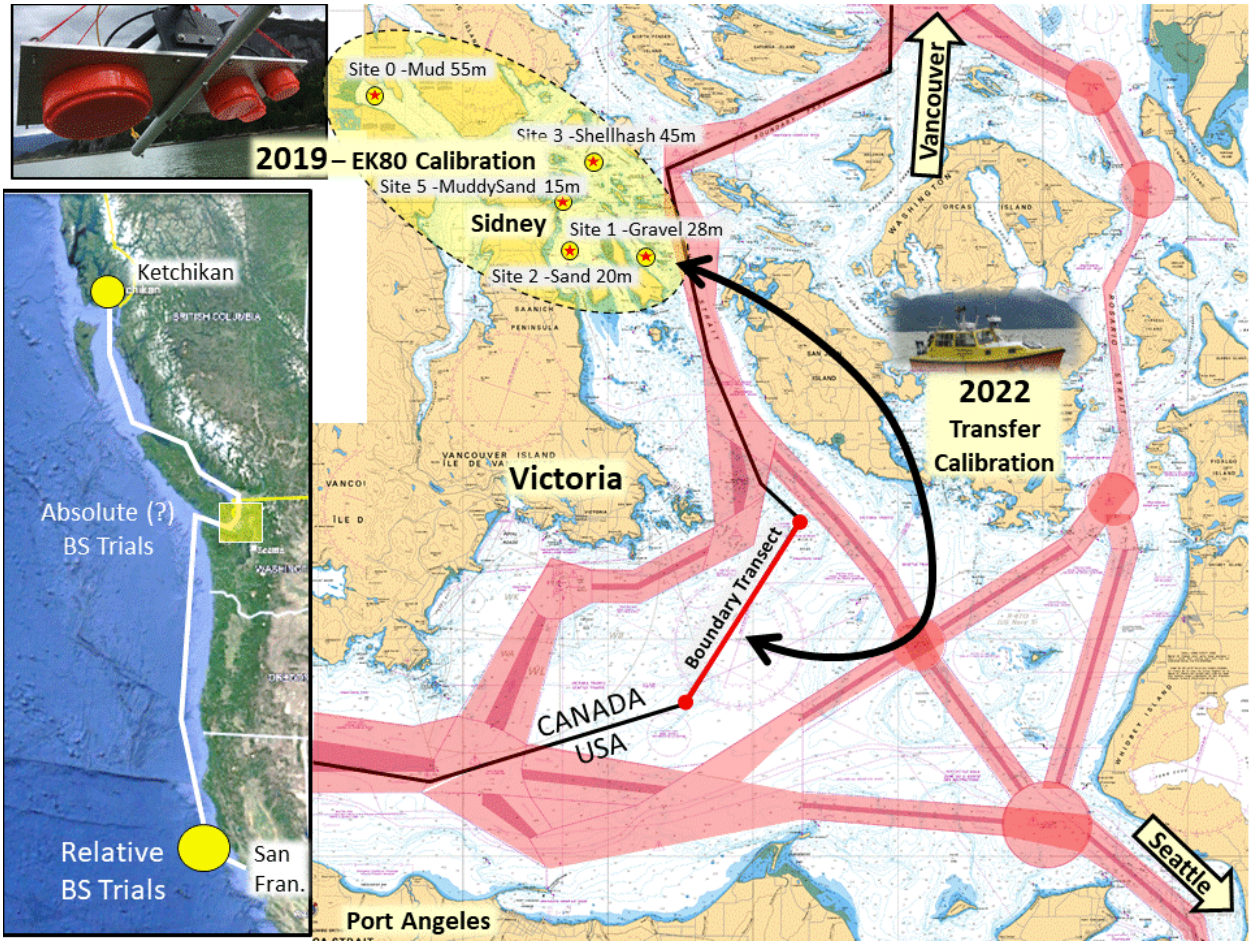

Figure 6.33: Establishing a new reference area in the US-Canada border. The inset on the left suggests the usage of this reference area by a hydrographic vessel transiting from San Francisco, CA to Ketchikan, AK, using the inner passage. From Hughes Clarke (2022).

In this transect, a ~ 3.5 km section presents a smooth bathymetry – depths between 100 and 115 m -, relatively uniform and high S_b, without any discernible specular component, suggesting that the seabed consists of washed cobbles and gravels (Hewitt & Mosher, 2001), which typically produce a Lambertian angular dependence. Figure 6.36 provides a representation of the bottom backscatter strength and the relief.

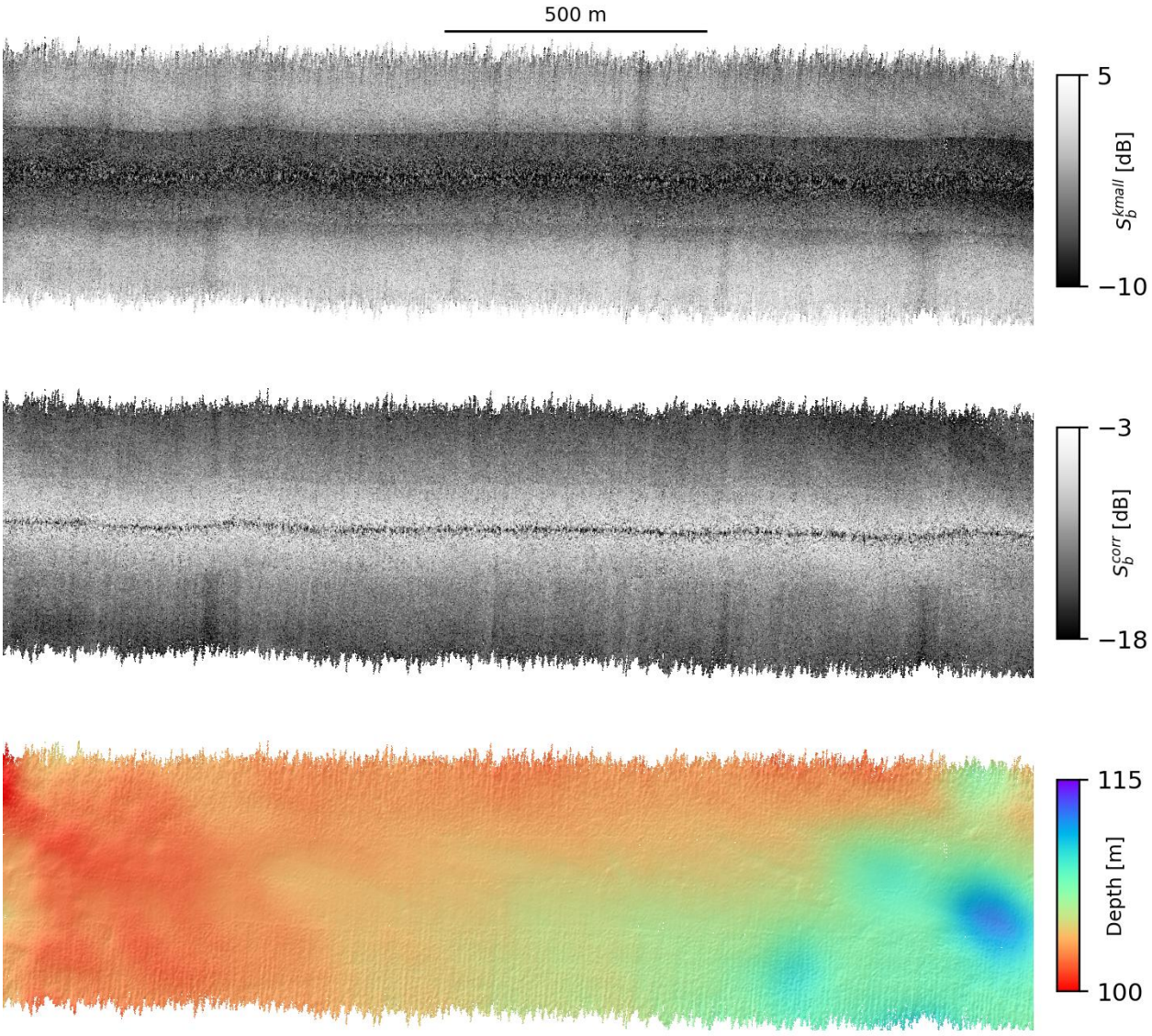

Figure 6.34: S_b^{kmall} mosaic (top), S_b^{corr} mosaic (center) and depth DTM (bottom). All grids with 2 m resolution. Dataset under analysis: EM712 / Very Shallow / 70-100 kHz / Dual swath / US-Canada border.

Considering the depth range is best suited for the EM712 Very Shallow and Shallow modes, Figure 6.35 presents the respective ARCs.

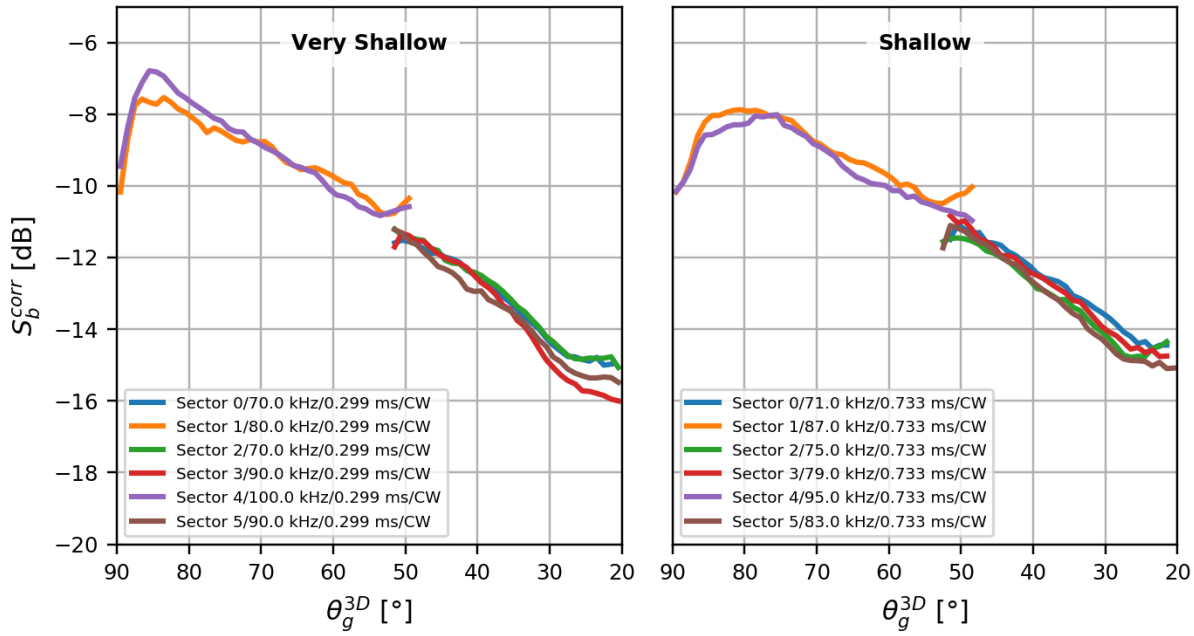

Figure 6.35: US-Canada border transect S_b ARCs acquired with a calibrated EM712 operating on Very Shallow mode (left) and Shallow mode (right) (both 70-100 kHz / Dual swath).

For the grazing angles between 20 and 80°, the ARCs from the two depth modes agree fairly well, which is to be expected since the frequencies used are no more than 11 kHz apart.

For the higher grazing angles, the two ARCs present more significant differences and both display a drop in S_b near normal incidence, where a maximum response is expected. Nonetheless, both ARCs present an identical S_b at normal incidence. The drop in S_b at nadir, however, is not physically realistic and suggests an imperfect near-nadir data calibration transfer from the original site to this area.

6.6.1. Investigating the ARCs anomalies

The only substantial difference between the EM712 Very Shallow and Shallow modes is the used pulse length, which only impacts the improved ensonified area correction (EAC_{imp})

computation. Equations 5.25, 2.4 and 2.5 imply that if there is any bias in the grazing angle calculations, its effect on EAC_{imp} will also depend on the pulse length. Figure 6.36 shows that the same grazing angle error (true grazing angle – biased grazing angle) has a bigger impact on the computed EAC_{imp} when smaller effective pulse lengths are used.

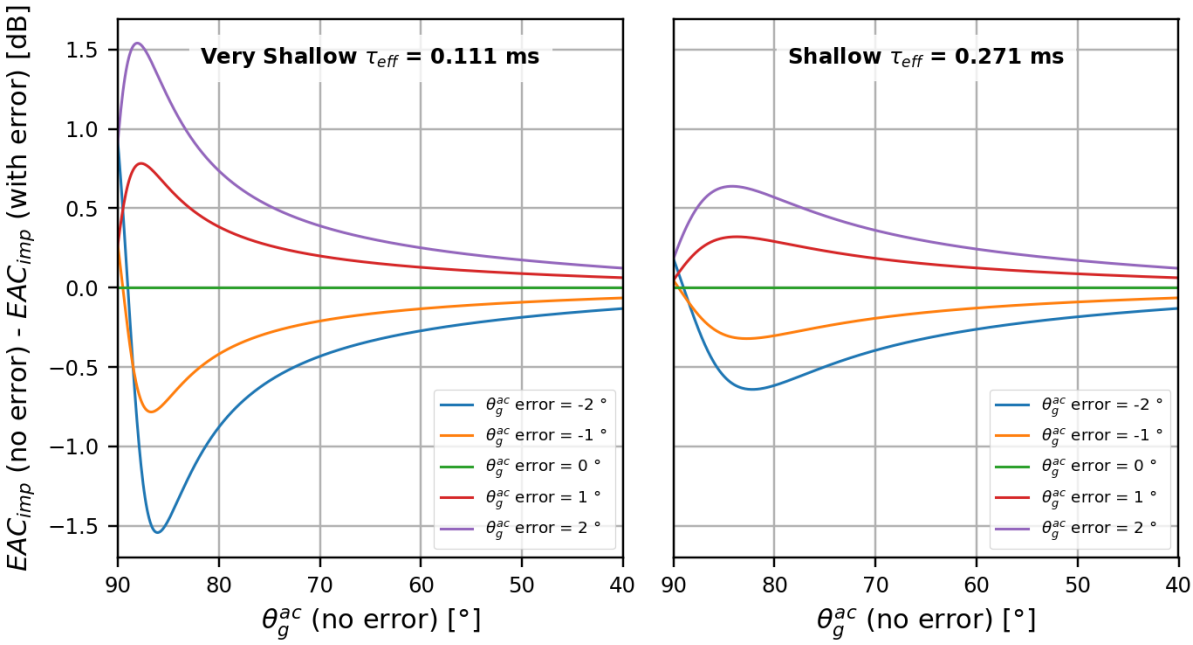

Figure 6.36: Impact of an across-track grazing angle bias on the EAC_{imp} computation. Left: EM712 Very Shallow mode effective pulse length; Right: EM712 Shallow mode pulse length.

Based on the area calculations shown in Figure 6.36, the anomalies in the ARCs presented in Figure 6.35 – the disparity between modes and the near nadir S_b dip - can be partially explained by a grazing angle bias. Furthermore, for the oblique grazing angles, the ARCs appear to have no issue which might indicate that the beamwidth limited ensonified area component might have some problem such as a bias on the beamwidths or the model itself not being good enough.

On top of that, it is also possible that the original reference multispectral ARCs from which the correction heatmaps were generated lack some accuracy, especially at near normal incidence, as explained in Section 6.4.

7. CONCLUSIONS

For a multi-sector MBES operating under a determined set of parameters (a specific mode), a two-dimensional array of correctors was derived for each transmit sector (the correction heatmap), providing estimates of the necessary beam pattern calibration, as a function of across- and along-track sonar referenced angles (SRAT and SRAR) to obtain absolute referenced S_b values. In principle, considering a homogenous area, if the correction heatmap is applied to the original data, the corrected output will match the associated reference angular response curve.

To produce the correction heatmaps, uncalibrated data must be compared to a reference angular response curve spanning through a wide range of grazing angles and, obviously, covering at least the used acoustic frequencies.

Subsequently, for each uncalibrated S_b estimate, a series of preliminary operations must be conducted. It is necessary to determine the grazing angle, compute the ensonified area (accounting for the along and across-track relief) and, of course, to estimate and reduce the manufacturer's applied Time Varying Gain. Notably, the .KMALL data format (Kongsberg Maritime) discloses the manufacturer's used TVG, unlike the previous .ALL format, where certain assumptions had to be made (used ensonified area model, pulse length and beamwidths), as the existing documentation does not define it entirely. Concurrently, using the geometry first proposed by Hiroji (2016), each S_b estimate is mapped according to its sonar relative angles.

The data is then binned by sector and sonar relative angles, allowing for computation of a mean S_b value for each bin. Simultaneously, a representative grazing angle is determined, allowing computation of the difference between the mean S_b value and the reference angular response curve, thus providing the corrector for each permutation of sector and sonar relative angles.

The developed technique was used with data collected by Guimarães (2020) in British Columbia, Canada in 2019, which included multispectral angular response curves for several homogeneous reference areas, acquired with calibrated split-beam echosounders, and uncalibrated data from an EM710 and an EM2040P, collected with the MBES operating at several depth modes. In 2022, a subset of those reference areas were resurveyed with two other MBES, an EM712 and an EM2040C, incrementing the number of datasets to which this methodology could be applied.

From the several available reference areas, the Shell hash and Cobbles areas were selected to use with this technique, as their angular response curve presented a negligible specular component, which eases the estimation of S_b at near normal incidence. Taking into account the depth of the considered reference areas (Shell hash: ~45 m; Cobbles: ~25 m) and also the noise of their angular response curves at certain frequencies, the following MBES/mode/frequencies combinations were considered to generate correction heatmaps: EM710 / Very Shallow / 70-100 kHz, EM712 / Very Shallow / 70-100 kHz and EM2040P / Shallow / 200 kHz. It is important to highlight that the generated corrections operate on top of the manufacturer's built-in estimates of the system's Source Level and Receiver Sensitivity, which the .KMALL data format records, unlike .ALL. Careful inspection of these models suggests that, for the EM2040P, the along-track receiver sensitivity variability is accounted for, which is especially important as that MBES can perform yaw stabilization. Remarkably, that same dependence was not identified for the EM712, which would also benefit from it as it is too a yaw-stabilized system.

To estimate how repeatable the generated correction heatmaps are, the same MBES, operating in the same mode, was used to collect data from the two mentioned reference areas and generate the respective heatmaps, which should be independent of the acquisition location. The

differences between heatmaps were generally within ±~ 2dB, suggesting that the developed technique is providing an adequate set of correctors.

Assuming this technique provides acceptable results, a pre-calibrated MBES can be used to survey a different location and establish another reference area. Thus, for the frequencies associated to the modes for which correction heatmaps are available, absolutely referenced angular response curves should be retrievable and be used to calibrate subsequent sonars that use the same frequencies. Under that scope, an attempt was made to establish a 2 nautical miles reference transect at the US-Canada border, in the eastern end of the Strait of Juan de Fuca, between Victoria and Port Angeles. This location presents depths ~100 m and relatively homogeneous and high S_b, apparently with no significant specular component. A pre-calibrated EM712, operating in Very Shallow and Shallow mode, was used to derive the angular response curves, which should agree, as both modes use similar frequencies. The retrieved ARCs were identical up to ~10 ° from normal incidence. However, from there to normal incidence, both curves presented a suspicious drop in S_b, which might be caused by a combination of the following complications: biases in the used grazing angles, beamwidths and effective pulse lengths and the actual model used to estimate the ensonified area.

In the end, the goal of establishing a new reference area by using a pre-calibrated MBES was only partially achieved as some outstanding complications surfaced and still lack a thorough examination.

7.1. Recommendations for further research

Under the scope of the current implementation of the proposed technique, some opportunities for improvement were identified and could be addressed in future research:

- Refraction is neglected in the estimation of the grazing angle and the SRAR. The beam direction at the seafloor is estimated by establishing a vector between the sounding and the transmit array at the time of transmission. The ensonified area model used is considerably sensitive to small grazing angle biases when the transition from a mainly pulse length limited regime to a mainly beamwidth limited regime occurs. To adequately solve this, the launching direction of the beam at the array would have to be estimated by intersecting the two non-concentric transmit and receive acoustic cones. As Kongsberg Maritime already solves the cone intersection (and the subsequent raytracing) in real time, the inclusion of a data field containing the beam vector direction when it intersects the seafloor would be a helpful addition.
- The correction heatmaps were generated on top of the manufacturer's estimates for Source Level and Receiver Sensitivity. It is unknown how these are applied to each beam and, most likely, are not employed as a function of SRAT and SRAR. Therefore, at least for the data in the .KMALL format, removing these estimates before generating the correction heatmaps would output better results. For the data in the .ALL format, as these estimates are not recorded, this operation cannot be performed. Still, to have a better understanding of what assumptions are being made, the same MBES could be used to run a specific set of lines twice, one outputting data in the .ALL format and another in the .KMALL format. Since the used hardware would be the same, the difference between the collected datasets

would, in principle, allow determination of the manufacturer's estimates for the Source Level and Receiver Sensitivity used in the .ALL format.

- Contrary to Kongsberg's claims, it was assumed that the EM712 does not vertically stabilize its transmit sectors. It would be interesting to see what results would emerge by considering that their transmit sectors are steered across-track to compensate for the roll.
- To obtain reliable S_b estimates, it is essential to correctly characterize the acoustic losses throughout the water column. The current work accepted the real-time software solution, which generates a single attenuation coefficient per transmit sector. However, in the presence of steep bathymetry, this solution might not be the best and contribute to the appearance of range dependent biases in the collected datasets. Thus, it would be advisable to compute the attenuation coefficients on a per beam basis.
- Data collection over the reference area followed a star pattern survey design, allowing to simultaneously assess the S_b azimuth dependency and increase the amount of acquired data. However, the usage of this pattern led to some operational complications. Steaming over the bubble field present in the wake of a previous line would often result in collecting some invalid data. Moreover, and perhaps more importantly, as the vessel usually turned in the same direction from one line to the next, and as the yaw stabilization reflects the recent history of a corner, all lines ended up with a one-sided yaw stabilization (e.g., the starboard sector would always be steered forward while the port sector would always be steered aft). Consequently, the generated correction heatmap would not cover the entire SRAT/SRAR feature space. Alternating the direction of turns at the end of each line would possibly promote the generation of a more complete correction heatmap. Another way of dealing with the limited reach of the correction heatmap is to attempt to model the along-track

receiver sensitivity beam pattern, enabling its extrapolation to larger SRAR, associated to heavy yaw stabilization.

- Besides comparing correction heatmaps from the same system (and mode) generated from datasets collected in different reference areas, no attempt has been made to assess the repeatability of the acquired correctors. Future research could focus on determining the uncertainty associated to the absolutely referenced S_b obtained through the application of the proposed technique.
- Finally, the obtained correction heatmaps are obtained by comparing the uncalibrated data with the reference multispectral angular response curves. Therefore, every effort put into getting the best reference data will contribute to generate a more reliable set of correctors.

LIST OF REFERENCES

Amiri-Simkooei, A., Snellen, M., & Simons, D. G. (2009). Riverbed sediment classification using multi-beam echo-sounder backscatter data. *The Journal of the Acoustical Society of America*, *126*(4), 1724. https://doi.org/10.1121/1.3205397

Anderson, J. T., Holliday, D. V., Kloser, R., Reid, D., Simard, Y., Brown, C. J., Chapman, R., Coggan, R., Kieser, R., Michaels, W. L., Orlowski, A., Preston, J., Simmonds, J., & Stepnowski, A. (2007). *Acoustic seabed classification of marine physical and biological landscapes* (ICES Cooperative Research Report No. 286). International Council for the Exploration of the Sea (ICES). https://ices-library.figshare.com/articles/_/18624206

Anderson, J. T., Van Holliday, D., Kloser, R., Reid, D. G., & Simard, Y. (2008). Acoustic seabed classification: Current practice and future directions. *ICES Journal of Marine Science*, *65*(6), 1004–1011. https://doi.org/10.1093/icesjms/fsn061

Anderson, T. J., Cochrane, G. R., Roberts, D. A., Chezar, H., & Hatcher, G. (2007). A rapid method to characterize seabed habitats and associated macro-organisms. *Special Paper - Geological Association of Canada*, *47*, 71–79. USGS Publications Warehouse.

APL-UW. (2014). *APL-UW High-Frequency Ocean Environmental Acoustic Models Handbook* (APL-UW TR No. 9407). Applied Physics Laboratory - University of Washington.

Augustin, J. M., Le Suave, R., Lurton, X., Voisset, M., Dugelay, S., & Satra, C. (1996). Contribution of the multibeam acoustic imagery to the exploration of the sea-bottom. *Marine Geophysical Researches*, *18*(2–4), 459–486. https://doi.org/10.1007/BF00286090

Augustin, J. M., & Lurton, X. (2005). Image amplitude calibration and processing for seafloor mapping sonars. *Europe Oceans 2005*, 698-701 Vol. 1. https://doi.org/10.1109/OCEANSE.2005.1511799

Boehme, H., Chotiros, N. P., Rolleigh, L. D., Pitt, S. P., Garcia, A. L., Goldsberry, T. G., & Lamb, R. A. (1985). Acoustic backscattering at low grazing angles from the ocean bottom. Part I. Bottom backscattering strength. *The Journal of the Acoustical Society of America*, *77*(3), 962–974. https://doi.org/10.1121/1.392064

Brown, C. J., Smith, S. J., Lawton, P., & Anderson, J. T. (2011). Benthic habitat mapping: A review of progress towards improved understanding of the spatial ecology of the seafloor using acoustic techniques. *Estuarine, Coastal and Shelf Science*, *92*(3), 502–520. https://doi.org/10.1016/j.ecss.2011.02.007

Carvalho, R. (2012). *Proper environmental reduction for attenuation in multi-sector sonars* [Master's Thesis, University of New Brunswick]. https://unbscholar.lib.unb.ca/islandora/object/unbscholar%3A8762/datastream/PDF/download/citation.pdf

Chu, D., Foote, K. G., & Hufnagle, L. C. (2002). Measurement of multibeam sonar directivity patterns. *Oceans '02 MTS/IEEE*, 1411–1414. https://doi.org/10.1109/OCEANS.2002.1191844

Chu, D., Foote, K. G., Hufnagle, L. C., Hammar, T. R., Liberatore, S. P., Baldwin, K. C., Mayer, L. A., & McLeod, A. (2003). Calibrating a 90-kHz multibeam sonar. *Oceans 2003. Celebrating the Past ... Teaming Toward the Future (IEEE Cat. No.03CH37492)*, 1633-1636 Vol.3. https://doi.org/10.1109/OCEANS.2003.178119

Cochrane, N. A., Li, Y., & Melvin, G. D. (2003). Quantification of a multibeam sonar for fisheries assessment applications. *The Journal of the Acoustical Society of America*, *114*(2), 745–758. https://doi.org/10.1121/1.1587151

de Moustier, C. (1986). Beyond bathymetry: Mapping acoustic backscattering from the deep seafloor with Sea Beam. *The Journal of the Acoustical Society of America*, *79*(2), 316–331. https://doi.org/10.1121/1.393570

Demer, D. A., Berger, L., Bernasconi, M., Bethke, E., Boswell, K., Chu, D., Domokos, R., Dunford, A., Fassler, S., Gauthier, S., & et al. (2015). *Calibration of acoustic instruments* (ICES Cooperative Research Report No. 326; p. 130). International Council for the Exploration of the Sea (ICES). https://ices-library.figshare.com/articles/_/19056617

Eleftherakis, D., Berger, L., Le Bouffant, N., Pacault, A., Augustin, J.-M., & Lurton, X. (2018). Backscatter calibration of high-frequency multibeam echosounder using a reference single-beam system, on natural seafloor. *Marine Geophysical Research*, *39*(1–2), 55–73. https://doi.org/10.1007/s11001-018-9348-5

Fezzani, R., & Berger, L. (2018). Analysis of calibrated seafloor backscatter for habitat classification methodology and case study of 158 spots in the Bay of Biscay and Celtic Sea. *Marine Geophysical Research*, *39*(1–2), 169–181. https://doi.org/10.1007/s11001-018-9342-y

Fonseca, L., Lurton, X., Fezzani, R., Augustin, J.-M., & Berger, L. (2021). A statistical approach for analyzing and modeling multibeam echosounder backscatter, including the influence of high-amplitude scatterers. *The Journal of the Acoustical Society of America*, *149*(1), 215–228. https://doi.org/10.1121/10.0003045

Fonseca, L., & Mayer, L. (2007). Remote estimation of surficial seafloor properties through the application Angular Range Analysis to multibeam sonar data. *Marine Geophysical Researches*, *28*(2), 119–126. https://doi.org/10.1007/s11001-007-9019-4

Foote, K. G., Chu, D., Hammar, T. R., Baldwin, K. C., Mayer, L. A., Hufnagle, L. C., & Jech, J. M. (2005). Protocols for calibrating multibeam sonar. *The Journal of the Acoustical Society of America*, *117*(4), 2013–2027. https://doi.org/10.1121/1.1869073

Foote, K. G., Knudsen, H. P., Vestnes, G., MacLennan, D. N., & Simmonds, E. J. (1987). *Calibration of acoustic instruments for fish density estimation: A practical guide* (ICES Cooperative Research Report No. 144). International Council for the Exploration of the Sea (ICES).

Foveau, A., Vaz, S., Desroy, N., & Kostylev, V. E. (2017). Process-driven and biological characterisation and mapping of seabed habitats sensitive to trawling. *PLOS ONE*, *12*(10), e0184486. https://doi.org/10.1371/journal.pone.0184486

Francois, R. E., & Garrison, G. R. (1982a). Sound absorption based on ocean measurements: Part I: Pure water and magnesium sulfate contributions. *The Journal of the Acoustical Society of America*, *72*(3), 896–907. https://doi.org/10.1121/1.388170

Francois, R. E., & Garrison, G. R. (1982b). Sound absorption based on ocean measurements. Part II: Boric acid contribution and equation for total absorption. *The Journal of the Acoustical Society of America*, *72*(6), 1879–1890. https://doi.org/10.1121/1.388673

Gensane, M. (1989). A statistical study of acoustic signals backscattered from the sea bottom. *IEEE Journal of Oceanic Engineering*, *14*(1), 84–93. https://doi.org/10.1109/48.16818

Guimarães, I. (2020). *Obtaining a reference for calibrating broadband multibeam seabed backscatter* [Master's Thesis, University of New Hampshire]. https://scholars.unh.edu/thesis/1424/

Hamilton, E. L. (1972). Compressional-wave attenuation in marine sediments. *GEOPHYSICS*, *37*(4), 620–646. https://doi.org/10.1190/1.1440287

Hammerstad, E. (2000). *Backscattering and Seabed Image Reflectivity* (p. 5) [EM Technical Note].

Harris, F. J. (1978). On the use of windows for harmonic analysis with the discrete Fourier transform. *Proceedings of the IEEE*, *66*(1), 51–83. https://doi.org/10.1109/PROC.1978.10837

Heaton, J. L. (2014). *Utilizing an extended target for high frequency multi-beam sonar intensity calibration* [Master's Thesis, University of New Hampshire]. https://ccom.unh.edu/sites/default/files/publications/thesis_JHeaton.pdf

Heaton, J. L., Rice, G., & Weber, T. C. (2017). An extended surface target for high-frequency multibeam echo sounder calibration. *The Journal of the Acoustical Society of America*, *141*(4), EL388–EL394. https://doi.org/10.1121/1.4980006

Hellequin, L., Boucher, J.-M., & Lurton, X. (2003). Processing of high-frequency multibeam echo sounder data for seafloor characterization. *IEEE Journal of Oceanic Engineering*, *28*(1), 78–89. https://doi.org/10.1109/JOE.2002.808205

Hellequin, L., Lurton, X., & Augustin, J. M. (1997). Postprocessing and signal corrections for multibeam echosounder images. *Oceans '97. MTS/IEEE Conference Proceedings*, *1*, 23–26. https://doi.org/10.1109/OCEANS.1997.634329

Hewitt, A. T., & Mosher, D. C. (2001). Surficial Geology of the Eastern Juan de Fuca Strait. In *Neotectonics of the eastern Juan de Fuca Strait; a digital geological and geophysical atlas.*

Geological Survey of Canada Open File Report 3931. https://geoscan.nrcan.gc.ca/starweb/geoscan/servlet.starweb?path=geoscan/downloade.web&search1=R=212099

Hiroji, A. D. (2016). *Extracting sonar relative beam patterns for multi-sector multibeam sonar* [PhD Thesis, University of New Brunswick]. http://omg.unb.ca/wordpress/theses/PhD_Thesis_Anand_Hiroji_final.pdf

Hughes Clarke, J. (1994). Toward remote seafloor classification using the angular response of acoustic backscattering: A case study from multiple overlapping GLORIA data. *IEEE Journal of Oceanic Engineering*, *19*(1), 112–127. https://doi.org/10.1109/48.289456

Hughes Clarke, J. (2012). Optimal Use of Multibeam Technology in the Study of Shelf Morphodynamics. In M. Z. Li, C. R. Sherwood, & P. R. Hill (Eds.), *Sediments, Morphology and Sedimentary Processes on Continental Shelves* (pp. 1–28). John Wiley & Sons, Ltd. https://doi.org/10.1002/9781118311172.ch1

Hughes Clarke, J. (2020). *Multibeam Active Motion Compensation. Multi-Sector Strategies Leading to Multi-Swath Concept* [OE/ESCI874 Seabed Mapping Lecture Notes]. University of New Hampshire.

Hughes Clarke, J. (2022). *US-Canada Border Backscatter Calibration Site*. http://omg.unb.ca/Projects/heron_apr2022_html/Border_Backscatter_Calibration_Site.html

Hughes Clarke, J., Iwanowska, K. K., Parrott, R., Duffy, G., Lamplugh, M., & Griffin, J. (2008). *Inter-calibrating multi-source, multi-platform backscatter data sets to assist in compiling regional sediment type maps: Bay of Fundy*. 22.

Inman, D. L., & Jenkins, S. A. (2002). *Scour and Burial of Bottom Mines: A Primer for Fleet Use*. UC San Diego: Scripps Institution of Oceanography. https://escholarship.org/uc/item/7vz9j289

International Hydrographic Organization. (2020). *IHO Standards for Hydrographic Surveys* (S-44 Edition 6.0.0).

Jackson, D. R., & Richardson, M. D. (2007). *High-frequency seafloor acoustics*. Springer.

Jackson, D. R., Winebrenner, D. P., & Ishimaru, A. (1986). Application of the composite roughness model to high-frequency bottom backscattering. *The Journal of the Acoustical Society of America*, *79*(5), 1410–1422. https://doi.org/10.1121/1.393669

Jensen, F. B., & Schmidt, H. (1987). Subcritical penetration of narrow Gaussian beams into sediments. *The Journal of the Acoustical Society of America*, *82*(2), 574–579. https://doi.org/10.1121/1.395457

Kongsberg Maritime. (2018a). *Kongsberg EM Series Multibeam echo sounder—EM datagram formats* (No. 850-160692/W).

Kongsberg Maritime. (2018b). *Kongsberg EM 712 Multibeam echo sounder—Installation manual*. https://www.kongsberg.com/contentassets/270cdfb4fdb64e43a75dcc0b6eaf97a6/401027_em712_installation_manual.pdf

Kongsberg Maritime. (2021). *EM datagrams on *.kmall format* (410224 rev I).

L-3 Communications SeaBeam Instruments. (2000). *Multibeam Sonar Theory of Operation*. https://www3.mbari.org/data/mbsystem/sonarfunction/SeaBeamMultibeamTheoryOperation.pdf

Ladroit, Y., Lamarche, G., & Pallentin, A. (2018). Seafloor multibeam backscatter calibration experiment: Comparing 45°-tilted 38-kHz split-beam echosounder and 30-kHz multibeam

data. *Marine Geophysical Research*, *39*(1–2), 41–53. https://doi.org/10.1007/s11001-017-9340-5

Ladroit, Y., Sintes, C., Lurton, X., & Garello, R. (2012). Extended scatterers model for fast sonar signal simulation. *2012 Oceans - Yeosu*, 1–5. https://doi.org/10.1109/OCEANS-Yeosu.2012.6263487

Lamarche, G., & Lurton, X. (2018). Recommendations for improved and coherent acquisition and processing of backscatter data from seafloor-mapping sonars. *Marine Geophysical Research*, *39*(1–2), 5–22. https://doi.org/10.1007/s11001-017-9315-6

Lamarche, G., Lurton, X., Verdier, A.-L., & Augustin, J.-M. (2011). Quantitative characterisation of seafloor substrate and bedforms using advanced processing of multibeam backscatter—Application to Cook Strait, New Zealand. *Continental Shelf Research*, *31*(2), S93–S109. https://doi.org/10.1016/j.csr.2010.06.001

Land Information New Zealand. (2020). *HYSPEC Contract Specifications for Hydrographic Surveys* (Version 2.0).

Lanzoni, J. C., & Weber, T. C. (2010). High-resolution calibration of a multibeam echo sounder. *OCEANS 2010 MTS/IEEE SEATTLE*, 1–7. https://doi.org/10.1109/OCEANS.2010.5664519

Lanzoni, J. C., & Weber, T. C. (2011). A method for field calibration of a multibeam echo sounder. *OCEANS'11 MTS/IEEE KONA*, 1–7. https://doi.org/10.23919/OCEANS.2011.6107075

Lanzoni, J. C., & Weber, T. C. (2012). *Calibration of multibeam echo sounders: A comparison between two methodologies*. 070040. https://doi.org/10.1121/1.4772734

Lucieer, V., Roche, M., Degrendele, K., Malik, M., Dolan, M., & Lamarche, G. (2018). User expectations for multibeam echo sounders backscatter strength data-looking back into the

future. *Marine Geophysical Research*, *39*(1–2), 23–40. https://doi.org/10.1007/s11001-017-9316-5

Lurton, X. (2002). *An introduction to underwater acoustics: Principles and applications*. Springer.

Lurton, X., Eleftherakis, D., & Augustin, J.-M. (2018). Analysis of seafloor backscatter strength dependence on the survey azimuth using multibeam echosounder data. *Marine Geophysical Research*, *39*(1–2), 183–203. https://doi.org/10.1007/s11001-017-9318-3

MacLennan, D. N. (1981). *The theory of solid spheres as sonar calibration targets* (Scottish Fisheries Research Report No. 22; p. 17). Department of Agriculture and Fisheries for Scotland.

Malik, M., Lurton, X., & Mayer, L. (2018). A framework to quantify uncertainties of seafloor backscatter from swath mapping echosounders. *Marine Geophysical Research*, *39*(1–2), 151–168. https://doi.org/10.1007/s11001-018-9346-7

Mulhearn, P. J. (2000). *Modelling Acoustic Backscatter from Near-Normal Incidence Echosounders—Sensitivity Analysis of the Jackson Model* (DSTO-TN-0304). DSTO Aeronautical and Maritime Research Laboratory.

Ona, E., Mazauric, V., & Andersen, L. N. (2009). Calibration methods for two scientific multibeam systems. *ICES Journal of Marine Science*, *66*(6), 1326–1334. https://doi.org/10.1093/icesjms/fsp125

Perrot, Y., Brehmer, P., Roudaut, G., Gerstoft, P., Josse, E., Perrot, Y., Brehmer, P., Roudaut, G., & Josse, E. (2014). *Efficient multibeam sonar calibration and performance evaluation*. *3*(4), 14.

Roche, M., Degrendele, K., Vrignaud, C., Loyer, S., Le Bas, T., Augustin, J.-M., & Lurton, X. (2018). Control of the repeatability of high frequency multibeam echosounder backscatter

by using natural reference areas. *Marine Geophysical Research*, *39*(1–2), 89–104. https://doi.org/10.1007/s11001-018-9343-x

Schimel, A. C. G., Beaudoin, J., Parnum, I. M., Le Bas, T., Schmidt, V., Keith, G., & Ierodiaconou, D. (2018). Multibeam sonar backscatter data processing. *Marine Geophysical Research*, *39*(1–2), 121–137. https://doi.org/10.1007/s11001-018-9341-z

Stanic, S., Briggs, K. B., Fleischer, P., Ray, R. I., & Sawyer, W. B. (1988). Shallow-water high-frequency bottom scattering off Panama City, Florida. *The Journal of the Acoustical Society of America*, *83*(6), 2134–2144. https://doi.org/10.1121/1.396341

Stanic, S., Briggs, K. B., Fleischer, P., Sawyer, W. B., & Ray, R. I. (1989). High-frequency acoustic backscattering from a coarse shell ocean bottom. *The Journal of the Acoustical Society of America*, *85*(1), 125–136. https://doi.org/10.1121/1.397720

Stanic, S., & Kennedy, E. (1992). Fluctuations of high-frequency shallow-water seafloor reverberation. *The Journal of the Acoustical Society of America*, *91*(4), 1967–1973. https://doi.org/10.1121/1.403680

Swift, D. J. P. (1974). Continental Shelf Sedimentation. In C. A. Burk & C. L. Drake (Eds.), *The Geology of Continental Margins* (pp. 117–135). Springer Berlin Heidelberg. https://doi.org/10.1007/978-3-662-01141-6_10

Teng, Y. (2011). *Sector-specific Beam Pattern Compensation for Multi-sector and Multi-swath Multibeam Sonars* [Master's Thesis]. University of New Brunswick.

Thompson, D., & Beasley, D. J. (2012). *Handbook for Marine Geotechnical Engineering* (Technical SP-2209-OCN; p. 457). Naval Facilities Engineering Command.

Thorsos, E. I., Jackson, D. R., & Williams, K. L. (2000). Modeling of subcritical penetration into sediments due to interface roughness. *The Journal of the Acoustical Society of America*, *107*(1), 263–277. https://doi.org/10.1121/1.428303

Trzcinska, K., Tegowski, J., Pocwiardowski, P., Janowski, L., Zdroik, J., Kruss, A., Rucinska, M., Lubniewski, Z., & Schneider von Deimling, J. (2021). Measurement of Seafloor Acoustic Backscatter Angular Dependence at 150 kHz Using a Multibeam Echosounder. *Remote Sensing*, *13*(23), 4771. https://doi.org/10.3390/rs13234771

UNESCO/IOC. (n.d.). *United Nations Decade of Ocean Science for Sustainable Development 2021-2030*. Retrieved July 15, 2022, from https://www.oceandecade.org/

Urick, R. J. (1954). The Backscattering of Sound from a Harbor Bottom. *The Journal of the Acoustical Society of America*, *26*(2), 231–235. https://doi.org/10.1121/1.1907314

Weber, T. C., & Lurton, X. (2015). Chapter 2 - Background and fundamentals. In X. Lurton & G. Lamarche (Eds.), *Backscatter measurements by seafloor-mapping sonars - Guidelines and Recommendations* (pp. 25–51). https://geohab.org/wp-content/uploads/2018/09/BWSG-REPORT-MAY2015.pdf

Weber, T. C., Rice, G., & Smith, M. (2018). Toward a standard line for use in multibeam echo sounder calibration. *Marine Geophysical Research*, *39*(1–2), 75–87. https://doi.org/10.1007/s11001-017-9334-3

Weber, T. C., & Ward, L. G. (2015). Observations of backscatter from sand and gravel seafloors between 170 and 250 kHz. *The Journal of the Acoustical Society of America*, *138*(4), 2169–2180. https://doi.org/10.1121/1.4930185

Wendelboe, G. (2018). Backscattering from a sandy seabed measured by a calibrated multibeam echosounder in the 190–400 kHz frequency range. *Marine Geophysical Research*, *39*(1–2), 105–120. https://doi.org/10.1007/s11001-018-9350-y

Wendelboe, G., Dahl, H., Maillard, E., & Bjorno, L. (2012). *Towards a fully calibrated multibeam echosounder*. 070025. https://doi.org/10.1121/1.4767979

Wentworth, C. K. (1922). A Scale of Grade and Class Terms for Clastic Sediments. *The Journal of Geology*, *30*(5), 377–392. https://doi.org/10.1086/622910

Wilkens, R. H., & Richardson, M. D. (2007). Mine Burial Prediction: A Short History and Introduction. *IEEE Journal of Oceanic Engineering*, *32*(1), 3–9. https://doi.org/10.1109/JOE.2007.894331

Williams, K. L., Satkowiak, L. J., & Bugler, D. R. (1989). Linear and parametric array transmission across a water–sand interface—Theory, experiment, and observation of beam displacement. *The Journal of the Acoustical Society of America*, *86*(1), 311–325. https://doi.org/10.1121/1.398348